Monthly Notices
of the
ROYAL ASTRONOMICAL SOCIETY

Mon. Not. R. Astron. Soc. **415,** 1479–1508 (2011) doi:10.1111/j.1365-2966.2011.18795.x

# The LABOCA survey of the Extended *Chandra* Deep Field-South: a photometric redshift survey of submillimetre galaxies

J. L. Wardlow,[1,2⋆] Ian Smail,[3] K. E. K. Coppin,[3] D. M. Alexander,[2] W. N. Brandt,[4] A. L. R. Danielson,[2] B. Luo,[4] A. M. Swinbank,[3] F. Walter,[5] A. Weiß,[6] Y. Q. Xue,[4] S. Zibetti,[5] F. Bertoldi,[7] A. D. Biggs,[8] S. C. Chapman,[9] H. Dannerbauer,[5] J. S. Dunlop,[10] E. Gawiser,[11] R. J. Ivison,[10,12] K. K. Knudsen,[7,13] A. Kovács,[6] C. G. Lacey,[3] K. M. Menten,[6] N. Padilla,[14] H.-W. Rix[5] and P. P. van der Werf[15]

[1]*Department of Physics, Durham University, South Road, Durham DH1 3LE*
[2]*Department of Physics & Astronomy, Frederick Reines Hall, University of California, Irvine, CA 92697-4575, USA*
[3]*Institute for Computational Cosmology, Durham University, South Road, Durham DH1 3LE*
[4]*Department of Astronomy and Astrophysics, 525 Davey Lab, Pennsylvania State University, University Park, PA 16802, USA*
[5]*Max-Planck-Institut für Astronomie, Königstuhl 17, D-69117 Heidelberg, Germany*
[6]*Max-Planck-Institut für Radioastronomie, Auf dem Hügel 69, D-53121 Bonn, Germany*
[7]*Argelander Institut für Astronomie, Auf dem Hügel 71, D-53121 Bonn, Germany*
[8]*European Southern Observatory, Karl-Schwarzschild Strasse 2, D-85748 Garching, Germany*
[9]*Institute of Astronomy, Madingley Road, Cambridge CB3 0HA*
[10]*SUPA (Scottish University Physics Alliance), Institute for Astronomy, University of Edinburgh, Royal Observatory, Edinburgh EH9 3HJ*
[11]*Physics and Astronomy Department, Rutgers University, Piscataway, NJ 08854, USA*
[12]*UK Astronomy Technology Centre, Royal Observatory, Blackford Hill, Edinburgh EH9 3HJ*
[13]*Onsala Space Observatory, Chalmers University of Technology, SE-43992 Onsala, Sweden*
[14]*Departmento de Astronomia y Astrofisica, Pontificia Universidad Catolica de Chile, Santiago, Chile*
[15]*Leiden Observatory, Leiden University, PO Box 9513, 2300 RA Leiden, the Netherlands*

Accepted 2011 March 24. Received 2011 March 24; in original form 2010 June 9

**ABSTRACT**

We derive photometric redshifts from 17-band optical to mid-infrared photometry of 78 robust radio, 24-μm and *Spitzer* IRAC counterparts to 72 of the 126 submillimetre galaxies (SMGs) selected at 870 μm by LABOCA observations in the Extended *Chandra* Deep Field-South (ECDF-S). We test the photometric redshifts of the SMGs against the extensive archival spectroscopy in the ECDF-S. The median photometric redshift of identified SMGs is $z = 2.2 \pm 0.1$, the standard deviation is $\sigma_z = 0.9$ and we identify 11 (∼15 per cent) high-redshift ($z \geq 3$) SMGs. A statistical analysis of sources in the error circles of unidentified SMGs identifies a population of possible counterparts with a redshift distribution peaking at $z = 2.5 \pm 0.2$, which likely comprises ∼60 per cent of the unidentified SMGs. This confirms that the bulk of the undetected SMGs are coeval with those detected in the radio/mid-infrared. We conclude that at most ∼15 per cent of all the SMGs are below the flux limits of our IRAC observations and thus may lie at $z \gtrsim 3$ and hence at most ∼30 per cent of all SMGs have $z \gtrsim 3$. We estimate that the full $S_{870\,\mu\mathrm{m}} > 4$ mJy SMG population has a median redshift of $2.5 \pm 0.5$. In contrast to previous suggestions, we find no significant correlation between submillimetre flux and redshift. The median stellar mass of the SMGs derived from spectral energy distribution fitting is $(9.1 \pm 0.5) \times 10^{10}\,\mathrm{M}_{\odot}$ although we caution that the uncertainty in the star formation histories results in a factor of ∼5 uncertainty in these stellar masses. Using a single temperature modified blackbody fit with $\beta = 1.5$, the median characteristic dust temperature of SMGs is $37.4 \pm 1.4$ K. The infrared luminosity function shows that SMGs at $z = 2$–3 typically have

⋆E-mail: jwardlow@uci.edu

higher far-infrared luminosities and luminosity density than those at $z = 1$–2. This is mirrored in the evolution of the star formation rate density (SFRD) for SMGs which peaks at $z \sim 2$. The maximum contribution of bright SMGs to the global SFRD (∼5 per cent for SMGs with $S_{870\,\mu\mathrm{m}} \gtrsim 4$ mJy or ∼50 per cent extrapolated to SMGs with $S_{870\,\mu\mathrm{m}} > 1$ mJy) also occurs at $z \sim 2$.

**Key words:** galaxies: evolution – galaxies: high-redshift – galaxies: starburst – submillimetre: galaxies.

## 1 INTRODUCTION

Observations in the millimetre and submillimetre wavebands provide a uniquely powerful route to survey the distant Universe for intense dust-obscured starbursts (Blain & Longair 1993). This is due to the negative *K*-correction arising from the shape of the spectral energy distribution (SED) of the dust emission in the rest-frame far-infrared (FIR), which results in an almost constant apparent flux for sources with a fixed luminosity at $z \sim 1$–8.

Over the past decade, a series of ever larger surveys in the submillimetre and millimetre wavebands have mapped out a population of sources at mJy-flux limits with a surprisingly high surface density (e.g. Smail, Ivison & Blain 1997; Barger et al. 1998; Hughes et al. 1998; Eales et al. 1999; Bertoldi et al. 2000, 2007; Coppin et al. 2006; Knudsen, van der Werf & Kneib 2008; Weiß et al. 2009; Austermann et al. 2010). The mJy fluxes of these sources imply FIR luminosities of $\gtrsim 10^{12}$ $\mathrm{L}_{\odot}$, if the sources are at cosmological distances, $z \gtrsim 1$, classifying them as ultraluminous IR galaxies (ULIRGs; Sanders & Mirabel 1996). Their high surface density is far in excess of that expected from a 'no-evolution' model, suggesting very strong evolution of the population: $\propto (1 + z)^4$ (Smail et al. 1997; Blain et al. 1999). If this results from the strong luminosity evolution of starburst galaxies [as opposed to obscured active galactic nuclei (AGNs); Alexander et al. 2005; Laird et al. 2010], then a significant fraction of the massive star formation (and metal production) at high redshift may be occurring in this population.

To confirm this evolution and understand the physical processes driving it requires redshifts for the submillimetre galaxies (SMGs). Due to the coarse spatial resolution of the submillimetre and millimetre maps with which the SMGs are identified, combined with their optical faintness (in part due to their high dust obscuration), it has proved challenging to measure their spectroscopic redshift distribution (e.g. Barger, Cowie & Sanders 1999; Chapman et al. 2003a, 2005).

In fact, spectroscopic redshifts are not necessary to map the broad evolution of the SMG population; cruder photometric redshifts can be sufficient, if they are shown to be reliable. Various photometric redshift techniques have therefore been applied in an attempt to trace the evolution of SMGs, using their optical/near-/mid-IR or FIR/radio SEDs (e.g. Carilli & Yun 1999; Smail et al. 2000; Ivison et al. 2004; Pope et al. 2005, 2006; Aretxaga et al. 2007; Ivison et al. 2007; Clements et al. 2008; Dye et al. 2008; Biggs et al. 2011).

Both the spectroscopic and photometric analyses suggest that the bulk of the SMG population lie at $z \gtrsim 1$, with an apparent peak at $z \sim 2.2$ for the subset of SMGs which can be located through their μJy radio emission (Chapman et al. 2005). Nevertheless, there are significant disagreements between the different studies (see e.g. Chapman et al. 2005; Clements et al. 2008; Dye et al. 2008), which may arise in part due to differing levels and types of incompleteness in the identifications and biases in the redshift measurements. The most serious of these is the incompleteness due to challenges in reliably locating the correct SMG counterpart. They are typically identified through statistical arguments and physical correlations based on radio, mid- or near-IR emission (e.g. Ivison et al. 1998, 2000, 2005; Smail et al. 1999; Pope et al. 2005; Bertoldi et al. 2007; Hainline et al. 2009; Biggs et al. 2011), but these locate only ∼60–80 per cent of SMGs. The expectation is that the SMGs whose counterparts are missed could potentially include the highest redshift (and thus the faintest in the radio and mid-IR) examples, biasing the derived evolution (Ivison et al. 2005; Dannerbauer et al. 2010). Attempts to address this incompleteness through time-intensive submillimetre interferometry have located a small number of previously unidentified SMGs (e.g. Dannerbauer et al. 2002; Wang et al. 2007; Younger et al. 2007, 2009; Dannerbauer, Walter & Morrison 2008), but the nature and redshifts of this unidentified subset of SMGs remain critical issues for studies of the population as a whole.

In this paper, we use optical, near- and mid-IR photometry to study SMGs detected in the Extended *Chandra* Deep Field-South (ECDF-S) by the Large APEX BOlometer CAmera (LABOCA; Siringo et al. 2009) on the Atacama Pathfinder EXperiment (APEX; Güsten et al. 2006) 12-m telescope as part of the LABOCA ECDF-S Submillimetre Survey (LESS; Weiß et al. 2009). The LESS mapped the full 30 × 30-arcmin$^2$ ECDF-S at 870 μm to a noise level of $\sigma_{870\,\mu\mathrm{m}} \approx 1.2$ mJy beam$^{-1}$, for a beam with the angular resolution of 19.2 arcsec. 126 SMGs were detected at $>3.7\sigma$ significance (equivalent to a false-detection rate of ∼4 per cent, Weiß et al. 2009) and robust or tentative radio, 24-μm or IRAC mid-IR counterparts are identified to 93 (75 robust and 18 tentative) SMGs (Biggs et al. 2011). Here, we determine photometric redshifts for the 90 of these SMGs with detectable optical and near-IR counterparts (72 robust and 18 tentative) in the new and archival multiband photometry of the ECDF-S (described in Section 2). The LESS is an ideal survey for this purpose because of its panoramic, deep and uniform submillimetre coverage and extensive auxiliary data, including the spectroscopy of sufficient SMG counterparts to adequately test our photometric redshifts. In addition, the large size of the survey allows us to statistically measure the redshift distribution of the SMGs that we are unable to locate directly, in order to test if their redshift distribution differs significantly from the identified population.

The layout of this paper is as follows. In Sections 2 and 3, we derive multiband photometry from new and archival observations, while in Section 4, we describe the photometric redshift estimates and tests of their reliability. The photometric redshifts, SED fits, absolute *H*-band magnitudes, IR luminosities, dust temperatures and star formation rates (SFRs) of SMGs are presented and discussed in Section 5 and we give our conclusions in Section 6. Throughout this paper, we use deboosted submillimetre fluxes from Weiß et al. (2009), J2000 coordinates and Λ cold dark matter (ΛCDM) cosmology with $\Omega_{\mathrm{M}} = 0.3$, $\Omega_{\Lambda} = 0.7$ and $H_0 = 70\,\mathrm{km\,s^{-1}\,Mpc^{-1}}$. All photometry is on the AB magnitude system, in which $23.9 m_{\mathrm{AB}} = 1$ μJy, unless otherwise stated.

## 2 SAMPLE SELECTION

In this paper, we consider the optical and IR counterparts to 126 SMGs in the ECDF-S detected at $\geq 3.7\sigma$ (Weiß et al. 2009) and identified by VLA radio, MIPS (Rieke et al. 2004) 24-μm and IRAC (Fazio et al. 2004) emission (Biggs et al. 2011). Following convention and Biggs et al. (2011), we consider robust counterparts as those with a corrected Poissonian probability of being unassociated with the submillimetre source ($p$; Downes et al. 1986) of $p \leq 0.05$ in one or more of the radio, 24-μm or IRAC data sets, or $p = 0.05$–$0.10$ in two or more; tentative counterparts are those with $p = 0.05$–$0.10$ for only one of the three identification criteria. According to these definitions, Biggs et al. (2011) identified robust counterparts to 75 LESS SMGs and tentative counterparts to a further 18 SMGs. Only three of these robust counterparts, and none of the tentative counterparts, are undetected in our optical and IR imaging (Section 3).

Six of the SMGs have multiple robust counterparts; of these four SMGs (LESS 2, LESS 27, LESS 49 and LESS 74) have two counterparts, which as we will show in Section 4.1, having photometric redshifts consistent with them being at the same distance and thus possibly physically associated. The choice of the precise counterpart for the SMG is therefore irrelevant for these sources as their physical interpretation is not dependent upon this. However, the other two SMGs (LESS 10 and LESS 49) each has two robust counterparts with photometric redshifts and SEDs that suggest they are not physically associated. In these cases, from the information currently available, it is not possible to determine which of the two counterparts is the source of the submillimetre flux, or whether the LABOCA detection is a blend of the emission from two galaxies. To avoid bias, we have included all of the multiple counterparts in our analysis, but we note that their small number means that their inclusion does not significantly affect our results.

## 3 OPTICAL AND INFRARED DATA

SMGs typically have faint optical and near-IR counterparts (e.g. Ivison et al. 2002), so we require deep photometry for accurate photometric redshift estimates. The ECDF-S was chosen for this survey because it is an exceptionally well-studied field and as such we are able to utilize data from extensive archival imaging and spectroscopic surveys. For completeness and uniformity, we only consider surveys that cover a large fraction of the ECDF-S rather than the smaller and deeper central *Chandra* Deep Field-South (CDF-S) region. Therefore, we utilize the MUltiwavelength Survey by Yale-Chile (MUSYC; Gawiser et al. 2006) near-IR survey for $U$- to $K$-band imaging (Taylor et al. 2009b), and the Spitzer IRAC/MUSYC Public Legacy in ECDF-S (SIMPLE) imaging for *Spitzer* IRAC data (Damen et al. 2011). We also include $U$-band data from the deep GOODS/VIMOS imaging survey of the CDF-S (Nonino et al. 2009); although this covers only ∼60 per cent of LESS SMGs, it is valuable for galaxies that are undetected at short wavelengths in the shallower MUSYC survey.

In addition, we have carried out deep near-IR observations in the $J$ and $K_s$ bands with the HAWK-I (Pirard et al. 2004; Casali et al. 2006; Kissler-Patig et al. 2008) at the ESO-VLT (ID: 082.A-0890, PI: N. Padilla). The ECDF-S was covered with a mosaic of 16 pointings in each band, with a total exposure time of 0.75 and 1.1 h per pointing in the $J$ and $K_s$ bands, respectively. The median seeing is 0.7 arcsec in $J$ and 0.5 arcsec in $K_s$. Data reduction has been performed using an upgraded version of the official ESO pipeline for HAWK-I; customized calibration has been obtained from observations of photometric standard stars. More details and catalogues will be published in Zibetti et al. (in preparation).

For accurate photometric redshifts, we require consistent photometry in apertures which sample the same emitting area in each of the 17 filters. For consistency between surveys and to ensure that all detected SMG counterparts are included in this study, we extract photometry from the available survey imaging rather than relying on the catalogued sources. SMGs are typically brighter at mid-IR than optical wavelengths due to their high redshifts and extreme dust obscuration. Therefore, we use SExtractor (Bertin & Arnouts 1996) to create a source list from a combined image of the four IRAC channels, which is weighted such that a given magnitude receives equal contributions from all of the input images. Real sources are required to have at least four contiguous $0.6 \times 0.6$ arcsec$^2$ pixels with fluxes at least 1.5 times the background noise. In addition, we visually check the area within 15 arcsec of each LABOCA source to ensure that no potential SMG counterparts are missed.

We next use apphot in iraf to measure the fluxes in 3.8-arcsec-diameter apertures for each of the four IRAC bands. We then cut the catalogues to $\geq 3\sigma$ based on the background noise and finally apply aperture corrections as derived by the SWIRE team (Surace et al. 2005) to obtain total source magnitudes. The resolution in the $U$- to $K$-band imaging is better than the IRAC (full width at half-maximum $\leq 1.5$ arcsec compared to ∼2 arcsec for the IRAC) and so we convolve each $U$- to $K$-band image to match the 1.5-arcsec seeing of the worst band. We next use apphot to measure photometry in 3-arcsec-diameter apertures at the positions of the IRAC-selected sources. In all cases, we only allow apphot to re-centroid the aperture if centroiding does not cause the extraction region to be moved to a nearby source, as flagged by iraf's CIER parameter when the centroid shift >0.5 arcsec. We have not performed any deblending of the photometry but examination of the images suggests that fewer than ∼10 per cent of the SMG counterparts are affected. We note here that the photometric extraction process is not restricted to SMGs and yields photometry (which allows us to calculate consistent photometric redshifts) for IRAC-selected sources throughout the ECDF-S.

Finally, to ensure equivalent photometry between the IRAC and optical to near-IR filters, we create simulated IRAC images of point sources. Using these images, we calculate that the correction between the measured IRAC total magnitudes and the photometry extracted from 3-arcsec-diameter apertures on 1.5-arcsec-seeing images is $-0.014 \pm 0.017$ mag, and as such we do not apply any systematic corrections to the IRAC magnitudes at this stage. In Section 4.1, we calibrate the photometry prior to photometric redshift calculation in a process which corrects for small residual offsets. A summary of our photometry is presented in Table 1.

The median number of photometric filters per SMG counterpart is 15 and we require detections in at least three photometric filters in order to calculate photometric redshifts. Our final sample therefore contains 78 detected counterparts to the 72 robustly identified SMGs with sufficient detectable optical to IR emission. In Section 5.2, we show that the exclusion of the additional 21, tentatively identified, counterparts does not bias our results.

We employ the spectroscopy of the ECDF-S to calibrate our photometry with the SED templates (Section 4.1) and test our photometric redshifts (Section 4.2). We have examined the spectroscopic redshift catalogues from many archival surveys (Cristiani et al. 2000; Croom, Warren & Glazebrook 2001; Bunker et al. 2003; Dickinson et al. 2004; Le Fèvre et al. 2004; Stanway et al. 2004; Strolger et al. 2004; Szokoly et al. 2004; van der Wel et al. 2004; Zheng et al. 2004; Daddi et al. 2005; Doherty et al. 2005;

**Table 1.** Summary of the photometry employed in this paper.

| Filter | $\lambda_{\rm effective}$ (μm) | Detection limit ($3\sigma$; mag) | Reference |
|---|---|---|---|
| MUSYC WFI *U* | 0.35 | 26.9 | Taylor et al. (2009b) |
| MUSYC WFI *U*38 | 0.37 | 25.4 | Taylor et al. (2009b) |
| VIMOS *U* | 0.38 | 28.4[a] | Nonino et al. (2009) |
| MUSYC WFI *B* | 0.46 | 26.8 | Taylor et al. (2009b) |
| MUSYC WFI *V* | 0.54 | 26.7 | Taylor et al. (2009b) |
| MUSYC WFI *R* | 0.66 | 25.8 | Taylor et al. (2009b) |
| MUSYC WFI *I* | 0.87 | 24.9 | Taylor et al. (2009b) |
| MUSYC Mosaic II *z* | 0.91 | 24.5 | Taylor et al. (2009b) |
| MUSYC ISPI *J* | 1.25 | 23.6 | Taylor et al. (2009b) |
| HAWK-I *J* | 1.26 | 25.7 | Zibetti et al. (in preparation) |
| MUSYC SofI *H* | 1.66 | 23.0 | Taylor et al. (2009b) |
| MUSYC ISPI *K* | 2.13 | 22.7 | Taylor et al. (2009b) |
| HAWK-I $K_{\rm s}$ | 2.15 | 25.3 | Zibetti et al. (in preparation) |
| SIMPLE IRAC 3.6 μm | 3.58 | 24.6 | Damen et al. (2011) |
| SIMPLE IRAC 4.5 μm | 4.53 | 24.4 | Damen et al. (2011) |
| SIMPLE IRAC 5.8 μm | 5.79 | 22.8 | Damen et al. (2011) |
| SIMPLE IRAC 8.0 μm | 8.05 | 23.5 | Damen et al. (2011) |

[a]The listed depth of the VIMOS *U* band is that of the central region. The typical depth in the shallower outskirts is 28.0 mag.

Mignoli et al. 2005; Grazian et al. 2006; Ravikumar et al. 2007; Kriek et al. 2008; Vanzella et al. 2008; Popesso et al. 2009; Treister et al. 2009; Balestra et al. 2010, Koposov et al., in preparation). This search provides robust and tentative spectroscopic redshifts for ∼1800 galaxies with the ECDF-S, including 12 SMGs. A full analysis of the spectroscopic properties of LESS SMGs, including the spectroscopy from our own ongoing spectroscopic survey with the VLT (PID: 183.A-0666, PI: I. Smail), will be published in full in Danielson et al. (in preparation).

## 4 ANALYSIS

### 4.1 Photometric redshift calculation

We use HYPERZ[1] (Bolzonella, Miralles & Pelló 2000) to calculate the photometric redshifts of counterparts to LESS SMGs (Biggs et al. 2011). HYPERZ compares a model SED to observed magnitudes and computes $\chi^2$ for each combination of the spectral type, age, reddening and redshift, and thus statistically determines the most likely redshift of the galaxy. We use the elliptical (E), Sb, single burst (Burst) and constant star formation (CSF) spectral templates from Bruzual & Charlot (1993) which are provided with HYPERZ, and allow reddening (Calzetti et al. 2000) of $A_V = 0$–5 in steps of 0.2. This combination of templates and $A_V$ was shown by Wardlow et al. (2010) to be sufficient for calculating photometric redshifts of SMGs. Redshifts between 0 and 7 are considered and galaxy ages are required to be less than the age of the Universe at the appropriate redshift. In Section 4.4, we show that the HYPERZ-derived galaxy ages cannot be reliably determined, but we note here that the requirement for SMGs to be younger than the Universe does not significantly affect the derived redshifts. Galaxies are assigned zero flux in any filter in which they are not detected at $\geq 3\sigma$, with an error equal to the $1\sigma$ detection limit of that filter. To ensure that galaxies at $z \sim 2$–3 do not have their redshifts systematically underestimated, we have modified the handling of the Lyman $\alpha$ forest in HYPERZ, such that the intragalactic absorption in the models is increased and three different levels of absorption are considered in the fitting process. The reliability of the calculated redshifts and the validity of these settings are tested in full in Section 4.2.

We test for small systematic discrepancies between the photometry and model SEDs prior to using HYPERZ to calculate photometric redshifts of SMGs. This is done by running HYPERZ on 1796 galaxies and AGNs with spectroscopic redshifts in the ECDF-S and requiring a fit at the observed redshift. We then compare the model and measured magnitudes for each galaxy, and iteratively adjust the zero-points of the filters with the largest systematic offsets. This yields significant offsets for the following filters: VIMOS *U* (0.083 mag), MUSYC *U* (−0.091 mag), *U*38 (−0.074 mag), *R* (0.049 mag), *I* (0.048 mag), *z* (0.095 mag), HAWK-I *J* (0.043 mag), IRAC 3.6 (0.043 mag) and IRAC 8.0 μm (0.110 mag). The typical uncertainties in these corrections are ±0.02 and the remaining eight filters have no significant corrections.

The calibrated photometry of the robust LESS SMG counterparts is listed in Table 2, and in Table 3, we provide the coordinates, photometric redshifts, absolute rest-frame *H*-band magnitudes, FIR luminosities and characteristic dust temperatures of the SMGs (Section 5.7). We also provide the reduced $\chi^2$ of the best-fitting SED at the derived photometric redshift and the number of filters in which the SMG was detected and undetected (but observed). We caution that the reduced $\chi^2$ for galaxies with only a few photometric detections is typically low ($\lesssim$0.5) but the error on the photometric redshift is typically large, since there are only weak limits on the SED from the photometry. Therefore, the values of the reduced $\chi^2$ should be considered in conjunction with the number of photometric detections when considering the reliability of the photometric redshifts.

The median reduced $\chi^2$ of the SMG counterparts is 2.3 (2.1 if only the galaxies with reduced $\chi^2 \leq 10$ are considered). This suggests that our photometric errors are slightly underestimated and leads to apparently overly-precise photometric redshift limits. Indeed, we find that the HYPERZ 99 per cent confidence intervals more reliably represent the $1\sigma$ errors, yielding ∼68 per cent of SMGs with photometric redshifts consistent with the spectroscopic redshifts. Therefore, throughout this paper, we use the HYPERZ 99 per cent confidence intervals on the photometric redshift estimates to represent the $1\sigma$ uncertainty. Of the 78 SMG counterparts examined there are eight with poor fits of the SED to the photometry (indicated with reduced $\chi^2 > 10$). Of these, one (LESS 39) is blended in the optical imaging and two (LESS 66 and LESS 81) lie in stellar haloes. LESS 66 is also likely to be a quasi-stellar object (QSO), as is LESS 96 (they are both optically bright, unresolved point sources, with X-ray emission and broad emission lines in their spectra; see Appendix A), and another four SMGs with reduced $\chi^2 > 10$ (LESS 19, LESS 57, LESS 75 and LESS 111) have excess 8 μm flux compared to the best-fitting SED, which is indicative of an AGN component (see Section 4.3 for a full discussion). Since we did not include any QSO or AGN templates in the fitting procedure, it is unsurprising that these sources are not well represented by the employed SEDs. We note here that, as we show in Section 4.3, the exclusion of AGN templates does not bias our photometric redshift estimates.

### 4.2 Reliability of photometric redshifts

To test the reliability of our photometric redshifts ($z_{\rm phot}$), we first compare them to the spectroscopic redshifts ($z_{\rm spec}$) for 1796

[1] We use HYPERZ version 10.0 (http://www.ast.obs-mip.fr/users/roser/hyperz/)

**Table 2.** Observed photometry for robust counterparts to LESS SMGs. $3\sigma$ limiting magnitudes are presented where sources are covered by imaging but not detected; SMGs which are not covered by imaging in a given filter have no photometry listed in that filter.

| Source | MUSYC *U* | *U*38 | VIMOS *U* | *B* | *V* | *R* | *I* | *z* | MUSYC *J* | HAWK-I *J* | *H* | MUSYC *K* | HAWK-I *K* | 3.6 μm | 4.5 μm | 5.8 μm | 8 μm |
|---|---|---|---|---|---|---|---|---|---|---|---|---|---|---|---|---|---|
| LESS 1 | >26.85 | – | 28.44 ± 0.22 | >26.81 | >26.68 | >25.79 | >24.94 | >24.48 | >23.64 | 26.49 ± 0.28 | >23.02 | >22.72 | 24.35 ± 0.11 | 23.22 ± 0.16 | 23.27 ± 0.18 | 22.38 ± 0.26 | 22.41 ± 0.16 |
| LESS 2a | 25.67 ± 0.13 | 25.35 ± 0.32 | 25.19 ± 0.10 | 24.78 ± 0.05 | 24.65 ± 0.05 | 24.39 ± 0.09 | 24.08 ± 0.15 | 23.82 ± 0.17 | 22.81 ± 0.16 | 22.88 ± 0.04 | >23.02 | 21.65 ± 0.13 | 22.18 ± 0.03 | 21.37 ± 0.07 | 21.18 ± 0.07 | 21.13 ± 0.14 | 21.49 ± 0.09 |
| LESS 2b | >26.85 | >25.40 | >28.38 | >26.81 | 26.56 ± 0.29 | >25.79 | >24.94 | >24.48 | >23.64 | 24.44 ± 0.09 | 22.94 ± 0.29 | >22.72 | 23.26 ± 0.05 | 22.38 ± 0.11 | 22.08 ± 0.10 | 21.86 ± 0.20 | 22.23 ± 0.14 |
| LESS 3 | >26.85 | >25.40 | – | >26.81 | >26.68 | >25.79 | >24.94 | >24.48 | >23.64 | – | >23.02 | >22.72 | 23.30 ± 0.05 | 22.72 ± 0.12 | 22.09 ± 0.10 | 21.74 ± 0.19 | 21.42 ± 0.09 |
| LESS 6 | 26.57 ± 0.27 | >25.40 | 28.11 ± 0.23 | 25.95 ± 0.15 | 24.94 ± 0.07 | 24.00 ± 0.06 | 22.91 ± 0.05 | 22.75 ± 0.07 | 21.83 ± 0.07 | 22.09 ± 0.03 | 21.73 ± 0.10 | 21.10 ± 0.08 | 21.15 ± 0.02 | 21.14 ± 0.06 | 21.52 ± 0.08 | 21.92 ± 0.21 | 22.36 ± 0.17 |
| LESS 7 | 26.46 ± 0.25 | >25.40 | 26.29 ± 0.12 | 24.90 ± 0.06 | 24.08 ± 0.03 | 23.37 ± 0.04 | 22.22 ± 0.03 | 22.11 ± 0.04 | 21.69 ± 0.06 | 21.44 ± 0.02 | 21.07 ± 0.06 | 20.47 ± 0.04 | 20.46 ± 0.01 | 20.02 ± 0.04 | 19.91 ± 0.04 | 19.86 ± 0.08 | 20.15 ± 0.05 |
| LESS 9 | >26.85 | – | >28.38 | >26.81 | >26.68 | >25.79 | >24.94 | – | >23.64 | 24.19 ± 0.08 | >23.02 | >22.72 | 22.47 ± 0.04 | 21.85 ± 0.08 | 21.43 ± 0.08 | 21.29 ± 0.15 | 21.13 ± 0.08 |
| LESS 10a | 26.29 ± 0.21 | >25.40 | 25.74 ± 0.11 | 25.53 ± 0.11 | 25.60 ± 0.13 | 25.05 ± 0.16 | 24.61 ± 0.23 | >24.48 | >23.64 | 24.56 ± 0.10 | >23.02 | >22.72 | 23.33 ± 0.05 | 22.21 ± 0.10 | 21.78 ± 0.09 | 21.72 ± 0.19 | 21.46 ± 0.09 |
| LESS 10b | >26.85 | >25.40 | 27.45 ± 0.14 | 26.66 ± 0.28 | 25.79 ± 0.15 | 24.28 ± 0.08 | 22.63 ± 0.04 | 22.36 ± 0.05 | 21.41 ± 0.05 | 21.18 ± 0.02 | 20.81 ± 0.05 | 20.51 ± 0.05 | 20.29 ± 0.01 | 19.87 ± 0.03 | 20.14 ± 0.04 | 20.75 ± 0.12 | 21.32 ± 0.09 |
| LESS 11 | >26.85 | – | 27.86 ± 0.15 | >26.81 | >26.68 | >25.79 | >24.94 | >24.48 | >23.64 | 25.04 ± 0.12 | >23.02 | >22.72 | 23.58 ± 0.06 | 22.16 ± 0.10 | 21.63 ± 0.09 | 21.29 ± 0.15 | 21.15 ± 0.08 |
| LESS 12 | >26.85 | >25.40 | >28.38 | >26.81 | >26.68 | >25.79 | >24.94 | >24.48 | >23.64 | 25.71 ± 0.18 | >23.02 | >22.72 | 23.83 ± 0.06 | 22.72 ± 0.12 | 22.35 ± 0.12 | 22.17 ± 0.23 | 21.98 ± 0.12 |
| LESS 14 | >26.85 | >25.40 | >28.38 | >26.81 | 26.71 ± 0.32 | >25.79 | >24.94 | >24.48 | >23.64 | 25.56 ± 0.19 | – | >22.72 | 23.53 ± 0.06 | 22.55 ± 0.11 | 21.87 ± 0.09 | 21.56 ± 0.17 | 21.14 ± 0.08 |
| LESS 15 | >26.85 | – | – | >26.81 | >26.68 | >25.79 | >24.94 | >24.48 | >23.64 | – | – | >22.72 | – | 21.91 ± 0.09 | 21.30 ± 0.07 | 21.11 ± 0.14 | 21.05 ± 0.08 |
| LESS 16 | 25.04 ± 0.07 | 24.86 ± 0.21 | 24.83 ± 0.10 | 24.49 ± 0.04 | 24.01 ± 0.03 | 23.29 ± 0.03 | 21.79 ± 0.02 | 21.57 ± 0.02 | 20.95 ± 0.03 | 20.93 ± 0.02 | 20.44 ± 0.05 | 20.16 ± 0.03 | 20.15 ± 0.01 | 19.51 ± 0.03 | 19.71 ± 0.04 | 20.03 ± 0.08 | 20.08 ± 0.05 |
| LESS 17 | 25.15 ± 0.08 | 25.25 ± 0.29 | 24.83 ± 0.10 | 24.47 ± 0.04 | 24.26 ± 0.04 | 23.94 ± 0.06 | 23.27 ± 0.07 | 23.05 ± 0.09 | 22.05 ± 0.08 | 22.16 ± 0.03 | 21.64 ± 0.10 | 21.25 ± 0.09 | 21.07 ± 0.02 | 20.36 ± 0.04 | 20.16 ± 0.04 | 20.38 ± 0.10 | 20.76 ± 0.07 |
| LESS 18 | 26.11 ± 0.18 | >25.40 | 25.71 ± 0.11 | 25.52 ± 0.11 | 25.34 ± 0.10 | 25.30 ± 0.20 | 24.64 ± 0.23 | 24.41 ± 0.27 | 23.21 ± 0.22 | 22.81 ± 0.04 | 22.05 ± 0.14 | 21.35 ± 0.10 | 21.45 ± 0.02 | 20.38 ± 0.04 | 20.06 ± 0.04 | 20.01 ± 0.08 | 20.67 ± 0.06 |
| LESS 19 | >26.85 | >25.40 | 27.01 ± 0.12 | 27.04 ± 0.35 | 26.39 ± 0.25 | 26.79 ± 0.62 | >24.94 | >24.48 | >23.64 | 23.82 ± 0.07 | – | >22.72 | 24.22 ± 0.08 | 22.74 ± 0.12 | 22.23 ± 0.11 | 21.83 ± 0.19 | 21.98 ± 0.12 |
| LESS 20 | >26.85 | >25.40 | – | 26.25 ± 0.20 | 25.66 ± 0.13 | 25.89 ± 0.33 | >24.94 | >24.48 | >23.64 | 24.56 ± 0.09 | >23.02 | >22.72 | 22.57 ± 0.03 | 21.83 ± 0.08 | 21.48 ± 0.08 | 21.16 ± 0.14 | 21.46 ± 0.09 |
| LESS 22 | >26.85 | – | – | >26.81 | 26.20 ± 0.21 | 25.60 ± 0.26 | >24.94 | >24.48 | – | – | – | – | – | 20.47 ± 0.04 | 20.16 ± 0.04 | 20.04 ± 0.08 | 20.55 ± 0.06 |
| LESS 24 | >26.85 | >25.40 | – | 25.53 ± 0.11 | 25.71 ± 0.14 | 25.15 ± 0.18 | 24.31 ± 0.18 | 24.71 ± 0.35 | 22.71 ± 0.14 | – | – | 21.39 ± 0.10 | – | 20.67 ± 0.05 | 20.41 ± 0.05 | 20.73 ± 0.12 | 20.97 ± 0.08 |
| LESS 25 | – | >25.40 | 26.78 ± 0.13 | 26.02 ± 0.16 | 25.46 ± 0.11 | 25.04 ± 0.16 | 24.45 ± 0.20 | 24.25 ± 0.24 | >23.64 | 23.23 ± 0.05 | – | 21.82 ± 0.15 | 21.67 ± 0.02 | 21.03 ± 0.06 | 20.73 ± 0.05 | 20.58 ± 0.11 | 20.83 ± 0.07 |
| LESS 27a | >26.85 | >25.40 | – | >26.81 | >26.68 | >25.79 | >24.94 | >24.48 | >23.64 | >26.60 | >23.02 | >22.72 | – | 22.68 ± 0.12 | 22.30 ± 0.12 | 21.93 ± 0.22 | 22.31 ± 0.17 |
| LESS 27b | >26.85 | >25.40 | – | 26.14 ± 0.18 | 25.88 ± 0.16 | 25.35 ± 0.21 | >24.94 | >24.48 | >23.64 | – | – | >22.72 | – | 22.01 ± 0.09 | 21.68 ± 0.09 | 21.45 ± 0.16 | 21.95 ± 0.12 |
| LESS 29 | >26.85 | – | – | >26.81 | >26.68 | >25.79 | >24.94 | >24.48 | >23.64 | – | – | >22.72 | – | 22.22 ± 0.10 | 21.70 ± 0.09 | 21.27 ± 0.15 | 21.19 ± 0.09 |
| LESS 31 | >26.85 | >25.40 | – | >26.81 | >26.68 | >25.79 | >24.94 | >24.48 | >23.64 | 26.49 ± 0.26 | – | >22.72 | 23.46 ± 0.05 | 22.70 ± 0.12 | 22.19 ± 0.11 | 21.68 ± 0.18 | 21.65 ± 0.10 |
| LESS 34 | 24.98 ± 0.07 | 24.69 ± 0.18 | 24.39 ± 0.10 | 24.09 ± 0.03 | 23.67 ± 0.02 | 23.06 ± 0.03 | 21.87 ± 0.02 | 21.57 ± 0.02 | 20.94 ± 0.03 | 20.78 ± 0.02 | 20.29 ± 0.05 | 20.04 ± 0.03 | 19.90 ± 0.01 | 19.51 ± 0.03 | 19.71 ± 0.04 | 20.37 ± 0.10 | 20.73 ± 0.06 |
| LESS 36 | >26.85 | >25.40 | – | >26.81 | – | >25.79 | >24.94 | >24.48 | >23.64 | 25.70 ± 0.16 | – | 22.67 ± 0.30 | 22.76 ± 0.04 | 21.53 ± 0.07 | 21.06 ± 0.06 | 20.65 ± 0.11 | 20.98 ± 0.07 |
| LESS 37 | >26.85 | – | – | 26.19 ± 0.19 | 25.33 ± 0.10 | 24.18 ± 0.08 | 23.45 ± 0.08 | – | 22.86 ± 0.16 | – | 22.38 ± 0.18 | 21.16 ± 0.08 | – | 20.55 ± 0.05 | 20.41 ± 0.05 | 20.82 ± 0.13 | 20.94 ± 0.08 |
| LESS 39 | 25.44 ± 0.10 | >25.40 | – | 25.17 ± 0.08 | 24.77 ± 0.06 | 24.15 ± 0.07 | 23.91 ± 0.13 | 23.41 ± 0.12 | 23.59 ± 0.30 | 24.32 ± 0.10 | – | 22.01 ± 0.17 | – | 21.62 ± 0.07 | 21.28 ± 0.07 | 21.06 ± 0.14 | 21.07 ± 0.08 |
| LESS 40 | 24.82 ± 0.06 | 24.71 ± 0.19 | 24.54 ± 0.10 | 24.36 ± 0.04 | 24.07 ± 0.03 | 23.81 ± 0.05 | 23.36 ± 0.08 | 23.44 ± 0.12 | 23.04 ± 0.19 | 23.05 ± 0.05 | 22.52 ± 0.21 | 22.20 ± 0.20 | 22.09 ± 0.03 | 21.45 ± 0.07 | 21.12 ± 0.07 | 21.04 ± 0.13 | 20.99 ± 0.07 |
| LESS 41 | – | – | – | – | – | – | – | – | – | – | – | – | – | 20.50 ± 0.04 | 20.19 ± 0.04 | 19.91 ± 0.08 | 19.93 ± 0.05 |
| LESS 43 | >26.85 | >25.40 | 28.17 ± 0.21 | >26.81 | >26.68 | >25.79 | >24.94 | >24.48 | >23.64 | 23.93 ± 0.07 | 23.11 ± 0.33 | >22.72 | 22.58 ± 0.03 | 21.46 ± 0.07 | 21.04 ± 0.06 | 21.09 ± 0.14 | 21.73 ± 0.11 |
| LESS 44 | 25.06 ± 0.07 | 24.77 ± 0.20 | – | 24.42 ± 0.04 | 24.32 ± 0.04 | 24.34 ± 0.09 | 24.58 ± 0.22 | 24.32 ± 0.25 | – | – | – | – | – | 20.94 ± 0.05 | 20.59 ± 0.05 | 20.37 ± 0.10 | 20.82 ± 0.07 |
| LESS 47 | >26.85 | >25.40 | 27.05 ± 0.13 | 26.31 ± 0.21 | 25.58 ± 0.12 | 25.26 ± 0.19 | >24.94 | >24.48 | >23.64 | – | – | >22.72 | – | 22.37 ± 0.10 | 22.00 ± 0.10 | 21.80 ± 0.19 | 21.83 ± 0.12 |
| LESS 48 | – | – | >28.38 | – | – | – | – | – | – | – | – | – | – | 20.27 ± 0.04 | 20.15 ± 0.04 | 20.14 ± 0.09 | 20.80 ± 0.07 |
| LESS 49a | 26.26 ± 0.21 | >25.40 | – | 25.30 ± 0.09 | 25.22 ± 0.09 | 24.59 ± 0.11 | 24.07 ± 0.14 | 24.25 ± 0.24 | – | 23.85 ± 0.07 | – | – | 22.20 ± 0.03 | 21.26 ± 0.06 | 20.97 ± 0.06 | 21.41 ± 0.16 | 21.67 ± 0.11 |
| LESS 49b | >26.85 | >25.40 | – | 24.85 ± 0.06 | 24.56 ± 0.05 | 24.37 ± 0.09 | 24.13 ± 0.15 | 24.38 ± 0.26 | – | 23.85 ± 0.07 | – | – | 22.49 ± 0.03 | 22.16 ± 0.10 | 21.88 ± 0.09 | 21.65 ± 0.18 | 21.67 ± 0.11 |
| LESS 50a | 24.34 ± 0.04 | 24.09 ± 0.11 | 23.95 ± 0.10 | 23.70 ± 0.02 | 23.38 ± 0.02 | 22.90 ± 0.02 | 22.19 ± 0.03 | 22.04 ± 0.03 | 21.75 ± 0.06 | 21.62 ± 0.02 | 21.55 ± 0.09 | 21.32 ± 0.09 | 21.17 ± 0.02 | 21.20 ± 0.06 | 21.67 ± 0.09 | 22.17 ± 0.25 | 23.24 ± 0.32 |
| LESS 50b | >26.85 | – | 26.12 ± 0.12 | 26.17 ± 0.18 | 26.12 ± 0.20 | 25.90 ± 0.33 | >24.94 | >24.48 | >23.64 | 24.22 ± 0.08 | >23.02 | 22.63 ± 0.29 | 22.65 ± 0.03 | 21.70 ± 0.08 | 21.17 ± 0.07 | 20.76 ± 0.12 | 20.57 ± 0.06 |
| LESS 54 | >26.85 | – | 26.97 ± 0.13 | 26.08 ± 0.17 | 26.33 ± 0.24 | >25.79 | >24.94 | >24.48 | >23.64 | – | – | >22.72 | – | 21.66 ± 0.08 | 21.26 ± 0.07 | 21.31 ± 0.15 | 21.97 ± 0.12 |
| LESS 56 | >26.85 | >25.40 | >28.38 | >26.81 | >26.68 | >25.79 | >24.94 | >24.48 | 23.77 ± 0.35 | 24.46 ± 0.09 | 22.57 ± 0.22 | 22.15 ± 0.20 | 22.00 ± 0.03 | 21.27 ± 0.06 | 20.95 ± 0.06 | 20.81 ± 0.12 | 21.26 ± 0.09 |
| LESS 57 | >26.85 | >25.40 | 26.57 ± 0.12 | 25.14 ± 0.08 | 25.38 ± 0.10 | 24.96 ± 0.15 | >24.94 | >24.48 | >23.64 | 24.25 ± 0.08 | 23.05 ± 0.32 | >22.72 | 22.55 ± 0.03 | 22.02 ± 0.09 | 21.63 ± 0.08 | 21.35 ± 0.16 | 20.54 ± 0.06 |
| LESS 59 | >26.85 | >25.40 | 27.66 ± 0.14 | 26.89 ± 0.33 | 26.67 ± 0.31 | >25.79 | 24.36 ± 0.19 | >24.48 | 23.14 ± 0.21 | 23.03 ± 0.04 | 22.53 ± 0.21 | 21.62 ± 0.12 | 21.71 ± 0.02 | 20.71 ± 0.05 | 20.51 ± 0.05 | 20.83 ± 0.12 | 21.27 ± 0.09 |
| LESS 60 | 25.50 ± 0.11 | 25.12 ± 0.26 | 24.98 ± 0.10 | 24.95 ± 0.06 | 24.59 ± 0.05 | 24.08 ± 0.07 | 23.18 ± 0.07 | 22.87 ± 0.07 | 22.54 ± 0.12 | 22.23 ± 0.03 | 22.01 ± 0.13 | 21.49 ± 0.11 | 21.31 ± 0.02 | 20.59 ± 0.05 | 20.39 ± 0.05 | 20.54 ± 0.11 | 20.65 ± 0.06 |
| LESS 62 | 26.55 ± 0.26 | >25.40 | 26.27 ± 0.12 | 25.55 ± 0.11 | 25.09 ± 0.08 | 24.44 ± 0.10 | 23.45 ± 0.08 | 23.56 ± 0.13 | 22.17 ± 0.09 | 22.11 ± 0.03 | 21.50 ± 0.09 | 20.81 ± 0.06 | 20.85 ± 0.01 | 19.93 ± 0.03 | 19.75 ± 0.04 | 20.08 ± 0.09 | 20.28 ± 0.05 |
| LESS 63 | 25.39 ± 0.10 | >25.40 | – | 25.05 ± 0.07 | 24.69 ± 0.06 | 24.25 ± 0.08 | 23.28 ± 0.07 | 22.92 ± 0.08 | 22.02 ± 0.08 | 21.83 ± 0.03 | 21.80 ± 0.11 | 21.21 ± 0.09 | 21.12 ± 0.02 | 20.69 ± 0.05 | 20.53 ± 0.05 | 20.76 ± 0.12 | 21.09 ± 0.08 |
| LESS 64 | >26.85 | – | >28.38 | 26.53 ± 0.25 | 25.52 ± 0.12 | 24.29 ± 0.08 | 24.17 ± 0.16 | 24.44 ± 0.28 | >23.64 | 24.28 ± 0.09 | – | >22.72 | 23.06 ± 0.04 | 22.51 ± 0.11 | 22.41 ± 0.12 | 22.27 ± 0.25 | 21.87 ± 0.12 |
| LESS 66 | 21.03 ± 0.00 | 20.89 ± 0.01 | – | 21.18 ± 0.00 | 21.13 ± 0.00 | 20.79 ± 0.00 | 20.64 ± 0.01 | 20.23 ± 0.01 | 21.21 ± 0.04 | – | 20.33 ± 0.05 | 20.30 ± 0.04 | – | 19.61 ± 0.03 | 19.44 ± 0.03 | 19.36 ± 0.06 | 19.32 ± 0.03 |
| LESS 67 | 26.14 ± 0.19 | >25.40 | 25.37 ± 0.10 | 24.85 ± 0.06 | 24.52 ± 0.05 | 24.42 ± 0.09 | 23.80 ± 0.11 | 23.74 ± 0.16 | 23.07 ± 0.20 | 22.79 ± 0.04 | 22.23 ± 0.16 | 21.16 ± 0.08 | 21.40 ± 0.02 | 20.63 ± 0.05 | 20.32 ± 0.05 | 20.20 ± 0.09 | 20.75 ± 0.06 |
| LESS 70 | 25.19 ± 0.08 | 24.72 ± 0.19 | 24.56 ± 0.10 | 23.87 ± 0.02 | 23.78 ± 0.02 | 23.69 ± 0.05 | 23.61 ± 0.10 | 23.53 ± 0.13 | 22.56 ± 0.13 | 22.56 ± 0.04 | 22.51 ± 0.20 | 21.70 ± 0.13 | 21.60 ± 0.02 | 20.96 ± 0.06 | 20.78 ± 0.06 | 20.58 ± 0.11 | 20.89 ± 0.07 |
| LESS 72 | 25.56 ± 0.11 | 25.33 ± 0.31 | 25.08 ± 0.10 | 24.73 ± 0.05 | 24.03 ± 0.03 | 23.29 ± 0.03 | 21.91 ± 0.02 | 21.81 ± 0.03 | 21.02 ± 0.03 | 20.86 ± 0.02 | 20.54 ± 0.05 | 19.93 ± 0.03 | 19.90 ± 0.01 | 19.58 ± 0.03 | 19.86 ± 0.04 | 20.16 ± 0.09 | 20.55 ± 0.06 |
| LESS 73 | >26.85 | >25.40 | >28.38 | >26.81 | >26.68 | 25.82 ± 0.31 | 24.38 ± 0.19 | >24.48 | >23.64 | 24.35 ± 0.09 | >23.02 | >22.72 | 23.53 ± 0.07 | 22.92 ± 0.13 | 22.79 ± 0.14 | 22.33 ± 0.25 | 21.99 ± 0.12 |
| LESS 74a | >26.85 | – | >28.38 | >26.81 | >26.68 | >25.79 | >24.94 | 24.72 ± 0.35 | 23.23 ± 0.22 | 23.48 ± 0.05 | 23.08 ± 0.33 | 22.41 ± 0.24 | 22.08 ± 0.03 | 21.45 ± 0.07 | 21.17 ± 0.07 | 21.15 ± 0.14 | 21.81 ± 0.12 |
| LESS 74b | >26.85 | – | 27.83 ± 0.15 | >26.81 | >26.68 | >25.79 | 25.04 ± 0.32 | >24.48 | 23.36 ± 0.25 | 23.60 ± 0.06 | >23.02 | 22.08 ± 0.18 | 22.47 ± 0.03 | 21.58 ± 0.07 | 21.18 ± 0.07 | 21.04 ± 0.14 | 21.57 ± 0.10 |

**Table 2 –** *continued*

| Source | MUSYC $U$ | $U38$ | VIMOS $U$ | $B$ | $V$ | $R$ | $I$ | $z$ | MUSYC $J$ | HAWK-I $J$ | $H$ | MUSYC $K$ | HAWK-I $K$ | 3.6 μm | 4.5 μm | 5.8 μm | 8 μm |
|---|---|---|---|---|---|---|---|---|---|---|---|---|---|---|---|---|---|
| LESS 75 | 25.14 ± 0.08 | 24.80 ± 0.20 | – | 23.86 ± 0.02 | 23.60 ± 0.02 | 23.42 ± 0.04 | 23.38 ± 0.08 | 23.50 ± 0.13 | 22.81 ± 0.16 | 22.95 ± 0.04 | – | 22.10 ± 0.19 | 22.17 ± 0.03 | 21.07 ± 0.06 | 20.43 ± 0.05 | 19.79 ± 0.08 | 19.07 ± 0.03 |
| LESS 78 | 26.83 ± 0.33 | >25.40 | – | 25.66 ± 0.12 | 25.67 ± 0.13 | 25.86 ± 0.32 | 25.65 ± 0.52 | 24.06 ± 0.20 | 23.33 ± 0.24 | – | – | 22.20 ± 0.20 | – | 20.92 ± 0.05 | 20.59 ± 0.05 | 20.52 ± 0.11 | 20.95 ± 0.09 |
| LESS 79 | 26.37 ± 0.23 | >25.40 | 25.56 ± 0.11 | 25.16 ± 0.08 | 24.84 ± 0.06 | 24.54 ± 0.10 | 23.61 ± 0.10 | 23.74 ± 0.16 | 22.63 ± 0.13 | 22.41 ± 0.03 | 22.09 ± 0.14 | 21.24 ± 0.09 | 21.20 ± 0.02 | 20.32 ± 0.04 | 20.16 ± 0.04 | 20.32 ± 0.10 | 20.87 ± 0.07 |
| LESS 81 | 25.94 ± 0.16 | >25.40 | – | 24.18 ± 0.03 | 23.73 ± 0.02 | 23.39 ± 0.04 | 22.79 ± 0.05 | – | 21.38 ± 0.04 | 22.45 ± 0.03 | 21.49 ± 0.08 | 20.90 ± 0.07 | 21.70 ± 0.02 | 20.18 ± 0.04 | 19.91 ± 0.04 | 20.11 ± 0.09 | 20.61 ± 0.07 |
| LESS 84 | 26.42 ± 0.24 | >25.40 | 25.62 ± 0.11 | 25.10 ± 0.07 | 25.03 ± 0.08 | 24.89 ± 0.14 | 24.43 ± 0.20 | >24.48 | >23.64 | 23.36 ± 0.05 | 22.81 ± 0.26 | 21.71 ± 0.13 | 22.10 ± 0.03 | 21.43 ± 0.07 | 21.08 ± 0.06 | 20.92 ± 0.13 | 21.10 ± 0.08 |
| LESS 87 | – | – | 25.52 ± 0.11 | – | – | – | – | – | – | – | – | – | – | 21.32 ± 0.06 | 21.07 ± 0.06 | 21.03 ± 0.14 | 20.90 ± 0.07 |
| LESS 88 | 26.78 ± 0.32 | >25.40 | 25.98 ± 0.11 | 25.42 ± 0.10 | 25.10 ± 0.08 | 24.98 ± 0.15 | 24.27 ± 0.17 | 24.43 ± 0.28 | 23.25 ± 0.23 | 23.51 ± 0.06 | 23.05 ± 0.32 | 22.00 ± 0.17 | 22.05 ± 0.04 | 21.15 ± 0.06 | 20.85 ± 0.06 | 20.73 ± 0.12 | 21.09 ± 0.08 |
| LESS 96 | 21.92 ± 0.00 | 21.73 ± 0.01 | 21.32 ± 0.10 | 20.82 ± 0.00 | 20.62 ± 0.00 | 20.40 ± 0.00 | 19.99 ± 0.00 | 19.72 ± 0.00 | 19.74 ± 0.01 | 19.50 ± 0.01 | 19.77 ± 0.04 | 19.76 ± 0.02 | 19.59 ± 0.01 | 19.63 ± 0.03 | 19.43 ± 0.03 | 19.07 ± 0.05 | 18.59 ± 0.02 |
| LESS 98 | >26.85 | – | – | >26.81 | >26.68 | >25.79 | 24.61 ± 0.23 | 24.64 ± 0.33 | 23.41 ± 0.26 | 22.98 ± 0.04 | – | 21.49 ± 0.11 | 21.40 ± 0.02 | 20.22 ± 0.04 | 19.84 ± 0.04 | 19.99 ± 0.08 | 20.31 ± 0.05 |
| LESS 101 | >26.85 | >25.40 | 27.28 ± 0.13 | 26.70 ± 0.29 | 26.20 ± 0.21 | 25.58 ± 0.25 | >24.94 | >24.48 | >23.64 | 24.33 ± 0.10 | >23.02 | >22.72 | 23.16 ± 0.05 | 22.44 ± 0.11 | 21.93 ± 0.10 | 21.62 ± 0.18 | 21.55 ± 0.10 |
| LESS 102 | >26.85 | >25.40 | – | 26.93 ± 0.34 | 26.24 ± 0.22 | 25.98 ± 0.35 | 24.97 ± 0.31 | 24.49 ± 0.29 | 22.91 ± 0.17 | – | – | 21.29 ± 0.09 | – | 20.43 ± 0.04 | 20.13 ± 0.04 | 20.17 ± 0.09 | 20.92 ± 0.08 |
| LESS 103 | >26.85 | – | – | >26.81 | >26.68 | >25.79 | >24.94 | >24.48 | >23.64 | – | – | 22.78 ± 0.33 | – | 21.51 ± 0.07 | 21.25 ± 0.07 | 21.12 ± 0.14 | 21.77 ± 0.12 |
| LESS 106 | >26.85 | >25.40 | – | >26.81 | >26.68 | >25.79 | 24.51 ± 0.21 | 24.38 ± 0.27 | 23.07 ± 0.20 | 22.71 ± 0.04 | 21.76 ± 0.11 | 21.33 ± 0.10 | 21.22 ± 0.02 | 20.22 ± 0.04 | 19.83 ± 0.04 | 19.91 ± 0.08 | 20.06 ± 0.05 |
| LESS 108 | 21.25 ± 0.00 | 21.00 ± 0.01 | 20.82 ± 0.10 | 19.64 ± 0.00 | 19.11 ± 0.00 | 18.60 ± 0.00 | 18.02 ± 0.00 | 17.94 ± 0.00 | 17.41 ± 0.00 | 17.35 ± 0.00 | 17.15 ± 0.04 | 17.00 ± 0.00 | 16.99 ± 0.00 | – | 17.79 ± 0.01 | 17.84 ± 0.03 | – |
| LESS 110 | – | – | – | – | – | – | – | – | – | – | – | – | – | 23.13 ± 0.16 | 22.44 ± 0.12 | 21.82 ± 0.20 | 21.72 ± 0.12 |
| LESS 111 | 25.06 ± 0.07 | 25.03 ± 0.25 | – | 23.82 ± 0.02 | 23.31 ± 0.02 | 22.79 ± 0.02 | 22.38 ± 0.03 | 22.27 ± 0.04 | 22.75 ± 0.15 | – | – | 21.57 ± 0.12 | – | 21.04 ± 0.06 | 20.98 ± 0.06 | 20.81 ± 0.12 | 20.23 ± 0.05 |
| LESS 112 | – | – | 26.98 ± 0.15 | – | – | – | – | – | – | – | – | – | – | 20.93 ± 0.05 | 20.59 ± 0.05 | 20.43 ± 0.10 | 21.06 ± 0.08 |
| LESS 114 | 25.31 ± 0.09 | 25.24 ± 0.29 | 24.98 ± 0.10 | 24.52 ± 0.04 | 24.21 ± 0.04 | 23.87 ± 0.06 | 23.05 ± 0.06 | 22.91 ± 0.07 | 21.63 ± 0.06 | 21.62 ± 0.02 | 20.97 ± 0.05 | 20.68 ± 0.05 | 20.67 ± 0.01 | 19.93 ± 0.03 | 19.66 ± 0.03 | 19.86 ± 0.08 | 20.10 ± 0.05 |
| LESS 115 | – | – | – | – | – | – | – | – | – | – | – | – | – | 22.58 ± 0.12 | – | 21.41 ± 0.18 | – |
| LESS 117 | 26.42 ± 0.24 | >25.40 | – | >26.81 | >26.68 | >25.79 | 24.09 ± 0.15 | – | 22.58 ± 0.13 | – | 21.60 ± 0.09 | 21.47 ± 0.11 | – | 20.56 ± 0.05 | 20.31 ± 0.05 | 20.53 ± 0.11 | 20.93 ± 0.08 |
| LESS 118 | – | – | – | – | – | – | – | – | – | 24.30 ± 0.08 | – | – | 23.98 ± 0.08 | 23.39 ± 0.17 | 23.81 ± 0.25 | 22.77 ± 0.34 | >23.50 |
| LESS 120 | >26.85 | >25.40 | – | 26.77 ± 0.30 | 25.99 ± 0.18 | >25.79 | 24.60 ± 0.23 | 23.79 ± 0.16 | 23.34 ± 0.25 | 23.23 ± 0.05 | 22.79 ± 0.26 | 21.77 ± 0.14 | 21.87 ± 0.03 | 20.99 ± 0.05 | 20.70 ± 0.05 | 20.74 ± 0.12 | 21.33 ± 0.09 |
| LESS 122 | 24.83 ± 0.06 | 24.70 ± 0.19 | 24.42 ± 0.10 | 23.77 ± 0.02 | 23.44 ± 0.02 | 23.28 ± 0.03 | 22.94 ± 0.05 | 22.86 ± 0.07 | 21.96 ± 0.07 | 21.96 ± 0.03 | 21.43 ± 0.08 | 21.20 ± 0.09 | 21.00 ± 0.02 | 20.24 ± 0.04 | 19.88 ± 0.04 | 19.59 ± 0.07 | 19.67 ± 0.04 |
| LESS 126 | >26.85 | >25.40 | 26.87 ± 0.12 | 26.32 ± 0.21 | 26.61 ± 0.30 | 25.87 ± 0.32 | >24.94 | – | >23.64 | 23.84 ± 0.07 | 22.72 ± 0.24 | 22.99 ± 0.38 | 22.24 ± 0.03 | 21.29 ± 0.06 | 21.04 ± 0.06 | 21.21 ± 0.14 | 21.68 ± 0.10 |

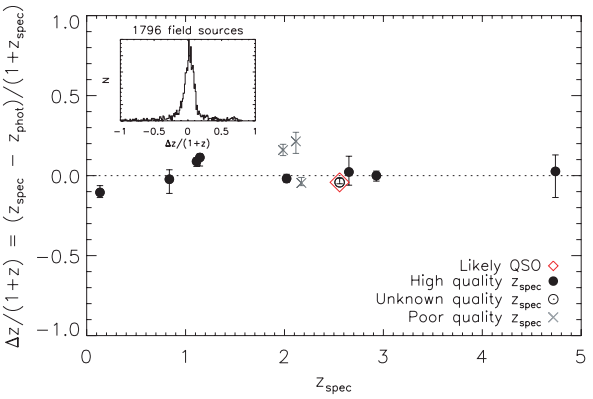


**Figure 1.** Spectroscopic redshift against $\Delta z/(1+z)$ for robust counterparts to LESS SMGs. We distinguish between high- and low-quality spectroscopic redshifts as determined by the flags provided in most archival catalogues, and highlight the likely QSO (LESS 96; see Appendix A). The median (mean) $\Delta z/(1+z)$ for all the SMGs is $0.023 \pm 0.042$ ($0.033 \pm 0.094$). The inset plot shows the histogram of $\Delta z/(1+z)$ for 1796 galaxies and AGNs in the ECDF-S with spectroscopic redshifts. The distribution is centred on $0.016 \pm 0.002$ and has a $1\sigma$ dispersion of 0.05. We conclude that our photometric redshifts are a good proxy for spectroscopic redshifts for both samples.

galaxies and AGNs in the ECDF-S and calculate $\Delta z = z_{\rm spec} - z_{\rm phot}$ for each source (here and throughout this paper, errors on median measurements are from bootstrapping). The histogram of $\Delta z/(1+z)$ for these 1796 sources is shown as an inset in Fig. 1; the sample is centred on $\Delta z/(1+z) = 0.016 \pm 0.002$ and has a $1\sigma$ dispersion of 0.05. We define outliers as sources with $|\Delta z|/(1+z) > 0.3$; the outlier fraction for these 1796 field galaxies and AGNs is 0.15. We also calculate the outlier resistant normalized median absolute deviation (NMAD) of $\Delta z$, $\sigma_{\rm NMAD} = 1.48 \times {\rm median}(|\Delta z - {\rm median}(\Delta z)|/(1+z)) = 0.097$. These statistics show that our photometric redshifts are a good proxy for spectroscopic redshift for these sources. We also note that Hildebrandt et al. (2010) recently performed extensive testing of the accuracy and reliability of 19 different photometric redshift codes, including several neural networks and others with training modes, on galaxies in the GOODS with a median spectroscopic redshift $z < 1$. They found that the performance of HYPERZ, without any training (to calibrate the photometric zero-points; Section 4.1), is close to the average of all 19 codes.

However, the median redshift, $z = 0.84$, of this test sample is lower than that expected for SMGs and the targets are typically brighter at optical wavelengths, limiting the usefulness of these comparisons for the SMGs. Therefore, we next test our photometric redshift calculation on the 12 robust SMG counterparts with published spectroscopic redshifts from archival surveys of the ECDF-S. Fig. 1 shows spectroscopic redshift against $\Delta z/(1+z)$ for these 12 SMG counterparts. Quality flags are published in many catalogues and where possible we distinguish between high- and low-quality spectroscopic redshifts. The median $\Delta z/(1+z)$ for SMGs is 0.023 $\pm$ 0.042, the mean $\Delta z/(1+z) = 0.033 \pm 0.094$ and $\sigma_{\rm NMAD} = 0.037$, suggesting that our photometric redshifts for SMGs are reliable. We caution that the SMGs without reliable spectroscopic redshifts are fainter on average than those with reliable redshifts, which could also affect the quality of their photometric redshifts. Although the median $R$-band magnitude of the SMGs detected in the MUSYC survey is the same for the counterparts with and without spectroscopic redshifts, all of the 12 SMGs with spectroscopic redshifts are detected in the MUSYC $R$ band, while only 36 of the 66 SMGs without spectroscopic redshifts are detected. We note that

**Table 3.** The catalogue of 78 robust counterparts to LESS SMGs, their photometric redshift estimates, reduced $\chi^2$ of the best-fitting SED and the number of photometric filters in which the galaxy is observed. We also present the absolute rest-frame $H$-band magnitudes, the derived FIR luminosities and characteristic dust temperatures of the SMGs.

| SMG[a] | Short name | RA[b] | Dec.[b] | $z_{\rm phot}$[c] | $\chi^2_{\rm red}$[d] | Filters[e] | $M_H$[f] | $L_{\rm FIR}$[g] ($10^{12}$ L$_\odot$) | $T_{\rm D}$[h] (K) | ID type[i] |
|---|---|---|---|---|---|---|---|---|---|---|
| LESS J033314.3−275611 | LESS 1 | 03$^{\rm h}$33$^{\rm m}$14$^{\rm s}$.38 | −27°56′11″.6 | $2.68^{+0.40}_{-0.38}$ | 1.4 | 7 [9] | −23.03 | <3.8 | <24.9 | M |
| LESS J033302.5−275643 | LESS 2a | 03$^{\rm h}$33$^{\rm m}$2$^{\rm s}$.55 | −27°56′44″.7 | $1.80^{+0.35}_{-0.14}$ | 2.8 | 16 [1] | −23.42 | <1.5 | <19.9 | M |
| LESS J033302.5−275643 | LESS 2b | 03$^{\rm h}$33$^{\rm m}$2$^{\rm s}$.68 | −27°56′42″.6 | $2.27^{+0.16}_{-0.55}$ | 1.1 | 8 [9] | −23.15 | $30.9^{+6.4}_{-15.3}$ | $44.2^{+2.5}_{-7.6}$ | R |
| LESS J033321.5−275520 | LESS 3 | 03$^{\rm h}$33$^{\rm m}$21$^{\rm s}$.50 | −27°55′20″.1 | $3.92^{+0.54}_{-0.72}$ | 0.5 | 5 [10] | −24.66 | <8.9 | <35.2 | M |
| LESS J033257.1−280102 | LESS 6 | 03$^{\rm h}$32$^{\rm m}$57$^{\rm s}$.15 | −28°1′1″.5 | $0.40^{+0.09}_{-0.03}$ | 4.3 | 16 [1] | −20.29 | $0.09^{+0.08}_{-0.03}$ | $12.8^{+1.1}_{-0.8}$ | RM |
| LESS J033315.6−274523 | LESS 7 | 03$^{\rm h}$33$^{\rm m}$15$^{\rm s}$.41 | −27°45′24″.0 | $2.81^{+0.18}_{-0.07}$ | 6.9 | 16 [1] | −25.50 | $16.2^{+4.3}_{-2.4}$ | $41.1^{+2.6}_{-1.9}$ | RM |
| LESS J033211.3−275210 | LESS 9 | 03$^{\rm h}$32$^{\rm m}$11$^{\rm s}$.35 | −27°52′12″.9 | $4.63^{+0.10}_{-1.10}$ | 2.4 | 6 [9] | −25.29 | $20.3^{+5.9}_{-11.7}$ | $48.3^{+3.4}_{-10.0}$ | RM |
| LESS J033219.0−275219 | LESS 10a | 03$^{\rm h}$32$^{\rm m}$19$^{\rm s}$.04 | −27°52′14″.3 | $2.46^{+0.15}_{-0.15}$ | 6.0 | 12 [5] | −23.46 | $8.7^{+2.4}_{-2.0}$ | $34.5^{+2.2}_{-2.2}$ | R |
| LESS J033219.0−275219 | LESS 10b | 03$^{\rm h}$32$^{\rm m}$19$^{\rm s}$.30 | −27°52′19″.1 | $0.91^{+0.07}_{-0.05}$ | 4.5 | 15 [2] | −23.32 | $0.8^{+0.3}_{-0.2}$ | $18.6^{+1.1}_{-1.0}$ | R |
| LESS J033213.6−275602 | LESS 11 | 03$^{\rm h}$32$^{\rm m}$13$^{\rm s}$.84 | −27°55′59″.8 | $2.60^{+0.30}_{-0.36}$ | 3.2 | 7 [9] | −24.04 | $9.9^{+4.4}_{-3.8}$ | $35.9^{+3.5}_{-4.0}$ | R |
| LESS J033248.1−275414 | LESS 12 | 03$^{\rm h}$32$^{\rm m}$47$^{\rm s}$.96 | −27°54′16″.1 | $3.92^{+1.02}_{-2.11}$ | 0.1 | 6 [11] | −24.06 | $18.2^{+17.3}_{-15.6}$ | $45.6^{+9.8}_{-19.7}$ | RM |
| LESS J033152.6−280320 | LESS 14 | 03$^{\rm h}$31$^{\rm m}$52$^{\rm s}$.47 | −28°3′18″.6 | $3.56^{+0.92}_{-0.56}$ | 0.8 | 7 [9] | −24.74 | $32.6^{+26.6}_{-12.5}$ | $51.3^{+10.6}_{-6.7}$ | RM |
| LESS J033333.4−275930 | LESS 15 | 03$^{\rm h}$33$^{\rm m}$33$^{\rm s}$.35 | −27°59′29″.4 | $1.95^{+3.05}_{-0.39}$ | 0.2 | 4 [8] | −23.59 | <1.8 | <22.6 | M |
| LESS J033218.9−273738 | LESS 16 | 03$^{\rm h}$32$^{\rm m}$18$^{\rm s}$.70 | −27°37′43″.5 | $1.09^{+0.08}_{-0.09}$ | 4.1 | 17 [0] | −24.05 | $1.2^{+0.4}_{-0.4}$ | $20.8^{+1.4}_{-1.5}$ | R |
| LESS J033207.6−275123 | LESS 17 | 03$^{\rm h}$32$^{\rm m}$7$^{\rm s}$.26 | −27°51′20″.1 | $1.55^{+0.11}_{-0.11}$ | 1.0 | 17 [0] | −24.11 | $6.6^{+1.5}_{-1.4}$ | $32.7^{+2.0}_{-2.1}$ | RM |
| LESSJ033205.1−274652 | LESS 18 | 03$^{\rm h}$32$^{\rm m}$4$^{\rm s}$.87 | −27°46′47″.4 | $2.07^{+0.08}_{-0.09}$ | 2.4 | 16 [1] | −24.88 | $13.8^{+2.1}_{-2.0}$ | $40.2^{+2.1}_{-2.1}$ | RM |
| LESS J033208.1−275818 | LESS 19 | 03$^{\rm h}$32$^{\rm m}$8$^{\rm s}$.23 | −27°58′13″.7 | $2.11^{+0.11}_{-0.10}$ | 10.3 | 10 [6] | −22.80 | $3.4^{+1.3}_{-1.1}$ | $28.3^{+2.3}_{-2.2}$ | RI |
| LESS J033316.6−280018 | LESS 20 | 03$^{\rm h}$33$^{\rm m}$16$^{\rm s}$.77 | −28°0′15″.8 | $2.80^{+0.17}_{-0.27}$ | 2.2 | 9 [7] | −24.28 | $903^{+132}_{-190}$ | $124.6^{+7.8}_{-10.5}$ | RM |
| LESSJ033147.0−273243 | LESS 22 | 03$^{\rm h}$31$^{\rm m}$46$^{\rm s}$.90 | −27°32′38″.8 | $1.95^{+0.34}_{-0.38}$ | 2.4 | 6 [4] | −24.67 | $10.4^{+5.8}_{-4.6}$ | $36.6^{+4.6}_{-5.1}$ | RM |
| LESS J033336.8−274401 | LESS 24 | 03$^{\rm h}$33$^{\rm m}$36$^{\rm s}$.97 | −27°43′58″.1 | $1.72^{+0.29}_{-0.36}$ | 2.6 | 11 [2] | −24.06 | $4.1^{+2.6}_{-2.1}$ | $29.2^{+3.6}_{-4.3}$ | RM |
| LESS J033157.1−275940 | LESS 25 | 03$^{\rm h}$31$^{\rm m}$56$^{\rm s}$.85 | −27°59′38″.9 | $2.28^{+0.09}_{-0.15}$ | 3.0 | 13 [2] | −24.47 | $8.1^{+1.8}_{-2.1}$ | $36.4^{+2.4}_{-2.8}$ | RM |
| LESS J033149.7−273432 | LESS 27a | 03$^{\rm h}$31$^{\rm m}$49$^{\rm s}$.88 | −27°34′30″.4 | $2.10^{+1.00}_{-0.88}$ | 0.1 | 4 [11] | −22.83 | <2.1 | <25.1 | I |
| LESS J033149.7−273432 | LESS 27b | 03$^{\rm h}$31$^{\rm m}$49$^{\rm s}$.92 | −27°34′36″.7 | $2.46^{+0.42}_{-0.72}$ | 1.9 | 7 [6] | −23.73 | <3.1 | <28.1 | MI |
| LESS J033336.9−275813 | LESS 29 | 03$^{\rm h}$33$^{\rm m}$36$^{\rm s}$.88 | −27°58′8″.8 | $2.64^{+4.36}_{-0.87}$ | 0.1 | 4 [8] | −24.13 | $8.4^{+78.5}_{-5.8}$ | $36.8^{+44.0}_{-9.2}$ | R |
| LESS J033150.0−275743 | LESS 31 | 03$^{\rm h}$31$^{\rm m}$49$^{\rm s}$.77 | −27°57′40″.4 | $3.63^{+0.84}_{-0.70}$ | 0.3 | 6 [9] | −24.30 | $9.9^{+10.0}_{-5.4}$ | $41.8^{+8.5}_{-7.3}$ | RI |
| LESS J033217.6−275230 | LESS 34 | 03$^{\rm h}$32$^{\rm m}$17$^{\rm s}$.60 | −27°52′28″.1 | $0.86^{+0.11}_{-0.05}$ | 3.8 | 17 [0] | −23.53 | <0.3 | <15.6 | M |
| LESS J033149.2−280208 | LESS 36 | 03$^{\rm h}$31$^{\rm m}$48$^{\rm s}$.94 | −28°2′13″.6 | $2.49^{+0.53}_{-0.31}$ | 0.3 | 7 [7] | −24.58 | $7.8^{+6.4}_{-3.0}$ | $36.7^{+6.2}_{-4.2}$ | RM |
| LESS J033336.0−275347 | LESS 37 | 03$^{\rm h}$33$^{\rm m}$36$^{\rm s}$.01 | −27°53′49″.4 | $3.52^{+0.26}_{-0.36}$ | 4.0 | 11 [1] | −24.95 | <6.9 | <37.3 | M |
| LESS J033144.9−273435 | LESS 39 | 03$^{\rm h}$31$^{\rm m}$45$^{\rm s}$.00 | −27°34′36″.3 | $2.59^{+0.16}_{-0.06}$ | 12.6 | 13 [1] | −24.25 | $8.2^{+2.8}_{-1.8}$ | $37.7^{+3.3}_{-2.9}$ | RM |
| LESS J033246.7−275120 | LESS 40 | 03$^{\rm h}$32$^{\rm m}$46$^{\rm s}$.77 | −27°51′20″.7 | $1.90^{+0.10}_{-0.11}$ | 3.1 | 17 [0] | −23.61 | $10.5^{+2.0}_{-1.8}$ | $39.7^{+2.7}_{-2.8}$ | RM |
| LESS J033110.5−275233 | LESS 41 | 03$^{\rm h}$31$^{\rm m}$10$^{\rm s}$.09 | −27°52′36″.3 | $2.74^{+4.26}_{-0.91}$ | 0.0 | 4 [0] | −25.56 | <4.0 | <29.9 | I |
| LESS J033307.0−274801 | LESS 43 | 03$^{\rm h}$33$^{\rm m}$6$^{\rm s}$.63 | −27°48′1″.9 | $1.67^{+0.23}_{-0.14}$ | 2.0 | 8 [9] | −23.35 | <1.3 | <22.8 | MI |
| LESS J033131.0−273238 | LESS 44 | 03$^{\rm h}$31$^{\rm m}$31$^{\rm s}$.19 | −27°32′38″.6 | $2.49^{+0.00}_{-0.08}$ | 2.8 | 11 [0] | −24.82 | $14.8^{+1.7}_{-2.6}$ | $43.0^{+2.9}_{-3.1}$ | RM |
| LESS J033256.0−273317 | LESS 47 | 03$^{\rm h}$32$^{\rm m}$55$^{\rm s}$.99 | −27°33′18″.9 | $2.90^{+0.14}_{-0.42}$ | 1.5 | 8 [6] | −23.77 | <4.5 | <32.7 | MI |
| LESS J033237.8−273202 | LESS 48 | 03$^{\rm h}$32$^{\rm m}$38$^{\rm s}$.00 | −27°31′59″.4 | $1.91^{+0.36}_{-0.43}$ | 0.2 | 4 [1] | −24.57 | $7.5^{+4.8}_{-3.8}$ | $35.0^{+4.9}_{-5.8}$ | RM |
| LESS J033124.5−275040 | LESS 49a | 03$^{\rm h}$31$^{\rm m}$24$^{\rm s}$.45 | −27°50′37″.5 | $1.50^{+0.15}_{-0.10}$ | 5.0 | 12 [1] | −23.22 | $1.8^{+1.0}_{-0.6}$ | $25.0^{+2.6}_{-2.4}$ | RM |
| LESS J033124.5−275040 | LESS 49b | 03$^{\rm h}$31$^{\rm m}$24$^{\rm s}$.69 | −27°50′46″.4 | $3.31^{+0.22}_{-0.38}$ | 0.7 | 11 [2] | −24.13 | $35.9^{+8.5}_{-10.6}$ | $58.4^{+4.8}_{-6.4}$ | R |
| LESS J033141.2−274441 | LESS 50a | 03$^{\rm h}$31$^{\rm m}$41$^{\rm s}$.11 | −27°44′42″.4 | $0.85^{+0.16}_{-0.11}$ | 2.3 | 17 [0] | −21.91 | <0.3 | <15.9 | M |
| LESSJ033141.2−274441 | LESS 50b | 03$^{\rm h}$31$^{\rm m}$40$^{\rm s}$.97 | −27°44′34″.8 | $2.69^{+0.49}_{-0.25}$ | 7.6 | 11 [5] | −24.67 | $15.1^{+9.0}_{-4.1}$ | $45.6^{+6.7}_{-4.3}$ | RM |
| LESSJ033243.6−273353 | LESS 54 | 03$^{\rm h}$32$^{\rm m}$43$^{\rm s}$.62 | −27°33′56″.6 | $1.84^{+0.62}_{-0.25}$ | 3.7 | 7 [6] | −23.35 | <1.6 | <24.1 | M |
| LESSJ033153.2−273936 | LESS 56 | 03$^{\rm h}$31$^{\rm m}$53$^{\rm s}$.11 | −27°39′37″.3 | $2.46^{+0.41}_{-0.24}$ | 0.6 | 9 [8] | −24.38 | $5.1^{+3.8}_{-2.0}$ | $34.3^{+5.1}_{-3.9}$ | RM |
| LESSJ033152.0−275329 | LESS 57 | 03$^{\rm h}$31$^{\rm m}$51$^{\rm s}$.93 | −27°53′26″.8 | $2.94^{+0.14}_{-0.11}$ | 10.8 | 11 [6] | −24.26 | $11.8^{+3.1}_{-2.6}$ | $43.6^{+3.6}_{-3.5}$ | RM |
| LESSJ033303.9−274412 | LESS 59 | 03$^{\rm h}$33$^{\rm m}$3$^{\rm s}$.62 | −27°44′12″.6 | $1.40^{+0.29}_{-0.13}$ | 1.9 | 13 [4] | −23.52 | $1.3^{+1.2}_{-0.5}$ | $23.5^{+3.6}_{-2.5}$ | RM |
| LESSJ033317.5−275121 | LESS 60 | 03$^{\rm h}$33$^{\rm m}$17$^{\rm s}$.53 | −27°51′27″.5 | $1.64^{+0.10}_{-0.24}$ | 5.1 | 17 [0] | −24.01 | $4.0^{+1.1}_{-1.6}$ | $31.8^{+2.7}_{-3.8}$ | RM |
| LESSJ033236.4−273452 | LESS 62 | 03$^{\rm h}$32$^{\rm m}$36$^{\rm s}$.52 | −27°34′53″.0 | $1.52^{+0.10}_{-0.21}$ | 0.8 | 16 [1] | −24.45 | $7.9^{+1.7}_{-2.6}$ | $37.5^{+3.1}_{-4.2}$ | RM |
| LESSJ033308.5−280044 | LESS 63 | 03$^{\rm h}$33$^{\rm m}$8$^{\rm s}$.49 | −28°0′42″.8 | $1.39^{+0.07}_{-0.05}$ | 2.5 | 15 [1] | −23.50 | $1.3^{+0.6}_{-0.4}$ | $23.8^{+2.4}_{-2.4}$ | RM |
| LESSJ033201.0−280025 | LESS 64 | 03$^{\rm h}$32$^{\rm m}$0$^{\rm s}$.98 | −28°0′25″.3 | $4.19^{+0.04}_{-0.32}$ | 1.9 | 11 [4] | −24.31 | $12.4^{+4.4}_{-5.4}$ | $48.3^{+5.4}_{-6.1}$ | RM |
| LESSJ033331.7−275406 | LESS 66 | 03$^{\rm h}$33$^{\rm m}$31$^{\rm s}$.92 | −27°54′10″.3 | $2.39^{+0.04}_{-0.05}$ | 37.2 | 14 [0] | −25.78 | $10.0^{+1.8}_{-1.7}$ | $41.0^{+3.4}_{-3.4}$ | RM |

**Table 3** – *continued*

| SMG[a] | Short name | RA[b] | Dec.[b] | $z_{\rm phot}$[c] | $\chi^2_{\rm red}$[d] | Filters[e] | $M_H$[f] | $L_{\rm FIR}$[g] ($10^{12}\,{\rm L}_\odot$) | $T_{\rm D}$[h] (K) | ID type[i] |
|---|---|---|---|---|---|---|---|---|---|---|
| LESSJ033243.3−275517 | LESS 67 | $03^{\rm h}32^{\rm m}43\overset{\rm s}{.}18$ | $-27^\circ55'14\overset{''}{.}2$ | $2.27^{+0.05}_{-0.11}$ | 3.2 | 16 [1] | −24.82 | $11.9^{+1.6}_{-2.1}$ | $42.8^{+3.2}_{-3.4}$ | RM |
| LESSJ033144.0−273832 | LESS 70 | $03^{\rm h}31^{\rm m}43\overset{\rm s}{.}92$ | $-27^\circ38'35\overset{''}{.}2$ | $2.31^{+0.15}_{-0.06}$ | 3.8 | 17 [0] | −24.48 | $44.1^{+7.9}_{-3.7}$ | $61.0^{+5.2}_{-4.6}$ | RM |
| LESSJ033240.4−273802 | LESS 72 | $03^{\rm h}32^{\rm m}40\overset{\rm s}{.}05$ | $-27^\circ38'8\overset{''}{.}5$ | $0.86^{+0.04}_{-0.04}$ | 2.0 | 17 [0] | −23.46 | $0.5^{+0.2}_{-0.2}$ | $19.2^{+1.9}_{-1.9}$ | M |
| LESSJ033229.3−275619 | LESS 73 | $03^{\rm h}32^{\rm m}29\overset{\rm s}{.}28$ | $-27^\circ56'18\overset{''}{.}9$ | $4.61^{+0.94}_{-0.59}$ | 1.1 | 8 [9] | −24.42 | $12.3^{+12.2}_{-6.2}$ | $49.3^{+9.9}_{-7.6}$ | R |
| LESSJ033309.3−274809 | LESS 74a | $03^{\rm h}33^{\rm m}9\overset{\rm s}{.}34$ | $-27^\circ48'15\overset{''}{.}9$ | $1.84^{+0.32}_{-0.49}$ | 0.9 | 10 [6] | −23.49 | $2.8^{+2.2}_{-1.8}$ | $29.2^{+4.3}_{-5.8}$ | RI |
| LESSJ033309.3−274809 | LESS 74b | $03^{\rm h}33^{\rm m}9\overset{\rm s}{.}14$ | $-27^\circ48'16\overset{''}{.}6$ | $1.71^{+0.20}_{-0.17}$ | 2.5 | 10 [6] | −23.29 | $3.0^{+1.6}_{-1.1}$ | $29.6^{+3.4}_{-3.1}$ | RI |
| LESSJ033126.8−275554 | LESS 75 | $03^{\rm h}31^{\rm m}27\overset{\rm s}{.}17$ | $-27^\circ55'50\overset{''}{.}9$ | $2.46^{+0.06}_{-0.09}$ | 33.2 | 15 [0] | −25.39 | $11.5^{+2.1}_{-2.2}$ | $43.1^{+3.4}_{-3.5}$ | RM |
| LESS J033340.3−273956 | LESS 78 | $03^{\rm h}33^{\rm m}40\overset{\rm s}{.}16$ | $-27^\circ39'48\overset{''}{.}7$ | $2.12^{+0.32}_{-0.34}$ | 2.3 | 12 [1] | −24.42 | $8.5^{+4.9}_{-3.6}$ | $39.2^{+5.5}_{-5.6}$ | R |
| LESS J033221.3−275623 | LESS 79 | $03^{\rm h}32^{\rm m}21\overset{\rm s}{.}61$ | $-27^\circ56'23\overset{''}{.}1$ | $1.41^{+0.23}_{-0.17}$ | 2.2 | 16 [1] | −23.89 | $1.5^{+1.1}_{-0.6}$ | $25.4^{+3.4}_{-3.0}$ | RM |
| LESS J033127.5−274440 | LESS 81 | $03^{\rm h}31^{\rm m}27\overset{\rm s}{.}54$ | $-27^\circ44'39\overset{''}{.}5$ | $2.23^{+0.13}_{-0.15}$ | 27.9 | 14 [1] | −24.89 | $27.7^{+5.0}_{-4.9}$ | $54.4^{+5.0}_{-5.1}$ | RM |
| LESS J033154.2−275109 | LESS 84 | $03^{\rm h}31^{\rm m}54\overset{\rm s}{.}49$ | $-27^\circ51'5\overset{''}{.}3$ | $2.29^{+0.15}_{-0.07}$ | 3.6 | 14 [3] | −24.14 | $4.5^{+1.8}_{-1.2}$ | $34.5^{+3.6}_{-3.4}$ | I |
| LESS J033251.1−273143 | LESS 87 | $03^{\rm h}32^{\rm m}50\overset{\rm s}{.}83$ | $-27^\circ31'41\overset{''}{.}2$ | $3.20^{+0.10}_{-0.81}$ | 0.1 | 5 [0] | −24.84 | $37.0^{+5.6}_{-19.3}$ | $60.1^{+5.9}_{-12.9}$ | RM |
| LESS J033155.2−275345 | LESS 88 | $03^{\rm h}31^{\rm m}54\overset{\rm s}{.}81$ | $-27^\circ53'40\overset{''}{.}9$ | $2.35^{+0.11}_{-0.10}$ | 1.1 | 16 [1] | −24.37 | $11.2^{+2.3}_{-1.9}$ | $44.0^{+4.0}_{-3.9}$ | R |
| LESS J033313.0−275556 | LESS 96 | $03^{\rm h}33^{\rm m}12\overset{\rm s}{.}62$ | $-27^\circ55'51\overset{''}{.}6$ | $2.71^{+0.03}_{-0.09}$ | 22.0 | 17 [0] | −26.30 | $16.0^{+1.9}_{-2.5}$ | $49.7^{+4.4}_{-4.5}$ | RM |
| LESS J033130.2−275726 | LESS 98 | $03^{\rm h}31^{\rm m}29\overset{\rm s}{.}89$ | $-27^\circ57'22\overset{''}{.}4$ | $1.55^{+0.17}_{-0.16}$ | 1.0 | 10 [4] | −24.40 | $7.8^{+2.8}_{-2.1}$ | $39.9^{+4.4}_{-4.3}$ | RM |
| LESS J033151.5−274552 | LESS 101 | $03^{\rm h}31^{\rm m}51\overset{\rm s}{.}53$ | $-27^\circ45'53\overset{''}{.}1$ | $2.39^{+0.36}_{-0.52}$ | 2.5 | 10 [7] | −23.51 | $3.8^{+2.9}_{-2.3}$ | $33.8^{+5.3}_{-6.5}$ | R |
| LESS J033335.6−274020 | LESS 102 | $03^{\rm h}33^{\rm m}35\overset{\rm s}{.}56$ | $-27^\circ40'23\overset{''}{.}2$ | $1.68^{+0.13}_{-0.25}$ | 1.1 | 11 [2] | −24.34 | <1.3 | <24.9 | M |
| LESS J033325.4−273400 | LESS 103 | $03^{\rm h}33^{\rm m}25\overset{\rm s}{.}37$ | $-27^\circ33'58\overset{''}{.}5$ | $1.84^{+0.59}_{-0.87}$ | 0.3 | 5 [7] | −23.44 | <1.6 | <26.3 | M |
| LESS J033140.1−275631 | LESS 106 | $03^{\rm h}31^{\rm m}40\overset{\rm s}{.}17$ | $-27^\circ56'22\overset{''}{.}4$ | $1.96^{+0.31}_{-0.48}$ | 2.1 | 11 [5] | −25.00 | $6.3^{+3.5}_{-3.4}$ | $38.5^{+5.4}_{-7.2}$ | RI |
| LESS J033316.4−275033 | LESS 108 | $03^{\rm h}33^{\rm m}16\overset{\rm s}{.}51$ | $-27^\circ50'39\overset{''}{.}3$ | $0.20^{+0.03}_{-0.05}$ | 6.3 | 15 [0] | −22.75 | $0.2^{+0.1}_{-0.1}$ | $24.5^{+2.3}_{-2.4}$ | RM |
| LESS J033122.6−275417 | LESS 110 | $03^{\rm h}31^{\rm m}22\overset{\rm s}{.}63$ | $-27^\circ54'17\overset{''}{.}0$ | $2.35^{+4.65}_{-0.44}$ | 0.0 | 4 [0] | −23.22 | <2.8 | <31.4 | MI |
| LESS J033325.6−273423 | LESS 111 | $03^{\rm h}33^{\rm m}25\overset{\rm s}{.}21$ | $-27^\circ34'25\overset{''}{.}9$ | $2.61^{+0.14}_{-0.06}$ | 14.4 | 13 [0] | −24.49 | $9.8^{+3.4}_{-2.3}$ | $44.1^{+5.0}_{-4.8}$ | RM |
| LESS J033249.3−273112 | LESS 112 | $03^{\rm h}32^{\rm m}48\overset{\rm s}{.}85$ | $-27^\circ31'12\overset{''}{.}8$ | $1.81^{+0.42}_{-0.30}$ | 0.7 | 5 [0] | −24.02 | $2.3^{+2.5}_{-1.2}$ | $28.5^{+5.8}_{-4.9}$ | RI |
| LESS J033150.8−274438 | LESS 114 | $03^{\rm h}31^{\rm m}51\overset{\rm s}{.}08$ | $-27^\circ44'37\overset{''}{.}0$ | $1.57^{+0.08}_{-0.07}$ | 1.6 | 17 [0] | −24.61 | $5.3^{+1.1}_{-0.9}$ | $36.8^{+3.7}_{-3.7}$ | RM |
| LESS J033349.7−274239 | LESS 115 | $03^{\rm h}33^{\rm m}49\overset{\rm s}{.}66$ | $-27^\circ42'34\overset{''}{.}0$ | $4.75^{+2.25}_{-3.29}$ | 0.0 | 2 [0] | −25.65 | <13.5 | <52.3 | I |
| LESS J033128.0−273925 | LESS 117 | $03^{\rm h}31^{\rm m}27\overset{\rm s}{.}62$ | $-27^\circ39'27\overset{''}{.}3$ | $1.73^{+0.29}_{-0.34}$ | 3.3 | 9 [4] | −24.23 | $5.7^{+3.4}_{-2.6}$ | $37.7^{+5.5}_{-6.0}$ | R |
| LESS J033121.8−274936 | LESS 118 | $03^{\rm h}31^{\rm m}21\overset{\rm s}{.}91$ | $-27^\circ49'34\overset{''}{.}0$ | $2.17^{+4.83}_{-1.49}$ | 1.7 | 5 [1] | −22.21 | $2.8^{+47.5}_{-2.7}$ | $31.8^{+48.7}_{-15.6}$ | R |
| LESS J033328.5−275655 | LESS 120 | $03^{\rm h}33^{\rm m}28\overset{\rm s}{.}55$ | $-27^\circ56'54\overset{''}{.}1$ | $1.43^{+0.30}_{-0.21}$ | 2.2 | 13 [3] | −23.41 | $2.1^{+1.8}_{-0.9}$ | $29.2^{+5.0}_{-4.3}$ | RM |
| LESS J033139.6−274120 | LESS 122 | $03^{\rm h}31^{\rm m}39\overset{\rm s}{.}52$ | $-27^\circ41'19\overset{''}{.}4$ | $2.08^{+0.08}_{-0.08}$ | 5.2 | 17 [0] | −25.14 | $22.4^{+2.8}_{-2.7}$ | $55.2^{+6.2}_{-6.2}$ | RM |
| LESS J033209.8−274102 | LESS 126 | $03^{\rm h}32^{\rm m}9\overset{\rm s}{.}60$ | $-27^\circ41'6\overset{''}{.}9$ | $2.02^{+0.17}_{-0.13}$ | 2.4 | 12 [4] | −23.84 | $2.3^{+1.3}_{-0.9}$ | $30.6^{+4.2}_{-4.1}$ | MI |

[a]The SMG names correspond to those in Weiß et al. (2009) and Biggs et al. (2011).
[b]Coordinates are the J2000 position of the optical/near-IR counterpart.
[c]Since HYPERZ was restricted to $0 < z < 7$, the five galaxies whose upper redshift limits yield a formal maximum redshift of $z_{\rm max} = 7$ are actually only constrained in the lower redshift limit. Therefore, throughout this paper, the redshifts of these galaxies are plotted as lower limits.
[d]The reduced $\chi^2$ of the best-fitting SED at the derived photometric redshift.
[e]The number of photometric filters in which each SMG counterpart was detected (and the number of filters in which the SMG was observed but not detected, providing a limiting flux).
[f]$M_H$ is the absolute magnitude in the rest-frame $H$ band.
[g]As discussed in Section 5.7, the FIR luminosity ($L_{\rm FIR}$) is derived from the IR–radio correlation using the radio flux and the photometric redshift of each SMG.
[h]The characteristic dust temperature ($T_{\rm D}$) is derived as discussed in Section 5.7 from radio and submillimetre fluxes and the photometric redshift of each SMG.
[i]ID types R, M and I indicate radio, 24-μm and IRAC-identified counterparts, respectively (see Biggs et al. 2011 for details).
[j]As shown in Section 5.1, LESS 20 appears to contain a radio-loud AGN. Therefore, $L_{\rm FIR}$ and $T_{\rm D}$ presented here are likely significantly overestimated due to the AGN contribution to the radio flux, as such LESS 20 is excluded from our studies of the luminosity function, SFR and star formation history of SMGs (Section 5.7).

a more extensive comparison using a larger sample of SMGs with redshifts, from the ongoing VLT large programme (Danielson et al., in preparation), confirms the results that we derive here.

To assess the level of systematic uncertainties in the derived photometric redshifts due to the adopted methodology, SED templates, and/or photometric data, we also use ZEBRA (Zurich Extragalactic Bayesian Redshift Analyzer; Feldmann et al. 2006) to independently calculate photometric redshifts. Our adopted procedure is similar to that discussed in section 3.2 of Luo et al. (2010). Briefly, we use ZEBRA to obtain a maximum-likelihood estimate for the photometric redshifts of individual galaxies or AGNs using an initial set of 265 galaxies, AGNs and galaxy–AGN hybrid SED templates. These SED templates were then expanded to 463 templates during the template-training mode of ZEBRA to best represent the SEDs of the ≈2 Ms X-ray sources (Luo et al. 2010), including AGNs. Besides the different SED templates used, this method differs from the HYPERZ approach described in Section 4.1 in some additional details such as how the redshift intervals and minimum

photometric errors are determined (see section 3.2 of Luo et al. 2010 for details).

The ZEBRA-derived photometric redshifts ($z_{\rm phot,check}$) were compared to those listed in Table 3 ($z_{\rm phot}$); the difference was measured by $\delta z_{\rm phot} = (z_{\rm phot,check} - z_{\rm phot})/(1 + z_{\rm phot})$. For sources with secure spectroscopic redshifts, individual $|\delta z_{\rm phot}|$ values range from $\approx$0.01 to 0.10, indicating that both methods are able to deliver photometric redshifts to a similar accuracy. For the full sample, the mean (median) value of $\delta z_{\rm phot}$ is $-0.006$ (0.011), with an rms scatter of 0.028, suggesting that the photometric redshifts in Table 3 are fairly robust. After accounting for the effective $1\sigma$ errors of the photometric redshifts, only three (sources LESS 7, LESS 37 and LESS 111) of the 78 sources have inconsistent $z_{\rm phot}$ and $z_{\rm phot,check}$. As some sources have photometry data in addition to those presented in Table 3, we also tested the effect of including more data points. The photometric redshifts differ by a mean value of $|\delta z_{\rm phot}|$ of 0.024 with an rms error of 0.030, after including the WFI *R*-band data (Giacconi et al. 2002; Giavalisco et al. 2004) for 25 sources and the *GALEX* near-ultraviolet (near-UV) and far-UV data (Morrissey et al. 2007) for three sources. Given the small difference caused by the additional data, we consider the consistent aperture photometry in Table 2 suitable for the purpose of deriving reliable photometric redshifts.

Finally, we perform two checks of our photometric redshifts against two independent analyses. Dunlop et al. (2010) have independently calculated photometric redshifts for the six LESS SMGs (five with robust counterparts) in the GOODS-South that were also detected by the *Balloon-borne Large Aperture Submillimeter Telescope* (*BLAST*) at 250 μm (Devlin et al. 2009). Their analysis uses the photometry from the *HST* ($B_{435}$, $V_{606}$, $i_{775}$, $z_{850}$), ISAAC on the VLT (*J*, *H*, *K*) and *Spitzer* (3.6, 4.5, 5.8 and 8 μm), and they use HYPERZ with the stellar population models of Charlot & Bruzual (e.g. Bruzual 2007), which have a Salpeter initial mass function (IMF). In all cases, the Dunlop et al. (2010) photometric redshifts agree within their errors with those presented in Table 3, providing further confidence that our photometric redshifts are reasonable for SMGs.

Similarly, Cardamone et al. (2010) recently used photometry in 18 medium bands and 14 broad bands to calculate 32-band photometric redshifts for ∼40 000 optically selected galaxies in the ECDF-S. Nine of these galaxies correspond to robust LESS SMG counterparts (within 1 arcsec) and the photometric redshifts of seven out of the nine galaxies are in good agreement with this work. The outliers are LESS 70, which has a spectroscopic redshift (Danielson et al., in preparation) that agrees with our photometric redshift, and LESS 39.

### 4.3 The effect of AGNs on photometric redshifts

As discussed in Section 4.1, our photometric redshift calculations are based on fitting stellar templates to the SMG photometry. However, studies have shown that the 8-μm flux in SMGs with a luminous AGN component can be dominated by the AGN and therefore fitting stellar templates may yield misleading results (Hainline et al. 2009, 2011; Coppin et al. 2010b).

We employ two methods to identify potential AGNs in the LESS SMGs. First, we cross-correlate the LESS SMG counterparts with the *Chandra* X-ray catalogues of the CDF-S (Luo et al. 2008) and ECDF-S (Lehmer et al. 2005). The Lehmer et al. (2005) catalogue contains ∼800 sources detected in a mosaic of *Chandra* 250-ks pointings covering the ECDF-S, and the Luo et al. (2008) catalogue details ∼500 sources detected in 2 Ms of *Chandra* exposure on the smaller CDF-S. We use a radius of 1 arcsec to match the *Chandra* and LESS counterparts, and find 12 X-ray luminous SMGs – five in the ECDF-S, three in the CDF-S and four are detected in both fields, due to an overlap between the observations. Secondly, we identify nine SMG counterparts (12 per cent of the robust LESS counterparts) with a large excess of 8-μm flux compared to the best-fitting SED template (Appendix B), which potentially indicates obscured power-law emission from an AGN [or emission from hot dust or polycyclic aromatic hydrocarbons (PAHs) powered by star formation]. In total, this yields 15 SMG counterparts (22 per cent of the robust LESS counterparts) which may contain AGNs (six are both X-ray detected and have an 8-μm excess). We discuss these individual sources in Appendix A.

The photometric redshifts of the four potential LESS AGNs that have available spectroscopic redshifts are not systematically offset from the spectroscopic values; the median $\Delta z/(1 + z) = -0.088 \pm 0.071$, which is consistent with the whole sample (Section 4.2). A more extensive comparison using the results of our ongoing VLT survey (Danielson et al., in preparation) supports this conclusion to determine whether the power-law contamination in the 8-μm filter reduces the accuracy of our photometric redshift estimates. We refit the photometry of the counterparts which display an 8-μm excess whilst excluding the 8-μm photometry. Spectroscopic redshifts are available for three of the affected galaxies and we find that the average $|\Delta z|$ of these eight galaxies is not significantly changed, while the median reduced $\chi^2$ drops by ∼1, when the 8-μm photometry is excluded from the fitting. This result does not change if we also exclude the 8-μm photometry of the SMGs which are X-ray detected.

It is also possible that our sample of SMG counterparts contains AGNs which enhance the 8-μm flux but do not cause a detectable excess. Therefore, we also exclude the 8-μm photometry of *all* the SMG counterparts during the fitting procedure. Once again the average $|\Delta z|$ for the spectroscopic sample does not change significantly [median $\Delta z/(1 + z) = 0.033 \pm 0.040$, compared to median $\Delta z/(1 + z) = 0.023 \pm 0.042$ originally]. These results indicate that when calculating photometric redshifts the benefit of including the longer wavelength data is greater than the bias which is removed by ignoring the 8-μm photometry. Therefore, we include the 8-μm photometry in our SED fitting.

### 4.4 Reliability of SED parameters

In addition to calculating photometric redshifts, HYPERZ also returns the spectral type, age and reddening of the best-fitting SED template. To test the sensitivity of the choice of templates, we allow redshifts in the range $z = 0$–7 and refit the photometry of the SMGs allowing only the Burst template, and then only a constant SFR history. These two templates represent the extremes of the star formation histories and so they will allow us to gauge the sensitivity of the derived parameters to the choice of the best-fitting template.

We compare the quality of the Burst and CSF fits of each galaxy with $\Delta\chi^2_{\rm red}$ – the difference in the reduced $\chi^2$ of the Burst and CSF fits. We find that 63 per cent of the SMGs have $|\Delta\chi^2_{\rm red}| \leq 1$ and as such the Burst and CSF templates are indistinguishable at the 99 per cent level for these SMGs. 61 per cent (17) of the SMGs with $|\Delta\chi^2_{\rm red}| > 1$ between the two template fits are best fitted by Bursts and 39 per cent (11) by CSF templates. If three templates – Burst, Sb and CSF – are considered, then the star formation histories of only 23 per cent (17) of all the SMG counterparts can be distinguished. Therefore, although it may be possible to crudely distinguish the

star formation histories of a fraction (∼20–40 per cent) of SMG counterparts with HYPERZ, the star formation histories of most SMG counterparts cannot be reliably established.

We find that the SMGs that have SED fits with $|\Delta\chi^2_{\rm red}| \leq 1$ and can be equally well fitted by either Burst or CSF templates have different age estimates depending on the template. The age and star formation history of a stellar population affects the light-to-mass ratio; thus our inability to distinguish between star formation histories leads to uncertainties in the light-to-mass ratios and stellar mass estimates. Using the *H*-band light-to-mass ratios for Burst and CSF models from the STARBURST99 stellar population model (Leitherer et al. 1999), we calculate that the uncertainties in SED fitting parameters result in a $1\sigma$ dispersion of a factor of 4.6 range in the light-to-mass ratios. This factor of 4.6 is the range from the smallest to the largest applicable light-to-mass ratios and consequently results in a $1\sigma$ uncertainty range of a factor of 4.6 × in the stellar mass estimates (see also Fig. 9 shown later).

We also compare reddening measurements for those galaxies with SED fits with $|\Delta\chi^2| \leq 1$ and find that on average the difference between $A_V$ for the best-fitting CSF and Burst templates, $\Delta A_V$, is equal to $0.32 \pm 0.16$. Since average estimates based on either template return the same value of $A_V$ (to $\sim 2\sigma$), we conclude that average reddening measurements for the SMG population are not strongly sensitive to the adopted star formation history and are likely to be statistically meaningful (although we caution against trusting values for individual SMGs). When fitting E, Sb, Burst or CSF templates and allowing $A_V = 0$–5, as in our photometric redshift calculations, we determine a median $A_V = 1.5 \pm 0.1$, and 96 per cent of SMGs have $A_V \leq 3$. We conclude that in most instances restricting to $A_V \leq 3$ is sufficient for calculating photometric redshifts of SMGs. We note that these values of $A_V$ are integrated across the whole galaxy and that the obscuration in the regions responsible for the majority of the FIR/submillimetre emission is considerably larger (e.g. Chapman et al. 2004b; Takata et al. 2006; Ivison et al. 2010b).

## 5 RESULTS AND DISCUSSION

In Section 4, we derived reliable photometric redshifts for 78 counterparts to 72 robustly identified SMGs. We now use these photometric redshifts and the SED fits to further investigate the properties of SMGs.

### 5.1 Photometric redshifts

In Fig. 2, we show our photometric redshift distribution for the 78 robust SMG counterparts; it peaks at $z = 2.2 \pm 0.1$, with $\sigma = 0.9$. We compare to the photometric redshift distribution of SMG counterparts in the SCUBA Half-Degree Extragalactic Survey (SHADES) (Clements et al. 2008; Dye et al. 2008), median $z = 1.5 \pm 0.1$, and the spectroscopic sample from Chapman et al. (2005), median $z = 2.2 \pm 0.1$, both of which have similar submillimetre flux limits to our survey. The LESS SMGs have a similar redshift distribution to Chapman et al. (2005), although in the LESS the spectroscopic 'redshift desert' at $z \sim 1.2$–1.8 is filled and there is a larger high-redshift tail. The redshift distributions of both LESS and Chapman et al. (2005) SMGs are peaked at higher redshifts than the SHADES SMGs. The Kolmogorov–Smirnov test (KS test) calculates the probability that two samples are drawn from the same parent population ($P_{\rm KS}$). A KS test between Chapman et al. (2005) and LESS SMGs yields $P_{\rm KS} = 0.54$, suggesting that the two samples are consistent with being drawn from the same parent population. However, a KS test between the LESS and SHADES SMGs gives $P_{\rm KS} = 2.1 \times 10^{-5}$ indicating that these samples are not consistent with being drawn from the same underlying population.

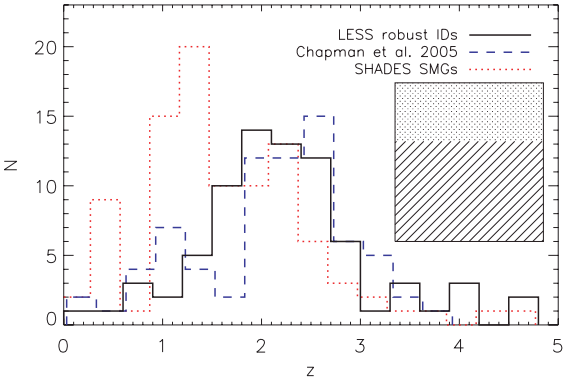


**Figure 2.** The photometric redshift distribution of the LESS SMGs. We compare this to the photometric redshift distribution of SHADES SMG counterparts (Clements et al. 2008; Dye et al. 2008), and the spectroscopic redshift distribution of SMGs from Chapman et al. (2005); for clarity the SHADES and Chapman et al. (2005) samples are offset slightly in redshift. The median redshift of identified SMGs in LESS is $z = 2.2 \pm 0.1$, which is the same as that from the Chapman et al. (2005) spectroscopic survey; SHADES has a lower median redshift of $z = 1.5 \pm 0.1$. There is a slightly larger high-redshift tail in the LESS SMG population than the Chapman et al. (2005) SMG population. Additionally, the so-called 'redshift desert' at $z \sim 1.5$, which is evident in the Chapman et al. (2005) study does not affect our photometric redshifts and as such, in contrast with Chapman et al. (2005), the increase in the number of galaxies from $z \sim 1$ to $z \sim 2$ is smooth. Statistical comparisons show that the Chapman et al. (2005) and LESS SMGs are most likely drawn from populations with similar redshift distributions, but that the SHADES SMGs are biased to low redshifts either from systematic errors in the photometric redshift calculations, sample selection, or cosmic variance. The shaded region represents the area that would be added to the histogram were the redshifts of the 54 statistically identified or completely unidentified SMGs known and is designed to give an impression of the potential contribution of the unidentified SMGs to this figure. The lower region corresponds to the unidentified SMGs that we statistically identify in Section 5.3, and which have redshifts similar to the identified SMGs. The upper shaded region represents the SMGs which remain unaccounted for after the statistical analysis and likely have $z \gtrsim 3$.

We conclude that the global properties of our photometric redshifts are consistent with the largest previous spectroscopic survey, albeit with a higher redshift tail – we find 11 (14 per cent) SMGs with $z \geq 3$ and nine (12 per cent) with $z \geq 3.5$, of which LESS 73 is spectroscopically confirmed at $z = 4.76$ (see Coppin et al. 2009, 2010a). It is likely that the larger number of high-redshift sources in the LESS compared to Chapman et al. (2005), where there are 10 per cent at $z \geq 3$ and just 1 per cent at $z \geq 3.5$, is due to deeper radio data (on average), the inclusion of 24-μm counterparts in the LESS (Biggs et al. 2011) and most critically the use of photometric redshifts covering the UV to mid-IR which are less reliant on the detection of spectral emission lines in the optical. Conversely, the SHADES SMGs appear to typically lie at lower redshifts. We stress that compared to the SHADES analyses we have used about twice as many photometric bands, tested against a spectroscopic sample of SMGs, and obtained qualitatively better fits to the SEDs. We suggest that either there is a systematic error in the original SHADES photometric redshifts or their counterpart identifications, or that cosmic variance is the cause of the different redshift distributions. However, we note that a reanalysis of the optical to IR photometry of the SHADES SMGs yields a median photometric

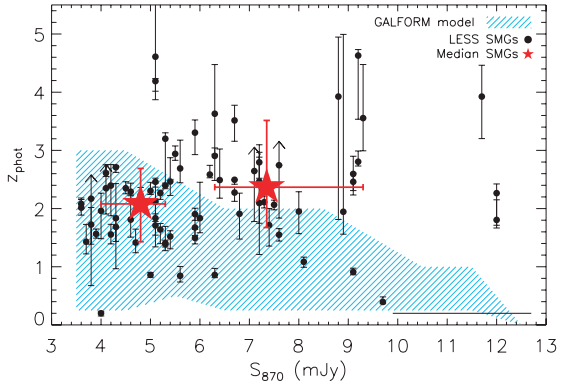


**Figure 3.** Photometric redshift versus submillimetre flux for LESS SMGs; the median $S_{870\,\mu m}$ error bar is shown in the bottom right. The median $S_{870\,\mu m}$ and redshift, with $1\sigma$ error bars, are presented for SMGs with $S_{870\,\mu m} \leq 5.6$ mJy and $S_{870\,\mu m} > 5.6$ mJy. Previous studies have suggested that the brightest SMGs may lie at the highest redshifts. This work contains optical to IR photometric redshifts for a larger sample of SMGs than previous studies of the phenomenon and finds no evidence for a trend. For comparison, we also highlight the $1\sigma$ distribution of SMGs in flux bins of 1 mJy in the ΛCDM GALFORM model (Baugh et al. 2005; Lacey et al. 2008; Swinbank et al. 2008).

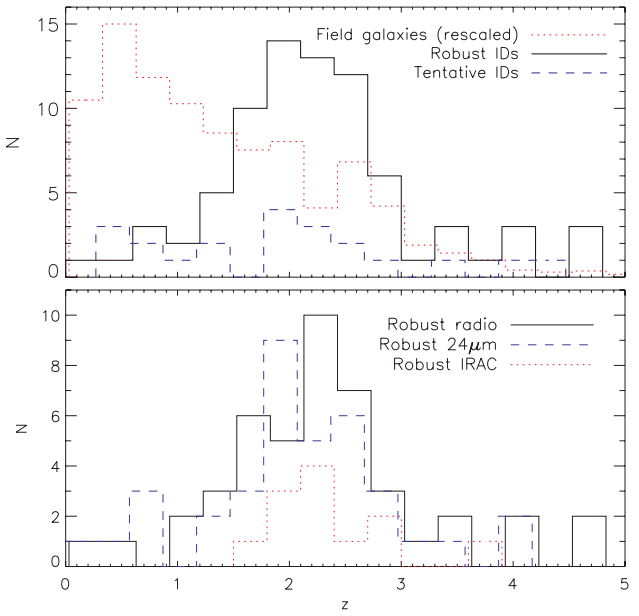


**Figure 4.** In the top panel, we present a comparison between robustly and tentatively identified SMG counterparts and the field population of the ECDF-S; tentative counterparts and field galaxies are offset slightly in redshift for clarity. The robust counterparts have a median redshift of $z = 2.2 \pm 0.1$, compared to $z = 2.0 \pm 0.3$ for the tentative counterparts. Tentative counterparts have a larger standard deviation – 1.2 compared to 0.9 for the robust SMG counterparts. We interpret these distributions as evidence that tentative counterparts are mainly drawn from the same parent population as the robust counterparts, but with the addition of some contamination, particularly at low redshifts. In the lower panel, we compare the redshift distributions of robust counterparts (with $p \leq 0.05$) in radio, 24-μm and IRAC data; for clarity, radio and 24-μm counterparts are plotted offset slightly in redshift. The radio, 24-μm and IRAC samples have the median redshifts of $2.3 \pm 0.1$, $2.1 \pm 0.2$ and $2.3 \pm 0.2$, and standard deviations of 0.9, 0.9 and 0.7, respectively. Therefore, we find no significant differences in the redshift distributions of the three identification methods.

redshift of $z = 2.05$ (Schael et al., in preparation) – more similar to the LESS and Chapman et al. (2005) than the original SHADES analyses. In addition, an analysis of optical to millimetre SEDs of SHADES galaxies in the Lockman Hole yields a median redshift of $z = 2.6 \pm 0.3$ (Serjeant et al. 2010).

Studies have suggested that the brightest SMGs may have higher redshifts than those with lower submillimetre fluxes (e.g. Ivison et al. 2002; Pope et al. 2005; Biggs et al. 2011). In Fig. 3, we plot the photometric redshift against 870-μm flux ($S_{870\,\mu m}$) for robust LESS SMG counterparts. We split the galaxies into those brighter and fainter than the median deboosted submillimetre flux of the sample, $S_{870\,\mu m} = 5.6$ mJy (we use deboosted 870-μm fluxes throughout). SMGs with $S_{870\,\mu m} \leq 5.6$ mJy have a median redshift of $z = 2.1 \pm 0.2$ and SMGs with $S_{870\,\mu m} > 5.6$ mJy have a median redshift of $z = 2.3 \pm 0.2$, where the errors are bootstrap uncertainties on the medians. Spearman's rank correlation coefficient between $S_{870\,\mu m}$ and $z_{phot}$ is 0.23, which corresponds to a probability of zero correlation of 0.04 and indicates that there is no significant correlation between the submillimetre flux and redshift for SMGs in our sample across their full observed redshift range. We have verified that the result is not dependent on the choice of the flux limit between the two bins. Additionally, if all the unidentified SMGs lie at $z = 5$ or 1 (in Section 5.3 both of these scenarios are shown to be unlikely), then we still find no statistically significant difference between the redshifts of SMGs in the two flux bins. The sample of SMGs with optical to IR photometric redshifts in this work is larger than that of previous studies of this phenomenon, and our analysis finds no significant correlation between $S_{870\,\mu m}$ and redshift for robustly identified sources, also implying that $S_{870\,\mu m}$ is not a good proxy for redshift. This result agrees with Knudsen et al. (2010) who find no difference in the redshift distributions of faint lensed SMGs ($S_{850\,\mu m} < 2$ mJy) and the brighter ($S_{850\,\mu m} \gtrsim 3$ mJy) SMGs from Chapman et al. (2005), and with the *Herschel* PACS analysis of 850-μm sources by Dannerbauer et al. (2010). We note that SMGs in the semianalytic ΛCDM GALFORM model (Baugh et al. 2005; Lacey et al. 2008; Swinbank et al. 2008) also show no correlation between $S_{870\,\mu m}$ and redshift (although the error range decreases at high fluxes where there are few galaxies in the model).

### 5.2 Sample subsets

As discussed in Section 1, Biggs et al. (2011) identified robust counterparts to 75 SMGs (of which 72 have detectable optical counterparts) and tentative counterparts to 18 LESS SMGs. In Fig. 4, we compare the photometric redshift distributions of the robust and tentative counterparts to determine whether our results may be biased by the exclusion of tentative counterparts in our main analysis. The median redshifts of robust and tentative counterparts are $2.2 \pm 0.1$ and $2.0 \pm 0.3$, and they have standard deviations of 0.9 and 1.2, respectively. We also use a KS test to compare the redshift distributions of robust and tentative counterparts statistically. We find $P_{KS} = 0.098$ and conclude that it is likely that there is some contamination from physically unassociated foreground ($z \lesssim 1$) galaxies in the tentative identifications. Therefore, we conclude that our analysis is less biased by restricting it to robust counterparts than it would be by including tentative counterparts.

We note that our identified sample contains two potential gravitational lenses (LESS 6 and LESS 111). These are low-redshift counterparts where the radio or mid-IR emission is offset from the optical source. These are discussed individually in Appendix A and we have confirmed that their inclusion does not affect our results.

In Fig. 4, we also compare the redshift distributions of counterparts with $p \leq 0.05$ in the radio, 24-μm and IRAC data. The median redshifts are $z = 2.3 \pm 0.1$, $2.1 \pm 0.2$ and $2.2 \pm 0.2$, and the

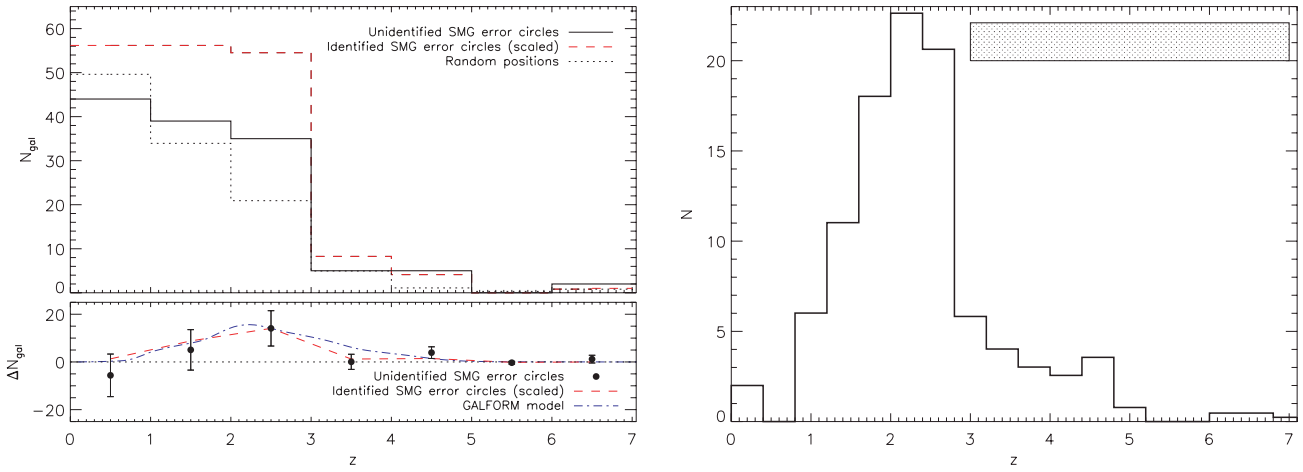


**Figure 5.** Left-hand side: the top panel shows the redshift histogram of sources within the submillimetre positional error circles of SMGs without robust radio, 24-μm or IRAC counterparts compared to the same number of random positions in the field. For comparison, we also plot the redshift histogram for sources in the submillimetre positional error circles of SMGs *with* robust counterparts, also scaled to the same number of error circles. In the bottom panel, we show the difference between the redshift histogram of galaxies around unidentified SMGs and the field population (from random positions). We also plot both the difference in the redshift of galaxies around identified SMGs and the field population, and the redshift distribution of radio-undetected SMGs in the ΛCDM GALFORM model (Swinbank et al. 2008). In order to highlight potential differences in the redshift distributions of the populations, the latter two data sets are scaled to match the value of $\Delta N_{\rm gal}$ of unidentified SMGs in the $z = 2$–3 bin. By using $\Delta N_{\rm gal}$ and assuming a uniform distribution of galaxies within the bins, we calculate that the average redshift of unidentified SMGs is $z = 2.5 \pm 0.2$. Right-hand side: the most likely redshift distribution of all LESS SMGs. The photometric redshift distribution of identified SMGs (Fig. 2) is combined with the statistically unidentified SMG population from the left-hand panels. The statistically unidentified SMGs are distributed uniformly within the relevant $\Delta z = 1$ ranges. The shaded area represents the remaining unidentified SMGs, which are likely to lie at $z \gtrsim 3$. We conclude that the median redshift of the $S_{870\,\mu{\rm m}} \gtrsim 4$ mJy SMG population is likely to be $z = 2.5 \pm 0.5$.

standard deviations are 0.9, 0.9 and 0.7 for the radio, 24-μm and IRAC samples, respectively. A comparison of the three redshift samples shows that they are statistically indistinguishable. We conclude that the three counterpart identification methods select galaxies with similar redshift distributions, and are not significantly biased with respect to each other.

### 5.3 Redshift distribution of unidentified SMGs

To date, redshift surveys of SMGs have focused on the ∼60–80 per cent of the population with counterparts identified from radio and 24-μm imaging, and a few located using high-resolution (sub-)millimetre interferometry. The requirement for radio or IR counterparts to SMGs can bias the redshift or the dust temperature distributions of identified SMGs (Chapman et al. 2005) and it is currently unknown if the identified population is representative of the ∼20–40 per cent of SMGs without identified counterparts. In particular, it is unclear whether they have the same redshift distribution. In order to investigate the redshift distribution of the unidentified SMGs, we utilize our extensive 17-band photometric redshifts in the ECDF-S to investigate the photometric redshifts of sources around SMGs without robustly identified counterparts to the field population.

In Fig. 5, we show the redshift histogram of galaxies within the error circles of the 51 unidentified SMGs in the ECDF-S, where the region considered is that used by Biggs et al. (2011) to identify SMG counterparts (both the completely unidentified and those with only tentative identifications). For comparison, we show the redshift histogram of all the galaxies in the submillimetre error circles of SMGs with robustly identified counterparts, scaled such that the number of error circles examined is the same as that of the unidentified SMG sample. We also consider the photometric redshifts of galaxies in the same area around random positions in the field, which are required to be >15 arcsec from any LESS SMGs. We consider 500 Monte Carlo simulations of 51 random field positions (equal to the number of unidentified SMGs), and employ the mean and standard deviations of the 500 simulations in each redshift bin for our statistical analyses. As discussed in Section 3, our photometric source extraction procedure included manually examining the regions around the SMGs and adding to the catalogue potential sources which may have been missed by the automated procedure. To remove any bias and ensure a fair comparison between the SMGs and random positions, we exclude these additional sources from this analysis.

In the lower left-hand panel of Fig. 5, we show the difference between the redshift distributions of the field and SMGs without robustly identified counterparts. Compared to the field, there is a tentative excess of 24 ± 12 at $z > 1$ around unidentified SMGs. There are tentative positive excesses of galaxies in the $z = 2$–3 (14 ± 7) and 4–5 (4 ± 2) bins around unidentified SMGs. The number of galaxies with $z = 2$–3 or 4–5 around the SMGs is not equalled or exceeded by *any* of the 500 Monte Carlo simulations, indicating that the probability of observing excesses of the magnitude of either of these by chance is <0.2 per cent. This suggests that the peak of the redshift distribution of the population of radio, 24-μm and IRAC unidentified SMGs is at $z = 2$–3.

To crudely compare the redshift distributions of the identified and unidentified SMGs, we also plot the difference between redshifts of sources in the submillimetre error circles of the identified SMGs to the field (scaled to the value in the $z = 2$–3 bin of the unidentified SMGs). We conclude that the redshift distribution of unidentified SMGs is broadly similar to that of robustly identified SMGs.

To provide a more reliable estimate of the average redshift of the unidentified SMGs, we evenly distribute the excess galaxies in the SMG error circles in each redshift bin. We verify that this method is valid by using it to calculate the average redshift for identified SMGs, which yields $z = 2.2 \pm 0.1$, in agreement with that derived using the robust counterparts alone (Section 5.1). For unidentified

SMGs, we derive an average redshift of $z = 2.5 \pm 0.2$. This suggests that unidentified SMGs may lie at marginally higher redshifts than the identified sample, although we stress that the difference is not statistically significant. This conclusion is consistent with the predicted redshift distribution of radio undetected SMGs from the semianalytic ΛCDM GALFORM model, which predicts they should lie at $z \sim 2.2$, similar to the observed SMGs (Swinbank et al. 2008).

We showed in Section 5.2 that there are nine tentative SMG counterparts with $z = 2$–3 and two with $z = 4$–5. Thus, potentially half of the excess sources in these redshift bins around the unidentified SMGs could be attributed to tentative counterparts. Indeed, if tentative SMGs are excised from this analysis, then only a $0.7\sigma$ ($4 \pm 5$) excess of $z = 2$–3 galaxies and a $1.2\sigma$ ($2.3 \pm 1.9$) excess of $z = 4$–5 galaxies around SMGs remain.

Finally, we use statistical arguments to estimate how many SMGs are still unaccounted for, and thus likely undetected in our optical and mid-IR imaging. There are 51 out of the sample of 126 LESS SMGs without robust radio, 24-μm or IRAC counterparts (Biggs et al. 2011). Due to the signal-to-noise ratio limit on the submillimetre catalogue (S/N $\geq 3.7\sigma$), five of the 126 SMGs are expected to be false detections (Weiß et al. 2009); an additional one to two are expected to have counterparts outside the search radii used (Biggs et al. 2011). This leaves 44–45 SMGs with currently unidentified counterparts that are expected to lie within our search area. We then calculate the total excess of galaxies in unidentified error circles over the field. Due to clustering, an error circle can contain more than one galaxy associated with the SMG. We then compare the sources around identified SMGs with the number of identified counterparts to determine this 'overcounting factor': $\sim 1.2\times$. We scale the difference between the field and unidentified SMG regions by this factor to estimate that there are $25 \pm 18$ LESS SMGs ($20 \pm 14$ per cent of the total) which are still unaccounted for. These have no robust radio, 24-μm and IRAC counterparts and have mid-IR fluxes below the limits of our imaging.

These counterparts could lie at $z \sim 1$–3 and be fainter than $M_H \lesssim -23$ (see Fig. 10 shown later). However, the specific SFRs (sSFRs) of such sources would be $\gtrsim 10^{-7}$ yr$^{-1}$, corresponding to lifetimes of $\lesssim 10$ Myr. The corresponding duty cycle for such short-lived sources means that to detect ∼20 sources in our 0.5-deg$^2$ survey, we require a parent population with a space density of $\gtrsim 0.02$ Mpc$^{-3}$, which we consider unlikely. Alternatively, if they have rest-frame near-IR luminosities similar to the identified SMG population, then Fig. 10 (shown later) suggests that they must lie at $z \gtrsim 3$. If correct, then we should add these sources to the SMGs identified at $z \gtrsim 3$. We have identified 11 SMGs at $z > 3$, as well as $4 \pm 2$ which have been statistically identified in our IRAC sample. To these we add the $25 \pm 18$ SMGs which are unaccounted for in our statistical analysis, to derive a total of $40 \pm 18$ SMGs ($32 \pm 14$ per cent of the whole population) at $z \geq 3$ in our survey. We conclude that ∼30 per cent, and at most ∼45 per cent, of the SMG population could reside at $z \gtrsim 3$. This corresponds to a volume density of $2.8 \times 10^{-6}$ Mpc$^{-3}$ (assuming they span the range $z = 3$–7, or 80 per cent higher if they only span $z = 3$–5). For comparison, the equivalent volume density of $z = 2$–3 SMGs, including identified counterparts and the 14 that are statistically identified in this redshift range, is $1.2 \times 10^{-5}$ Mpc$^{-3}$, signifying strong evolution in the abundance of SMGs from $z \sim 2.5$ to $z > 3$. We note that for there to be no decline in the space density of SMGs at $z > 3$, all the SMGs are required to be at $z \lesssim 3.8$. However, five of the identified SMGs have higher photometric redshifts than this, and one of those is spectroscopically confirmed at $z = 4.76$ – verifying that there is a decline in the space density of SMGs at $z > 3$.

We have statistically identified the redshifts of ∼50 per cent of the unidentified SMGs, and shown that the remainder likely lie at $z \gtrsim 3$. In the right-hand panel of Fig. 5, we combine the redshift distributions of the identified and unidentified SMGs to provide the probable redshift distribution of the *entire* $S_{870\,\mu m} \gtrsim 4$ mJy SMG population. We conclude that the most likely median redshift for the $S_{870\,\mu m} \gtrsim 4$ mJy SMG population is $z = 2.5 \pm 0.5$.

### 5.4 Simple redshift estimators for SMGs

We next consider whether the SMG population has a characteristic SED shape that can be used to predict its redshift. Previous studies have investigated and used optical (*BzK*; Daddi et al. 2004), UV (BX/BM; Steidel et al. 2004; Chapman et al. 2005) and IRAC colours (Yun et al. 2008; Hainline et al. 2009) and various combinations of radio, submillimetre and FIR flux ratios (e.g. Carilli & Yun 1999; Ivison et al. 2007; Daddi et al. 2009; Dannerbauer et al. 2010; Biggs et al. 2011) as simple estimators of the redshifts of SMGs. Here we use our 17-band photometric redshifts to investigate the reliability of such *BzK* colours and radio to submillimetre fluxes as redshift estimators and derive a simple IRAC colour indicator of redshift.

In Fig. 6, we show the *BzK* colour–colour plot (Daddi et al. 2004), which is designed to identify galaxies at $1.4 < z \lesssim 2.5$, for LESS SMG counterparts. We have distinguished between counterparts

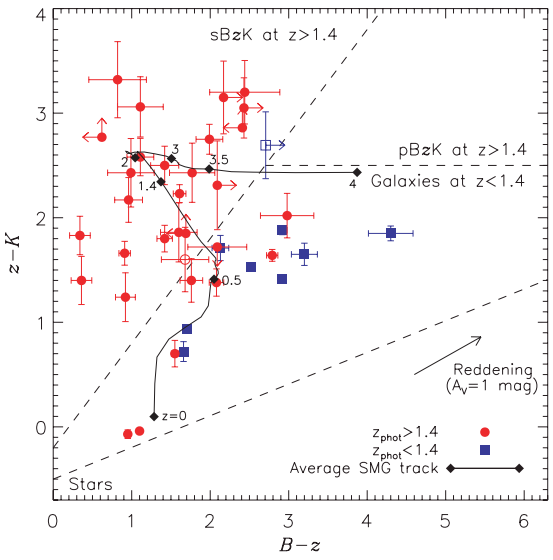


**Figure 6.** $(B - z)$ versus $(z - K)$ colour–colour plot of LESS SMG counterparts. The selection regions for star-forming and passive $z > 1.4$ *BzK* galaxies (sBzK and pBzK, respectively), $z < 1.4$ galaxies and stars (Daddi et al. 2004) are shown, and we distinguish between SMG counterparts with $z_{phot} \geq 1.4$ and $z_{phot} < 1.4$. The photometric redshifts typically agree with the *BzK* colours and most of the SMG counterparts have *BzK* colours of $z > 1.4$ star-forming galaxies and none has colours of stars or $z > 1.4$ passive galaxies (similar to the result of Bertoldi et al. 2007). All of the counterparts with sBzK colours are found to have $z_{phot} \geq 1.4$, but galaxies with BzK colours suggesting $z < 1.4$ have ∼45 per cent contamination from counterparts with $z_{phot} \geq 1.4$. We also show the redshift track of the average SMG SED (Section 5.5) from $z = 0$ to 4 and the reddening vector for $A_V = 1$ mag. The scatter in the photometry of individual SMGs compared to the redshift track of the average SMG SED suggests that the SMGs have a range of optical SEDs. The open symbols show galaxies which lie in haloes of bright stars in the $z$ band; in these cases, for the purpose of this plot only, the $z$-band magnitude is extrapolated from the SED fit and the measured $I$-band magnitude.

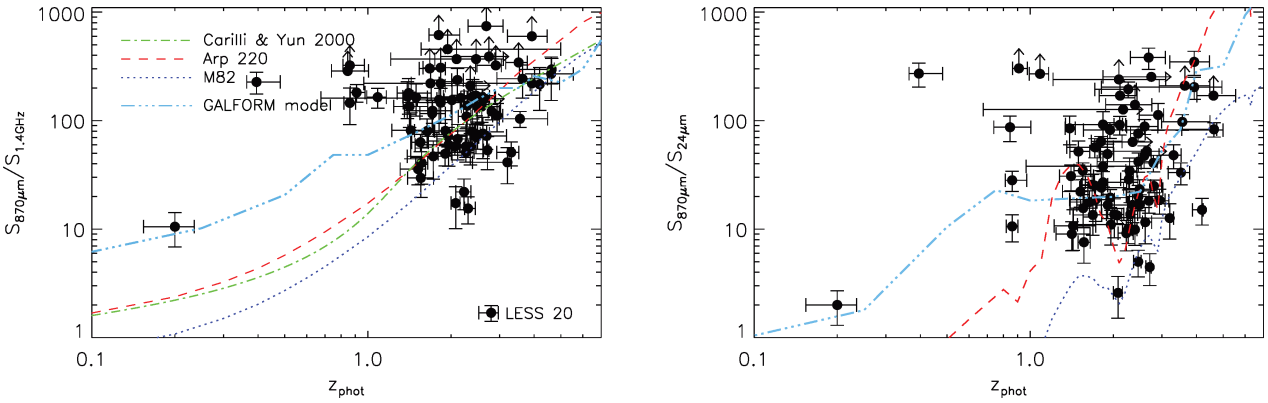


**Figure 7.** The variation in submillimetre-to-radio (left-hand panel) and submillimetre-to-mid-IR (right-hand panel) flux ratios with redshift, compared with Arp 220 and M82 (based on the SEDs of Silva et al. 1998) and SMGs in the ΛCDM GALFORM model (Baugh et al. 2005) with $S_{850\,\mu m} \geq 3$ mJy; we also show the relationship between redshift and the radio-to-submillimetre spectral index derived by Carilli & Yun (2000) in the left-hand panel. The SMGs show two orders of magnitude dispersion in both $S_{870\,\mu m}/S_{1.4\,GHz}$ and $S_{870\,\mu m}/S_{24\,\mu m}$. The model track of $S_{870\,\mu m}/S_{1.4\,GHz}$ for M82 lies below the majority of the SMGs, while that of Arp 220 more closely follows the SMGs, suggesting that they typically have a characteristic dust temperature which is cooler than that in M82 and more like that in Arp 220. Similarly, although studies have found that mid-IR spectral properties of SMGs are similar to M82 (Menéndez-Delmestre et al. 2009), we find that M82 does not describe the submillimetre-to-mid-IR continuum flux ratios well, and that Arp 220 fits better to these data. LESS 20 (labelled) is significantly brighter at 1.4 GHz than expected from its submillimetre flux and redshift and is most likely a radio-bright AGN.

with photometric redshifts above and below $z = 1.4$ and find that all the SMGs with $z_{phot} < 1.4$ lie in the expected region of colour–colour space. However, whilst SMG counterparts with $z_{phot} \geq 1.4$ typically have the colours of high-redshift star-forming galaxies, this population does scatter into the low-redshift region. Two galaxies with $z_{phot} > 1.4$, $B - z \sim 1$ and $z - K \sim -0.1$ lie near the separation between $z < 1.4$ galaxies and stars and are both X-ray luminous, bright unresolved sources which may be submillimetre-bright QSOs (see Appendix A). We conclude that the *BzK* analysis of SMG counterparts can select clean but incomplete samples of $z > 1.4$ SMGs, and that samples selected to have $z < 1.4$ will contain ∼45 per cent contamination from galaxies at higher redshift. We compare the observed *BzK* colours with a redshift track of the average SMG SED (Section 5.5) and note that the median SED of SMGs has a redder rest-frame $(U - z)$ colour [corresponding to observed $(z - K)$ at $z \sim 1.4$] than used to define the selection areas for $z > 1.4$ galaxies and that the SMGs at the highest redshifts may fall in the passive *BzK* or $z < 1.4$ region.

In Fig. 7, we plot the photometric redshift against $S_{870\,\mu m}/S_{1.4\,GHz}$ for the LESS SMGs (Weiß et al. 2009; Biggs et al. 2011), the tracks of Arp 220 and M82 (based on the SEDs of Silva et al. 1998). We also show the ΛCDM GALFORM predictions (Baugh et al. 2005) and the Carilli & Yun (2000) relationship. The wide range in $S_{870\,\mu m}/S_{1.4\,GHz}$ at a fixed redshift limits the usefulness of $S_{870\,\mu m}/S_{1.4\,GHz}$ as a redshift indicator for SMGs and indicates that SMGs have a variety of submillimetre-to-radio flux ratios, suggesting a range in dust temperatures (Chapman et al. 2005; Clements et al. 2008). Indeed, 850-μm-selected SMGs that have dust temperatures derived from that observed at multiple millimetre and submillimetre wavelengths exhibit a range of dust temperatures (e.g. Kovács et al. 2006; Coppin et al. 2008; Clements, Dunne & Eales 2010); local LIRGs and ULIRGs also have a range of dust temperatures (e.g. Dunne et al. 2000; Yang & Phillips 2007). We also note that the majority of SMGs lie above the redshift track of M82, suggesting higher submillimetre-to-radio flux ratios (potentially due to the presence of more cold dust). LESS 20 has $z_{phot} \sim 2.8$ and $S_{870\,\mu m}/S_{1.4\,GHz} \sim 1.7$, which is significantly lower than expected from its redshift, indicating that it is most likely a radio-bright AGN, so we remove it from our subsequent analyses of FIR luminosities, SFRs and characteristic dust temperature (Section 5.7).

Studies of mid-IR spectra of SMGs have shown that they are similar to M82 with an additional power-law contribution, potentially due to AGN emission or hot dust (Menéndez-Delmestre et al. 2007, 2009; Pope et al. 2008; Coppin et al. 2010b). In Fig. 7, we plot photometric redshift against $S_{870\,\mu m}/S_{24\,\mu m}$, which shows that the mid-IR-to-submillimetre flux ratios of SMGs are similar to Arp 220 and those derived in the ΛCDM GALFORM model, but are poorly represented by M82. This suggests that although SMGs have mid-IR spectra similar to M82, the mid-IR continuum emission is fainter compared to the FIR emission and is more comparable to that of Arp 220. We note that although $S_{870\,\mu m}/S_{24\,\mu m}$ for SMGs varies with redshift in a manner comparable to Arp 220, the scatter and the effect of PAH and silicate features passing through the 24-μm filter makes this measurement unsuitable for redshift derivation (Pope et al. 2006).

We expand on the work of Yun et al. (2008) and Hainline et al. (2009), and propose a new redshift estimator for SMGs, which is based on the IRAC 8- and 3.6-μm fluxes and exhibits less scatter than the commonly employed radio-to-submillimetre flux ratio. In Fig. 8, we plot this ratio against redshift for the LESS SMGs, and using the ROBUST_LINEFIT procedure from the IDL Astronomy Library (Landsman 1993), we fit an outlier-resistant linear relationship to SMGs with $z_{phot} < 4$, which yields

$$z = (2.1 \pm 0.1) + (1.9 \pm 0.2) \log_{10}\left(\frac{S_8}{S_{3.6}}\right). \quad (1)$$

We exclude SMGs with $z_{phot} \geq 4$ from the fit because at high redshifts the 1.6-μm stellar peak passes through the 8-μm filter, making this redshift estimator unreliable. For SMGs with $z < 4$, the $1\sigma$ dispersion in redshift estimated using equation (1) is $\sigma_z = 0.44$ and we find that ∼85 per cent of SMGs at $z > 2$ have $S_8/S_{3.6} > 1$. However, we find that for SMGs with strong AGN contamination (Hainline et al. 2009, 2011), equation (1) is *not* a good redshift discriminator and should be used with caution.

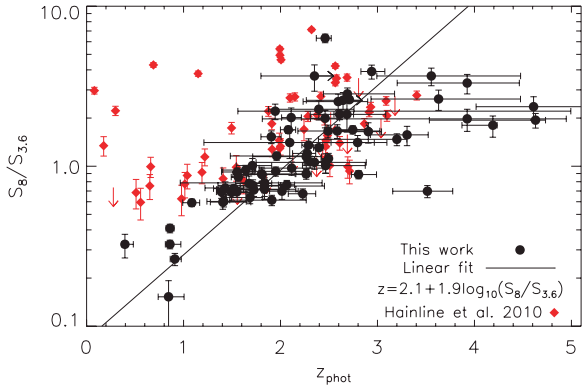


**Figure 8.** The correlation between redshift and the ratio of 8-μm to 3.6-μm flux for the LESS SMGs with photometric redshifts and those with spectroscopic redshifts (Chapman et al. 2005) and photometry from Hainline et al. (2011). The LESS SMGs show a trend and so we plot a linear fit to the SMGs with $z < 4$, which yields $z = 2.1 + 1.9\log_{10}(S_8/S_{3.6})$, with a $1\sigma$ dispersion in redshift of $\sigma_z = 0.44$. This relation may be useful as a crude redshift indicator for SMGs as we note that ∼90 per cent of all LESS SMGs with $z > 2$ have $S_8/S_{3.6} > 1$, while similarly ∼85 per cent of all LESS SMGs with $z < 2$ have $S_8/S_{3.6} < 1$. However, the SMGs from Hainline et al. (2011), which contain a large fraction of AGN contamination, do not conform to the trend, and therefore we caution against the use of $S_8/S_{3.6}$ as a redshift indicator for SMGs which are likely to contain strong AGN contamination.

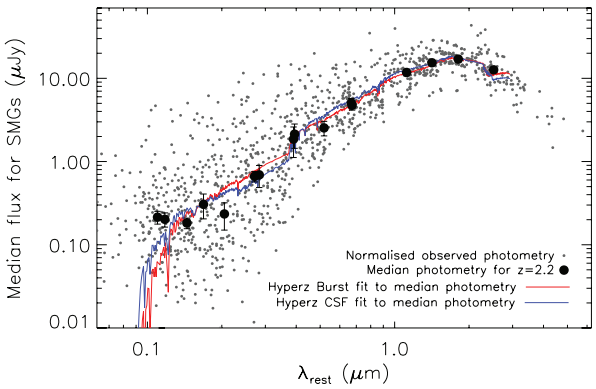


**Figure 9.** The photometry of SMG counterparts shifted to the rest frame and normalized to the $H$ band (1.6 μm). Redshifting these data to $z = 2.2$, we calculate the apparent fluxes in the 17 photometric filters considered throughout this paper and use HYPERZ to fit galaxy templates at this redshift. The median photometric points are shown and the resulting best HYPERZ Burst and CSF template fits are displayed. The best-fitting HYPERZ templates have: Burst, $A_V = 1.7$, an age of 33 Myr and a $L_H/M^* \sim 24$; CSF, $A_V = 1.1$, an age of 3.5 Gyr and a $L_H/M^* \sim 6$. It is clear that it is not possible to distinguish between these two very different star formation histories and hence there is a factor of ∼5 uncertainty in the resulting masses. The MUSYC $U38$ filter has ≥50 per cent contribution from limiting magnitudes and is excluded from the fit.

### 5.5 Typical SMG SEDs

To investigate the SED of a typical SMG, we show in Fig. 9 the SMG photometry in the rest frame and normalized in the $H$ band. We also calculate the expected fluxes expected in each of the 17 photometric filters used throughout this paper as observed at $z = 2.2$ and determine the median flux in each.

We begin by noting that the data show evidence for a break at ∼3500–4000 Å suggestive of a Balmer or 4000-Å break. Closer inspection hints at it being a Balmer break indicating that the blue rest-frame light is dominated by stars older than 20 Myr and younger than ∼2 Gyr. Then, as in Section 4.1, we use HYPERZ to fit this photometry, with redshift fixed at $z = 2.2$, and show the best-fitting templates for both the Burst and CSF star formation histories in Fig. 9. Comparing the $\chi^2$ for these two models in the same manner as in Section 4.4, we find that we cannot accurately distinguish between different star formation histories (and hence ages or light-to-mass ratios). The best-fitting Burst model has an age of just 33 Myr, an $A_V = 1.7$ and a resulting light-to-mass ratio of $L_H/M^* \sim 24$; in contrast, the CSF template yields an age of 3.5 Gyr, $A_V = 1.1$ and an $L_H/M^* \sim 6$. The reddening derived from these two template fits is in agreement with the median of the individual SED fits ($A_V = 1.5 \pm 0.1$; Section 4.4), while $L_H/M^*$ has a range of 4×.

We also estimate the extinction in LESS SMGs by comparing the SFR derived from the rest-frame far-UV luminosity (median $\mathrm{SFR_{UV}} = 2\,\mathrm{M_\odot\ yr^{-1}}$; Kennicutt 1998) with the SFR derived from the FIR luminosity (median $\mathrm{SFR_{FIR}} = 1400\,\mathrm{M_\odot\ yr^{-1}}$; Section 5.7). Comparing the two values yields $A_V = 2.6 \pm 0.2$, corresponding to reddening approximately four times higher than the SED fit and indicating that the majority of the star formation within SMGs occurs in totally obscured regions. As discussed in Kennicutt (1998), the conversion from far-UV luminosity to $\mathrm{SFR_{UV}}$ assumes that the SFR has been constant for $>10^8$ yr. SMGs are likely to be shorter bursts of activity and therefore for a fixed SFR they will be brighter at UV wavelengths and likely have higher $A_V$ than estimated above.

### 5.6 Stellar masses

We use HYPERZ to estimate the rest-frame $H$-band absolute magnitudes ($M_H$) from our SED fits and find the median $M_H = -24.1 \pm 0.1$, with $\sigma = 0.9$. In Fig. 10, we plot $M_H$ against photometric redshift for the LESS SMG counterparts. There is the suggestion of a weak trend of $M_H$ with redshift. However, as the plotted detection limit shows, this is most likely a selection effect, with the higher redshift galaxies needing to be more luminous to be detected. The average $z = 2$–3 SMG has $M_H = -24.4$ and would be detected in our survey out to $z \sim 3$–4, and therefore, any incompleteness in our SMG sample due to the IRAC flux limits is only significant at $z \gtrsim 3$.

$M_H$ is used to estimate the stellar mass of galaxies because it is less influenced by young stars than optical bands and is relatively unaffected by dust. As discussed in Section 4.4, the uncertainties in the derived spectral types and ages result in an estimated factor of ∼5 uncertainty in assumed mass-to-light ratios and thus stellar masses derived from $M_H$. Therefore, we only consider the stellar masses of the LESS SMGs statistically.

Hainline et al. (2011) estimated $H$-band mass-to-light ratios for SMGs with Burst and CSF templates, based on a Chabrier (2003) IMF. We use the average of their values converted to a Salpeter IMF (with a lower mass limit of $0.1\,\mathrm{M_\odot}$ and an upper mass cut-off of $100\,\mathrm{M_\odot}$) for our stellar mass calculation: $L_H/M^* = 3.8\,\mathrm{L_\odot\,M_\odot^{-1}}$. We adopt a Salpeter IMF as this has been shown to provide a better fit to the stellar masses of elliptical galaxies (Auger et al. 2010; Treu et al. 2010), while a Chabrier IMF leads to underestimated stellar masses. We estimate that the median stellar mass of the SMGs in our sample is $M^* = (9.1 \pm 0.9) \times 10^{10}\,\mathrm{M_\odot}$ and the standard deviation is $1.0 \times 10^{11}\,\mathrm{M_\odot}$. The quoted errors do not include the systematic uncertainty from the star formation histories and mass-to-light ratios, which adds a factor of ∼5 uncertainty to the values (Section 4.4; Fig. 9). We also caution that the choice of IMF coupled with the assumption that all the light is from the current burst can affect the derived stellar masses by an additional factor of ∼2. Finally, we note that on average we observe the SMGs

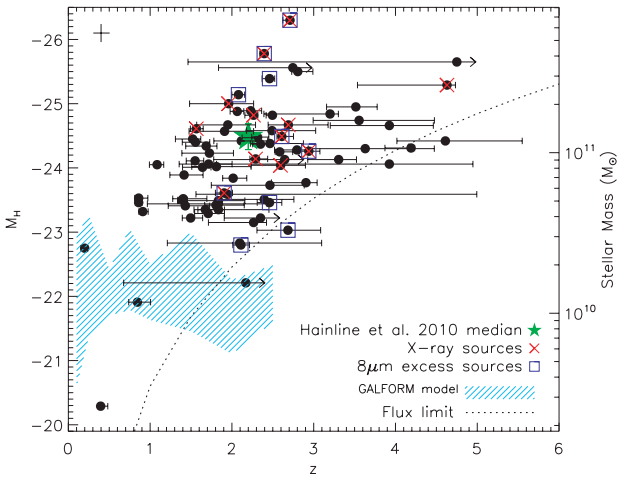


**Figure 10.** A plot of photometric redshift against rest-frame $H$-band absolute magnitude for LESS SMGs, and the approximate correspondence with the stellar mass (as described in the text). The median $M_H$ is $-24.1 \pm 0.1$ with $\sigma = 0.9$ in good agreement with the median $M_H$ from Hainline et al. (2011). This corresponds to a median stellar mass of $\sim 9.1 \times 10^{10}\,\mathrm{M}_\odot$, with $\sigma = 10 \times 10^{10}\,\mathrm{M}_\odot$, although we stress that there is a systematic error on these values of $\sim 5\times$. We also highlight SMGs with evidence for AGN activity from X-ray detections or 8-μm excesses, which appear brighter than the average SMG. We also show the predicted $1\sigma$ distribution of absolute $H$-band magnitudes of SMGs with $S_{850\,\mu\mathrm{m}} \geq 3$ mJy that are brighter than our flux limit at 4.5 μm (approximately the rest-frame $H$ band at $z = 2$) from GALFORM (Baugh et al. 2005; Lacey et al. 2008; Swinbank et al. 2008) and note that $M_H$ is underpredicted in the model. Errors in $M_H$ are dominated by the error in the photometric redshift; we calculate the error in $M_H$ for SMGs with the median redshift error by re-running HYPERZ with the redshift forced to the extremes of the error range; the corresponding errors are shown in the top left-hand corner of the plot and can be scaled with the error in redshift. The dotted line illustrates the trend in $M_H$ with redshift resulting from the flux-limited nature of our survey.

approximately halfway through the burst, and typical SMG gas masses (Greve et al. 2005) suggest an additional $\sim 3 \times 10^{10}\,\mathrm{M}_\odot$ could be added by the end of the burst.

We find that galaxies with evidence for AGN activity from an 8-μm excess or X-ray emission have median $M_H = -24.6 \pm 0.3$, compared to $M_H = -24.1 \pm 0.1$ for the remainder of the SMGs. The two SMGs with the brightest $M_H$ are the two submillimetre bright QSOs (LESS 66 and LESS 96; Appendix A) in which the observed emission is expected to be dominated by the AGN rather than starlight (Hainline et al. 2011). If these are excluded, then the median $M_H$ of SMGs containing AGNs is $M_H = -24.5 \pm 0.3$.

The median stellar mass for SMGs in the SHADES Lockman Hole was claimed to be $M^* = (6.3^{+1.6}_{-1.3}) \times 10^{11}\,\mathrm{M}_\odot$ by Dye et al. (2008). This is a factor of $\sim 7$ higher than our estimate for LESS SMGs. Dye et al. (2008) use nine-band photometry for their photometric redshift determination and claim to also be able to disentangle the star formation histories of the SMGs with sufficient accuracy to identify a significant mass of old stars which underlies the current burst. This leads to a higher effective mass-to-light ratio and correspondingly higher stellar masses. In contrast, as discussed earlier (Section 4.4), we do not believe that with existing data it is possible to untangle the influences of the potentially complex star formation histories and dust distributions on the SEDs of SMGs. Hence, we do not believe that there is any observational evidence for significant old stellar populations in these galaxies, as required by the Dye et al. (2008) results. Hainline et al. (2011) have used optical and IRAC photometric data to calculate an average stellar mass for the Chapman et al. (2005) SMGs and they find $M^* = (1.4 \pm 0.3) \times 10^{11}\,\mathrm{M}_\odot$ (converted to Salpeter IMF), comparable to our survey and a factor of $\sim 5$ lower than Dye et al. (2008).

In Fig. 10, we also show the absolute $H$-band magnitudes of SMGs in the ΛCDM GALFORM model (Baugh et al. 2005), which assumes a top-heavy IMF with slope $x = 0$. We consider only galaxies with $S_{850\,\mu\mathrm{m}} \geq 3$ mJy and fluxes in the IRAC 4.5-μm filter brighter than our detection limit (4.5 μm corresponds to the rest-frame $H$ band at $z \sim 2$). Swinbank et al. (2008) showed that GALFORM predicts rest-frame $K$-band luminosities of SMGs which are a factor of 10 lower than observed. This arises primarily due to an order of magnitude lower stellar masses than implied by observations for SMGs (see also Lacey et al. 2010). As Fig. 10 shows, the predicted rest-frame $H$-band magnitudes of the model SMGs are also a factor of 10 lower than our observations. Indeed, if SMGs formed stars following the prescriptions used in Baugh et al. (2005), then few of the SMGs above a redshift of $z \sim 2$ would have been detected in these IRAC images.

### 5.7 Dust temperatures, FIR luminosities and star formation

In order to further investigate the intrinsic properties of the LESS SMGs, we next use our photometric redshifts and the observed radio and submillimetre fluxes to derive the characteristic dust temperatures ($T_\mathrm{D}$), FIR luminosities (8–1000 μm; $L_\mathrm{FIR}$) and SFRs.

Blain et al. (2002) showed that the submillimetre-to-radio flux ratio in SMGs is mainly influenced by redshift and the characteristic dust temperature. Chapman et al. (2005) assumed a dust emissivity, $\beta = 1.5$, and the $z = 0$ FIR–radio correlation, to determine empirically that for their sample of SMGs

$$T_\mathrm{D} = \frac{6.25(1+z)}{(S_{850\,\mu\mathrm{m}}/S_{1.4\,\mathrm{GHz}})^{0.26}}. \quad (2)$$

We note that the most reliable method of calculating $T_\mathrm{D}$ is to fit template SEDs to multiple FIR and submillimetre photometric points, but for simplicity and due to the absence of published deep FIR photometry, we use equation (2) to calculate $T_\mathrm{D}$ of LESS SMGs (although we next use shallow FIR observations to confirm the validity of this assumption).

We also use the IR–radio correlation (Helou, Soifer & Rowan-Robinson 1985; Condon 1992),

$$q_\mathrm{FIR} = \log_{10}\left(\frac{L_\mathrm{FIR}}{3.75 \times 10^{12}\,\mathrm{W}}\right) - \log_{10}\left(\frac{L_{1.4\,\mathrm{GHz}}}{\mathrm{W\,Hz^{-1}}}\right), \quad (3)$$

with radio spectral index $\alpha = 0.8$ (where $S_\nu \propto \nu^{-\alpha}$) and $q_\mathrm{FIR} = 2.64$ (Bell 2003, for star-forming galaxies), to calculate FIR luminosities of the LESS SMGs from their radio fluxes, as done by Chapman et al. (2005). Although this approach was recently verified by Magnelli et al. (2010) who used *Herschel* data to show that the local FIR–radio correlation is consistent with SMGs, we caution that there may be a factor of $\sim 2$ uncertainty in the derived luminosities due to possible evolution in the FIR–radio correlation (Kovács et al. 2006, 2010; Ivison et al. 2010a) and hence the appropriate value of $q_\mathrm{FIR}$.

In Fig. 11, we plot the FIR luminosity against $T_\mathrm{D}$ for the LESS SMGs and optically faint radio galaxies (OFRGs; Chapman et al. 2004a; Casey et al. 2009; Magnelli et al. 2010). The LESS SMGs have a median $T_\mathrm{D} = 37.4 \pm 1.4$ K, with $\sigma = 14.7$ K and $L_\mathrm{FIR} = (8.2 \pm 0.9) \times 10^{12}\,\mathrm{L}_\odot$, with a standard deviation of $9.2 \times 10^{12}\,\mathrm{L}_\odot$, comparable to previous surveys (e.g. Chapman et al. 2005; Magnelli et al. 2010).

To check this result, we also employ the 250-, 350- and 500-μm *BLAST* maps of the ECDF-S (Devlin et al. 2009). We can stack

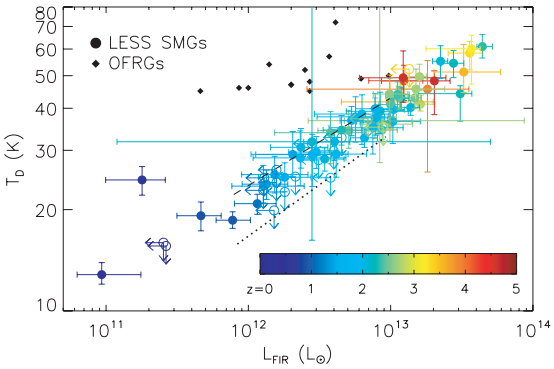


**Figure 11.** The characteristic dust temperature ($T_{\rm D}$) versus FIR luminosity ($L_{\rm FIR}$) for our SMGs. The SMGs are colour-coded on the basis of their photometric redshifts and as expected the most luminous galaxies are the hottest and also tend to be those at the highest redshifts. This trend is driven in part by the radio luminosities of the SMGs (which lack the positive $K$-correction of the submillimetre waveband); hence, this is why there is a correlation between $L_{\rm FIR}$ and $z$, but not between $S_{870\,\mu{\rm m}}$ and $z$ (Fig. 3). The regions above the dashed line and below the dotted line are illustrative of the regions excluded by our submillimetre and radio detection limits, respectively. The dashed line, which roughly demarcates the upper envelope of the data, represents the derived temperature of galaxies at $z = 2$ with various radio fluxes and $S_{870\,\mu{\rm m}} = 4.2$ mJy. The dotted line, which similarly demarcates the lower envelope, is derived for submillimetre-luminous ($S_{870\,\mu{\rm m}} = 16$ mJy) sources with radio flux equal to our detection limit ($3\sigma = 19.5$ μJy) at redshifts of $z = 1.4$–4. This reflects both the strong cut-off in the submillimetre luminosity function at high luminosities and the fact that our radio data are only just deep enough to detect counterparts to the majority of SMGs. We conclude that the apparent correlation between $T_{\rm D}$ and $L_{\rm FIR}$ is in part caused by selection bias. We note that the OFRGs (Chapman et al. 2004a; Casey et al. 2009; Magnelli et al. 2010), which are detected in the radio but not in the submillimetre, lie above the upper dashed line.

the emission in these maps at the positions of the LESS SMG counterparts and fit the stacked fluxes with a modified blackbody with $\beta = 1.5$ at $z = 2.2$ and correct the luminosity of the fitted blackbody to the *total* IR luminosity, 8–1000 μm, based on Ivison et al. (2010c). From this calculation, the typical characteristic dust temperature of the LESS SMGs is $T_{\rm D} = 33.6 \pm 1.1$, and the typical FIR luminosity is $L_{\rm FIR} = (7.6^{+1.7}_{-1.5}) \times 10^{12}\,{\rm L}_{\odot}$. These values are in reasonable agreement with those derived above from the local FIR–radio correlation.

We find that the highest redshift galaxies also have the highest luminosities due to a combination of the radio $K$-correction (preventing the detection of low-luminosity galaxies at high redshifts) and luminosity evolution (see Fig. 12). There is an apparent trend between $T_{\rm D}$ and $L_{\rm FIR}$ but this is likely at least partially a selection effect, although local *IRAS* galaxies also exhibit a tight correlation between $T_{\rm D}$ and $L_{\rm IR}$ (Chapman et al. 2003b; Chapin et al. 2009). We note that 850-μm-selected galaxies that have $T_{\rm D}$ and $L_{\rm FIR}$ estimates based on multiwavelength (sub-)millimetre data (e.g. Kovács et al. 2006; Coppin et al. 2008; Clements et al. 2010) typically have $T_{\rm D}$ and $L_{\rm FIR}$ values in the ranges of those derived here for LESS SMGs. This suggests that our use of equations (2) and (3) does not significantly bias the results of Fig. 11. To illustrate the selection effects, we also show in Fig. 11 OFRGs (Chapman et al. 2004a), which are detected at radio but not submillimetre wavelengths and have radio luminosities similar to SMGs, but contain warmer dust ($T_{\rm D} \sim 45$ K; Casey et al. 2009; Magnelli et al. 2010). Our 870-μm detection limit misses warmer and lower luminosity galaxies from the sample and the radio detection limit excludes the colder luminous galaxies (e.g. Chapman et al. 2005).

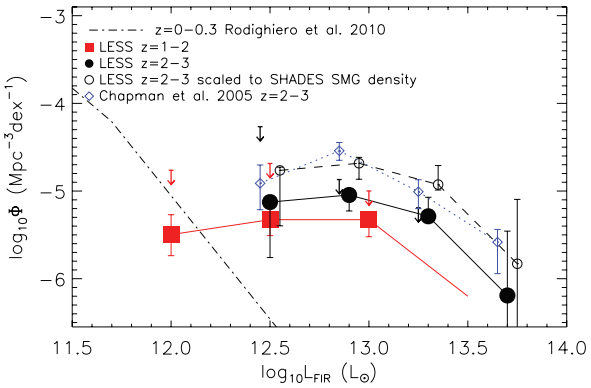


**Figure 12.** FIR luminosity functions of the radio-detected LESS SMGs with $z = 1$–2 and 2–3. Evolution is evident in the luminosity function of the LESS SMGs between the two redshift bins, and from the 24-μm-selected low-redshift comparison sample (Rodighiero et al. 2010). The SMGs have higher luminosities than the $z < 0.3$ 24-μm galaxies, and the $z = 2$–3 SMGs having higher luminosities and $\Phi^*$. We also show the $z = 2$–3 luminosity function of Chapman et al. (2005) SMGs (offset slightly in $\log_{10}L_{\rm FIR}$ for clarity) for comparison. The LESS $z = 2$–3 sample has a systematically lower luminosity density than Chapman et al. (2005) SMGs in the same redshift range. Weiß et al. (2009) showed that the ECDF-S is underdense at submillimetre wavelengths and by scaling the LESS luminosity function such that the SMG number density matches that of the SHADES (Coppin et al. 2006), we show that the disparity in $\Phi^*$ between the LESS and Chapman et al. (2005) is likely due to the relative density of SMGs in the two surveys (the scaled LESS luminosity function is offset slightly in $\log_{10}L_{\rm FIR}$ SMGs for clarity). We calculate the maximum contribution from unidentified SMGs, by assigning them the redshift distribution that we measure in Section 5.3 and radio fluxes equal to our detection limit. Including the contribution from unidentified SMGs, the total maximum $\Phi$ in each luminosity bin is represented by an arrow (offset slightly in $\log_{10}L_{\rm FIR}$ for $z = 2$–3 SMGs for clarity).

**Table 4.** FIR luminosity function for radio-detected LESS SMGs.

| $z = 1$–2 SMGs | | $z = 2$–3 SMGs | |
|---|---|---|---|
| $\log_{10}L_{\rm FIR}$ ($L_{\odot}$) | $\log_{10}\Phi$ (Mpc$^{-3}$ dex$^{-1}$) | $\log_{10}L_{\rm FIR}$ ($L_{\odot}$) | $\log_{10}\Phi$ (Mpc$^{-3}$ dex$^{-1}$) |
| 12.0 | $-5.5 \pm 0.2$ | 12.5 | $-5.1^{+0.1}_{-0.6}$ |
| 12.5 | $-5.3 \pm 0.1$ | 12.9 | $-5.0^{+0.1}_{-0.2}$ |
| 13.0 | $-5.3^{+0.1}_{-0.2}$ | 13.3 | $-5.3^{+0.2}_{-0.1}$ |
| 13.5 | $<-6.2$ | 13.7 | $-6.2^{+0.7}_{-6.2}$ |

In Fig. 12 and Table 4, we present the FIR luminosity functions of the radio-detected LESS SMGs with $z = 1$–2 and 2–3, compared to the $z = 2$–3 result from Chapman et al. (2005). We calculate the LESS SMG luminosity function with an accessible volume technique where

$$\Phi(L)\Delta L = \sum_i \frac{1}{V_i}, \qquad (4)$$

which accounts for the flux-limited nature of our survey. $\Phi(L)\Delta L$ is the number density of sources with luminosities between $L$ and $L + \Delta L$, and $V_i$ is the comoving volume within which the $i$th source can be detected in the luminosity bin under consideration. Since we derive the FIR luminosity from the radio flux, $V_i$ is calculated using the radio luminosity. Error bars are calculated by bootstrapping and account for the redshift, luminosity and binning errors. We use the same method to calculate the luminosity function for Chapman

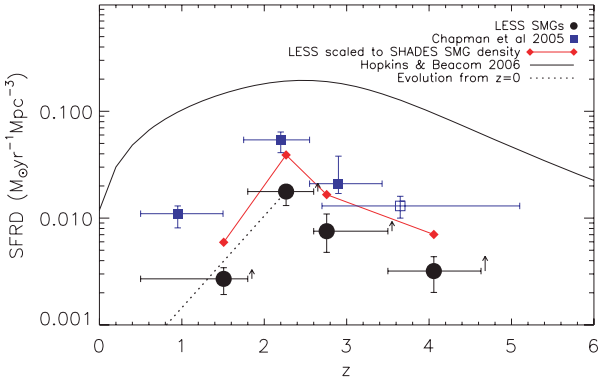


**Figure 13.** Evolution of the SFRD for the radio-detected LESS SMGs compared to Chapman et al. (2005). The arrows to the right-hand side of each LESS redshift bin indicate the maximum additional contribution from unidentified SMGs and the open symbol represents unidentified SMGs from Chapman et al. (2005). We also show the modified Salpeter A IMF fit to the SFRD compilation from Hopkins & Beacom (2006) and a line showing the evolution from *IRAS* ULIRGs at $z = 0$ (Elbaz & Cesarsky 2003) to LESS SMGs at $z = 2.3$. The LESS SMG activity peaks at $z \sim 2$ – similar to that found by previous studies of star-forming galaxies and the peak activity of QSOs (Hopkins, Richards & Hernquist 2007). The contribution from SMGs to the total SFRD also peaks at $z \sim 2$ where they are responsible for ∼10 per cent of the Hopkins & Beacom (2006) SFRD. The ECDF-S is underdense at submillimetre wavelengths (Weiß et al. 2009), so similarly to Fig. 12 we also scale the SFRD of the LESS SMGs such that the number counts match the SHADES, allowing a closer comparison to Chapman et al. (2005).

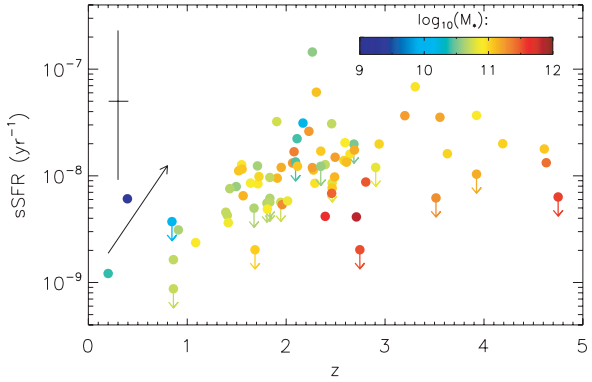


**Figure 14.** A plot of sSFR versus redshift for the LESS SMGs. Galaxies are colour-coded by mass and we show the median error bar in the top left-hand hand corner and note that similarly to Fig. 10 the error in the sSFR is correlated with that in redshift. The arrow represents the gradient of the trend in the sSFR with redshift for IRAC-selected galaxies with $\log_{10}(M_*) = 10.3$–$10.8\,\mathrm{M}_\odot$, offset in the sSFR by two orders of magnitude for the purpose of display. We note that due to the requirement for radio counterparts no SMGs are detected in the high-redshift and low-sSFR region of this plot. Similarly, the short lifetime of SMGs with sSFR $\gtrsim 10^{-7}\,\mathrm{yr}^{-1}$ and the limited volume of our survey mean that few SMGs with very high sSFRs are detected. However, the dearth of SMGs at $z \lesssim 1.5$ with sSFR $\gtrsim 10^{-8}\,\mathrm{yr}^{-1}$ may indicate an upper limit to the sSFR of SMGs with a similar scaling to the trends seen in lower activity galaxies at lower redshifts (Damen et al. 2009).

et al. (2005) SMGs based on the redshifts and radio fluxes listed in that paper. By assuming that unidentified SMGs have radio fluxes equal to our detection limit and the redshift distribution that we measure in Section 5.3, we also calculate the maximum contribution of unidentified SMGs to the FIR luminosity functions.

We observe strong evolution in the FIR luminosity function: the $z = 2$–3 SMGs are more luminous and have higher space densities than the $z = 1$–2 SMGs, which in turn are more luminous than the $z < 0.3$ 24-μm-selected galaxies from Rodighiero et al. (2010) (see also the *Herschel* sample of Vaccari et al. 2010). LESS SMGs at $z = 2$–3 have $\Phi^* \sim 60$ per cent and $L^*$ approximately two times larger than those at $z = 1$–2.

The $z = 2$–3 LESS SMGs have systematically lower $\Phi^*$ than the Chapman et al. (2005) SMGs in the same redshift range. This may be due to cosmic variance since Weiß et al. (2009) showed that the ECDF-S is a factor of ∼2 underdense compared to other large submillimetre surveys at flux densities $\gtrsim$3 mJy. By rescaling the LESS luminosity function so that the 870-μm number counts agree with those of the SHADES (Coppin et al. 2006), which should be similar to that of Chapman et al. (2005) since both covered multiple fields, Fig. 12 shows that the low surface density of SMGs in the ECDF-S is most likely the cause of the disparity in $\Phi^*$.

In Fig. 13, we show the evolution of the SFR density (SFRD) of the radio-detected LESS SMGs. We use the same accessible volume technique as in our luminosity function calculations to account for the flux-limited nature of the survey. Error bars are calculated from bootstrapping and include the uncertainties in binning, redshifts and SFRs. Since the SFRs are based upon radio fluxes, we exclude the suspected radio-bright AGN LESS 20 from this analysis.

We do not know the individual redshifts, IR luminosities or SFRs for 45 per cent of the LESS SMGs because they do not have robustly identified optical counterparts. In Fig. 13, we account for this population by assigning them the redshift distribution that we measure in Section 5.3 and assuming radio fluxes equal to our detection limit. The calculated SFRD of the unidentified SMGs from this analysis is an upper limit since the actual radio fluxes will typically be lower than the detection limit. In Fig. 13, we indicate the maximum contribution to the SFRD of unidentified SMGs in each redshift bin.

The SFRDof the LESS SMGs appears to peak at $z \sim 2$, similar to Chapman et al. (2005). The LESS SMGs have a lower SFRD than the SMGs from Chapman et al. (2005) but we note that the lower number density of SMGs in the ECDF-S is sufficient to account for this effect. This corresponds to the peak of QSO activity at $z = 2.15 \pm 0.05$ (Hopkins et al. 2007). The fractional contribution of LESS SMGs to the SFRD of the Universe also peaks at $z \sim 2$ where they are responsible for ∼10 per cent of the SFRD as estimated by Hopkins & Beacom (2006) from a compilation of surveys that does not include any submillimetre surveys. We stress that this only includes SMGs with $S_{870\,\mu\mathrm{m}} \gtrsim 4$ mJy. Assuming that fainter sources have the same redshift distribution, the contribution of SMGs with $S_{870\,\mu\mathrm{m}} \gtrsim 1$ mJy is ∼100 per cent of the Hopkins et al. (2007) value. Thus, SMGs contribute ∼50 per cent of the *total* SFRD of the Universe at $z \sim 2$. The contribution of the integrated flux from the LESS SMGs to the cosmic IR background is presented in Weiß et al. (2009).

We use Kennicutt (1998), which assumes a Salpeter IMF with upper and lower mass limits of 0.1 and $100\,\mathrm{M}_\odot$, respectively, to calculate the SFRs of the LESS SMGs from their inferred FIR luminosities. The median SFR is $1400 \pm 200\,\mathrm{M}_\odot\,\mathrm{yr}^{-1}$, with $\sigma = 1100\,\mathrm{M}_\odot\,\mathrm{yr}^{-1}$. The median sSFR = SFR/$M^*$ = $(1.2 \pm 0.1) \times 10^{-8}\,\mathrm{yr}^{-1}$, with $\sigma = 1.9 \times 10^{-8}\,\mathrm{yr}^{-1}$. Although again, we caution that due to the uncertainties in the stellar mass estimates, there is an additional factor of ∼5 uncertainty in these values (see Section 4.4 for a full discussion). The median formation time-scale of the LESS SMGs is thus ∼100 Myr and it is feasible that all of the stellar mass we see could be formed in a burst. In Fig. 14, we plot the trend of the sSFR against the redshift of the LESS SMGs. We note that

the apparent lack of galaxies with a low sSFR at high redshifts is a selection effect due to the requirement for a radio counterpart, and that galaxies with sSFR $\gtrsim 10^{-7}$ yr$^{-1}$ are rare due the brevity of the burst phase. However, the dearth of SMGs at $z \lesssim 1.5$ with sSFR $\sim 10^{-8}$–$10^{-7}$ yr$^{-1}$ is not a selection effect and this upper envelope may be following the same trend in the sSFR with redshift seen in galaxies with similar masses but lower SFRs (e.g Damen et al. 2009).

Finally, we relate our new estimate of the redshift distribution of SMGs to constraints on the evolution of their likely descendants: massive early-type galaxies (Swinbank et al. 2006). As we have shown, the bulk of the SMG population with observed 870-μm fluxes above ∼4 mJy lie at redshifts of $z \sim 1.5$–3 with a median redshift of $z \sim 2.5$. We estimate that the volume density of SMGs at $z = 2$–3 above our flux limit is $1.3 \times 10^{-5}$ Mpc$^{-3}$, where we include both the identified and statistically identified samples in this estimate. Using a characteristic lifetime of the SMG phase of ∼100 Myr, we can correct this density for the burst duty cycle to derive a volume density for the remnants of $2 \times 10^{-4}$ Mpc$^{-3}$. As we have shown, the estimated baryonic masses of these galaxies are $\sim 1.2 \times 10^{11}$ M$_\odot$, combining our best estimate of the stellar mass with the typical gas masses from Greve et al. (2005). If the burst of star formation we are seeing in the SMG phase is the last major star formation event in these galaxies, then we expect their descendants to appear as passive, red galaxies at $z \sim 1.5$ (>1 Gyr after $z \sim 2$).

There have been various estimates of the volume density of massive, passive galaxies at $z \sim 1$–2 (McCarthy et al. 2004; Daddi et al. 2005; Taylor et al. 2009a). For galaxies with masses of $\gtrsim 10^{11}$ M$_\odot$, the estimated space densities are (1–2) $\times 10^{-4}$ Mpc$^{-3}$ (at $z = 1.5$–1.8; Taylor et al. 2009a), $3 \times 10^{-4}$ Mpc$^{-3}$ (at $\langle z \rangle = 1.7$; Daddi et al. 2005) and $0.6 \times 10^{-4}$ Mpc$^{-3}$ (at $\langle z \rangle = 1.5$; McCarthy et al. 2004). These estimates, with their various uncertainties, are comparable to the predicted volume density of massive, passive galaxies if these all undergo a SMG phase at an earlier epoch. Hence, the starbursts in SMGs may be responsible for the formation of a large fraction of the passive, massive galaxies seen at $z \sim 1.5$.

We can attempt a similar calculation comparing the SMG population at $z > 3$ with the constraints on massive galaxies at $z \gtrsim 2$. We estimate the volume density of $z > 3$ SMGs from Section 5.3 as $2.8 \times 10^{-6}$ Mpc$^{-3}$. This includes the 11 identified SMGs, $4 \pm 2$ statistically identified SMGs and the remaining $25 \pm 18$ unidentified sources and assumes that they are contained within a redshift range of $z = 3$–7. Using a characteristic lifetime of the SMG phase of ∼100 Myr, we can correct this density for the Burst duty cycle to derive a volume density for the remnants of $3.8 \times 10^{-5}$ Mpc$^{-3}$. Again the estimated baryonic masses of these galaxies are $\sim 1.2 \times 10^{11}$ M$_\odot$. Unfortunately, observable limits on the volume density of passive galaxies are increasingly uncertain at $z > 2$, but using the estimates from Coppin et al. (2009) of the volume density of massive galaxies of $\sim$(1–5) $\times 10^{-5}$ Mpc$^{-3}$, we again conclude that it is possible that the SMG population we have identified is also responsible for the formation of a significant fraction of the most massive galaxies at $z \sim 2.5$.

Thus, we conclude that the presence of a sizable population of passive galaxies at high redshift may be intimately linked to the strong evolution in dust-obscured starbursts in the distant Universe. Theoretical attempts to match the properties of high-redshift galaxies therefore need to focus on these observable constraints as aspects of the same problem (Swinbank et al. 2008).

We also estimate the fraction of local massive passive galaxies that underwent a SMG phase at $z = 1$–3, the peak epoch of SMG activity. The volume density of passive galaxies with stellar masses $>10^{11}$ M$_\odot$ at $z < 0.05$ ($z \sim 0.2$) is $\sim 6 \times 10^{-4}$ Mpc$^{-3}$ ($\sim 5 \times 10^{-4}$ Mpc$^{-3}$; Taylor et al. 2009a). The volume density of LESS SMGs with $z = 1$–3 is $1.1 \times 10^{-5}$ Mpc$^{-3}$ and accounting for a ∼100 Myr SMG lifetime, the volume density of the remnants is ∼4 $\times 10^{-4}$ Mpc$^{-3}$. We conclude that ∼65 per cent of $z < 0.05$ (∼80 per cent of $z \sim 0.5$) passive galaxies with $M^* > 10^{11}$ M$_\odot$ likely underwent a SMG phase at $z = 1$–3.

## 6 SUMMARY AND CONCLUSIONS

We use deep multicolour imaging of the ECDF-S in 17 bands to derive the photometric properties of the counterparts of SMGs in the LESS LABOCA survey of the ECDF-S (Weiß et al. 2009; Biggs et al. 2011). Our main results are as follows:

(i) LESS radio, 24-μm and IRAC-identified SMGs have a median redshift of $z = 2.2 \pm 0.1$, with a standard deviation of 0.9. Thus, the peak activity in SMGs corresponds to the epoch of maximal QSO and star formation activity in the Universe. The redshift distribution of LESS SMGs is consistent with the spectroscopic survey of Chapman et al. (2005), but higher than the photometric studies of the SHADES (Clements et al. 2008; Dye et al. 2008). We find a higher redshift tail to the distribution of LESS galaxies, with 11 (14 per cent) identified SMGs at $z \gtrsim 3$. Counterparts identified through radio, 24-μm and IRAC emission have statistically indistinguishable redshift distributions; similarly, robust and tentative counterparts have comparable redshift distributions, albeit with some foreground contamination in the tentative sample. Previous studies provided tentative evidence that SMGs with the highest submillimetre fluxes may be the highest redshift sources (e.g. Ivison et al. 2002; Pope et al. 2005), but with our extensive photometric redshifts, we find no detectable correlation within our sample.

(ii) A statistical study of the source population in the error circles of the 51 SMGs that lack robust radio, 24-μm and IRAC counterparts suggests that there is a tentative excess of $24 \pm 12$ $z > 1$ galaxies in these regions. Of these $14 \pm 7$ are at $z = 2$–3 and $4 \pm 2$ are at $z = 4$–5; both of these excesses have a <0.2 per cent probability of being observed by chance. This excess population corresponds to the counterparts or companions of the unidentified SMGs and our analysis then suggests that the redshift distribution of these unidentified SMGs peaks at $z = 2.5 \pm 0.2$. This is similar to, but slightly higher than, that of the identified population, suggesting that many of the unidentified SMGs are at $z \sim 2$–3 and have radio or 24-μm fluxes just below our detection limits.

(iii) We estimate that there are $25 \pm 18$ ($20 \pm 14$ per cent of all the SMGs) LESS SMGs that are not robustly identified and which are not accounted for in our statistical analysis of unidentified SMGs. These should be galaxies without any detectable mid-IR emission and as a result are likely to lie at $z \gtrsim 3$. Including the identified SMGs at $z > 3$, we estimate that $32 \pm 14$ per cent of all LESS SMGs lie at $z > 3$.

(iv) We combine the redshift distribution of identified SMGs with that statistically determined for unidentified SMGs, including the SMGs which are not detected in our survey and are likely to lie at $z \gtrsim 3$. We conclude that the likely median redshift of the *entire* population of $S_{870\,\mu\mathrm{m}} \gtrsim 4$ mJy SMGs is $z = 2.5 \pm 0.5$.

(v) The median rest-frame $H$-band absolute magnitude of the LESS SMGs is $M_H = -24.1 \pm 0.1$ with $\sigma = 0.9$. Using $M_H$ and the average mass-to-light ratio from Hainline et al. (2011) (converted to a Salpeter IMF), we calculate that the median stellar mass of the LESS SMGs is $(9.1 \pm 0.9) \times 10^{10}$ M$_\odot$, with $\sigma = 1.0 \times 10^{11}$ M$_\odot$. However, a $\chi^2$ analysis of the best-fitting star formation histories

shows that, even with 17-band photometry spanning the UV to mid-IR, we cannot reliably distinguish different star formation histories and ages for the SMGs. We estimate that this results in an additional factor of ∼5 uncertainty in the mass-to-light ratios and hence the derived stellar masses.

(vi) Using our photometric redshifts, submillimetre and radio fluxes, we calculate that the median characteristic dust temperature of the SMGs is $T_{\rm D} = 37.4 \pm 1.4$ K, with $\sigma = 14.7$ K. The median FIR luminosity of the SMGs, derived from the radio luminosity, is $L_{\rm FIR} = (8.2 \pm 0.9) \times 10^{12}\,{\rm L}_{\odot}$, with $\sigma = 9.2 \times 10^{12}\,{\rm L}_{\odot}$. For a Salpeter IMF, this corresponds to the median ${\rm SFR} = 1400\,{\rm M}_{\odot}\,{\rm yr}^{-1}$, with $\sigma = 1100\,{\rm M}_{\odot}\,{\rm yr}^{-1}$. We show that, for LESS SMGs, the apparent correlation between the FIR luminosity and $T_{\rm D}$ is in part a selection effect.

(vii) The FIR luminosity function of the LESS SMGs exhibits a strong redshift evolution, such that SMGs at $z = 2$–3 are more numerous and have higher luminosities than those at $z = 1$–2. We find that the normalization of the luminosity function is lower for the LESS than for the Chapman et al. (2005) SMG sample, and by scaling the ECDF-S submillimetre number counts we show that this is due to the underdensity of the ECDF-S at submillimetre wavelengths (Weiß et al. 2009).

(viii) The SFRD and fractional contribution to the global SFRD of the LESS SMGs with $S_{870\,\mu{\rm m}} \gtrsim 4$ mJy evolves with redshift and both peak at $z \sim 2$, where the LESS population contributes a total SFR density of $0.02\,{\rm M}_{\odot}\,{\rm yr}^{-1}\,{\rm Mpc}^{-1}$. If fainter submillimetre sources have the same redshift distribution, then SMGs with $S_{870\,\mu{\rm m}} > 1$ mJy produce ∼50 per cent of the SFRD of the Universe at $z \sim 2$.

(ix) The masses and the volume density of LESS SMGs at $z = 2$–3 are comparable to those of massive, passive galaxies at $z \sim 1$–2, and similarly the volume density of $z > 3$ SMGs is comparable to the limits on the numbers of massive galaxies at $z \sim 2$–3. This suggests that a large fraction of the population of massive, passive galaxies at high redshifts form most of their stars during an earlier SMG phase.

This analysis demonstrates the strengths and weaknesses of the photometric redshift analysis for SMGs in a field with excellent photometry. In the impending era of the SCUBA-2 and *Herschel* $\gg 10^5$ SMGs will be discovered; it will be impossible to obtain spectroscopic redshifts for such large samples and hence the challenge is to obtain sufficient photometric coverage of these survey fields to allow a photometric analysis of the type described here.

## ACKNOWLEDGMENTS

We thank an anonymous referee for helpful comments that improved this paper. We also thank Carlton Baugh, Mark Dickinson and Laura Hainline for help and useful discussions. JLW acknowledges the support of a Science and Technology Facilities Council (STFC) studentship, IS acknowledges the support of the STFC, and KEKC and AMS acknowledge the support of STFC fellowships. WNB, BL and YQX acknowledge Chandra X-ray Observatory grant SP8-9003A and NASA ADP grant NNX10AC99G. JSD acknowledges the support of the Royal Society through a Wolfson Research Merit award and the support of the European Research Council through the award of an Advanced Grant. This publication is based on data acquired with the APEX under programme numbers 078.F-9028(A), 079.F-9500(A), 080.A-3023(A) and 081.F-9500(A). The APEX is a collaboration between the Max-Planck-Institut fur Radioastronomie, the European Southern Observatory and the Onsala Space Observatory. This study is based on observations made with ESO telescopes at the Paranal and La Silla Observatories under programme numbers 171.A-3045, 168.A-0485, 082.A-0890 and 183.A-0666.

## REFERENCES

Alexander D. M., Bauer F. E., Chapman S. C., Smail I., Blain A. W., Brandt W. N., Ivison R. J., 2005, ApJ, 632, 736
Aretxaga I. et al., 2007, MNRAS, 379, 1571
Auger M. W., Treu T., Gavazzi R., Bolton A. S., Koopmans L. V. E., Marshall P. J., 2010, ApJ, 721, L163
Austermann J. E. et al., 2010, MNRAS, 401, 160
Balestra I. et al., 2010, A&A, 512, A12
Barger A. J., Cowie L. L., Sanders D. B., Fulton E., Taniguchi Y., Sato Y., Kawara K., Okuda H., 1998, Nat, 394, 248
Barger A. J., Cowie L. L., Sanders D. B., 1999, ApJ, 518, L5
Baugh C. M., Lacey C. G., Frenk C. S., Granato G. L., Silva L., Bressan A., Benson A. J., Cole S., 2005, MNRAS, 356, 1191
Bell E. F., 2003, ApJ, 586, 794
Bertin E., Arnouts S., 1996, A&AS, 117, 393
Bertoldi F. et al., 2000, A&A, 360, 92
Bertoldi F. et al., 2007, ApJS, 172, 132
Biggs A. D. et al., 2011, MNRAS, 413, 2314
Blain A. W., Longair M. S., 1993, MNRAS, 264, 509
Blain A. W., Smail I., Ivison R. J., Kneib J., 1999, MNRAS, 302, 632
Blain A. W., Smail I., Ivison R. J., Kneib J., Frayer D. T., 2002, Phys. Rep., 369, 111
Bolzonella M., Miralles J.-M., Pelló R., 2000, A&A, 363, 476
Bruzual G., 2007, in Vallenari A., Tantalo R., Portinari L., Moretti A., eds, ASP Conf. Ser. Vol. 374, From Stars to Galaxies: Building the Pieces to Build Up the Universe. Astron. Soc. Pac., San Francisco, p. 303
Bruzual A. G., Charlot S., 1993, ApJ, 405, 538
Bunker A. J., Stanway E. R., Ellis R. S., McMahon R. G., McCarthy P. J., 2003, MNRAS, 342, L47
Calzetti D., Armus L., Bohlin R. C., Kinney A. L., Koornneef J., Storchi-Bergmann T., 2000, ApJ, 533, 682
Cardamone C. N. et al., 2010, ApJS, 189, 270
Carilli C. L., Yun M. S., 1999, ApJ, 513, L13
Carilli C. L., Yun M. S., 2000, ApJ, 530, 618
Casali M. et al., 2006, in McLean I. S., Iye M., eds, SPIE Conf. Ser. Vol. 6269, Ground-based and Airborne Instrumentation for Astronomy. SPIE, Bellingham, p. 62690W
Casey C. M. et al., 2009, MNRAS, 399, 121
Chabrier G., 2003, PASP, 115, 763
Chapin E. L. et al., 2009, MNRAS, 398, 1793
Chapman S. C., Blain A. W., Ivison R. J., Smail I. R., 2003a, Nat, 422, 695
Chapman S. C., Helou G., Lewis G. F., Dale D. A., 2003b, ApJ, 588, 186
Chapman S. C., Smail I., Blain A. W., Ivison R. J., 2004a, ApJ, 614, 671
Chapman S. C., Smail I., Windhorst R., Muxlow T., Ivison R. J., 2004b, ApJ, 611, 732
Chapman S. C., Blain A. W., Smail I., Ivison R. J., 2005, ApJ, 622, 772
Clements D. L. et al., 2008, MNRAS, 387, 247
Clements D. L., Dunne L., Eales S., 2010, MNRAS, 403, 274
Condon J. J., 1992, ARA&A, 30, 575
Coppin K. et al., 2006, MNRAS, 372, 1621
Coppin K., Halpern M., Scott D., Borys C., Dunlop J., Dunne L., Ivison R., Wagg J., 2008, MNRAS, 384, 1597
Coppin K. E. K. et al., 2009, MNRAS, 395, 1905
Coppin K. et al., 2010a, MNRAS, 407, L103
Coppin K. et al., 2010b, ApJ, 713, 503
Cristiani S. et al., 2000, A&A, 359, 489
Croom S. M., Warren S. J., Glazebrook K., 2001, MNRAS, 328, 150
Daddi E., Cimatti A., Renzini A., Fontana A., Mignoli M., Pozzetti L., Tozzi P., Zamorani G., 2004, ApJ, 617, 746
Daddi E. et al., 2005, ApJ, 626, 680
Daddi E. et al., 2009, ApJ, 694, 1517

Damen M., Labbé I., Franx M., van Dokkum P. G., Taylor E. N., Gawiser E. J., 2009, ApJ, 690, 937
Damen M. et al., 2011, ApJ, 727, 1
Dannerbauer H., Lehnert M. D., Lutz D., Tacconi L., Bertoldi F., Carilli C., Genzel R., Menten K., 2002, ApJ, 573, 473
Dannerbauer H., Walter F., Morrison G., 2008, ApJ, 673, L127
Dannerbauer H. et al., 2010, ApJ, 720, L144
Devlin M. J. et al., 2009, Nat, 458, 737
Dickinson M. et al., 2004, ApJ, 600, L99
Doherty M., Bunker A. J., Ellis R. S., McCarthy P. J., 2005, MNRAS, 361, 525
Downes A. J. B., Peacock J. A., Savage A., Carrie D. R., 1986, MNRAS, 218, 31
Dunlop J. S. et al., 2010, MNRAS, 408, 2022
Dunne L., Eales S., Edmunds M., Ivison R., Alexander P., Clements D. L., 2000, MNRAS, 315, 115
Dye S. et al., 2008, MNRAS, 386, 1107
Eales S., Lilly S., Gear W., Dunne L., Bond J. R., Hammer F., Le Fèvre O., Crampton D., 1999, ApJ, 515, 518
Elbaz D., Cesarsky C. J., 2003, Sci, 300, 270
Fazio G. G. et al., 2004, ApJS, 154, 10
Feldmann R. et al., 2006, MNRAS, 372, 565
Gawiser E. et al., 2006, ApJS, 162, 1
Giacconi R. et al., 2002, ApJS, 139, 369
Giavalisco M. et al., 2004, ApJ, 600, L93
Grazian A. et al., 2006, A&A, 449, 951
Greve T. R. et al., 2005, MNRAS, 359, 1165
Güsten R., Nyman L. Å., Schilke P., Menten K., Cesarsky C., Booth R., 2006, A&A, 454, L13
Hainline L. J., Blain A. W., Smail I., Frayer D. T., Chapman S. C., Ivison R. J., Alexander D. M., 2009, ApJ, 699, 1610
Hainline L. J., Blain A. W., Smail I., Alexander D. M., Armus L., Chapman S. C., Ivison R. J., 2011, preprint (astro-ph/1006.0238)
Helou G., Soifer B. T., Rowan-Robinson M., 1985, ApJ, 298, L7
Hildebrandt H. et al., 2010, A&A, 523, A31
Hopkins A. M., Beacom J. F., 2006, ApJ, 651, 142
Hopkins P. F., Richards G. T., Hernquist L., 2007, ApJ, 654, 731
Hughes D. H. et al., 1998, Nat, 394, 241
Ivison R. J., Smail I., Le Borgne J., Blain A. W., Kneib J., Bezecourt J., Kerr T. H., Davies J. K., 1998, MNRAS, 298, 583
Ivison R. J., Smail I., Barger A. J., Kneib J., Blain A. W., Owen F. N., Kerr T. H., Cowie L. L., 2000, MNRAS, 315, 209
Ivison R. J. et al., 2002, MNRAS, 337, 1
Ivison R. J. et al., 2004, ApJS, 154, 124
Ivison R. J. et al., 2005, MNRAS, 364, 1025
Ivison R. J. et al., 2007, MNRAS, 380, 199
Ivison R. J. et al., 2010a, A&A, 518, L31
Ivison R. J., Smail I., Papadopoulos P. P., Wold I., Richard J., Swinbank A. M., Kneib J., Owen F. N., 2010b, MNRAS, 404, 198
Ivison R. J. et al., 2010c, A&A, 518, L35
Kennicutt R. C., Jr, 1998, ARA&A, 36, 189
Kissler-Patig M. et al., 2008, A&A, 491, 941
Knudsen K. K., van der Werf P. P., Kneib J., 2008, MNRAS, 384, 1611
Knudsen K. K., Kneib J., Richard J., Petitpas G., Egami E., 2010, ApJ, 709, 210
Kovács A., Chapman S. C., Dowell C. D., Blain A. W., Ivison R. J., Smail I., Phillips T. G., 2006, ApJ, 650, 592
Kovács A. et al., 2010, ApJ, 717, 29
Kriek M. et al., 2008, ApJ, 677, 219
Lacey C. G., Baugh C. M., Frenk C. S., Silva L., Granato G. L., Bressan A., 2008, MNRAS, 385, 1155
Lacey C. G., Baugh C. M., Frenk C. S., Benson A. J., Orsi A., Silva L., Granato G. L., Bressan A., 2010, MNRAS, 405, 2
Laird E. S., Nandra K., Pope A., Scott D., 2010, MNRAS, 401, 2763
Landsman W. B., 1993, in Hanisch R. J., Brissenden R. J. V., Barnes J., eds, ASP Conf. Ser. Vol. 52, Astronomical Data Analysis Software and Systems II. Astron. Soc. Pac., San Francisco, p. 246
Le Fèvre O. et al., 2004, A&A, 428, 1043
Lehmer B. D. et al., 2005, ApJS, 161, 21
Leitherer C. et al., 1999, ApJS, 123, 3
Luo B. et al., 2008, ApJS, 179, 19
Luo B. et al., 2010, ApJS, 187, 560
McCarthy P. J. et al., 2004, ApJ, 614, L9
Magnelli B. et al., 2010, A&A, 518, L28
Menéndez-Delmestre K. et al., 2007, ApJ, 655, L65
Menéndez-Delmestre K. et al., 2009, ApJ, 699, 667
Mignoli M. et al., 2005, A&A, 437, 883
Morrissey P. et al., 2007, ApJS, 173, 682
Nonino M. et al., 2009, ApJS, 183, 244
Pirard J. et al., 2004, in Moorwood A. F. M., Iye M., eds, SPIE Conf. Ser. Vol. 5492, Ground-based Instrumentation for Astronomy. SPIE, Bellingham, p. 1763
Pope A., Borys C., Scott D., Conselice C., Dickinson M., Mobasher B., 2005, MNRAS, 358, 149
Pope A. et al., 2006, MNRAS, 370, 1185
Pope A. et al., 2008, ApJ, 675, 1171
Popesso P. et al., 2009, A&A, 494, 443
Ravikumar C. et al., 2007, A&A, 465, 1099
Rieke G. H. et al., 2004, ApJS, 154, 25
Rodighiero G. et al., 2010, A&A, 515, A8
Sanders D. B., Mirabel I. F., 1996, ARA&A, 34, 749
Serjeant S. et al., 2010, A&A, 514, A10
Silva L., Granato G. L., Bressan A., Danese L., 1998, ApJ, 509, 103
Siringo G. et al., 2009, A&A, 497, 945
Smail I., Ivison R. J., Blain A. W., 1997, ApJ, 490, L5
Smail I., Ivison R. J., Kneib J., Cowie L. L., Blain A. W., Barger A. J., Owen F. N., Morrison G., 1999, MNRAS, 308, 1061
Smail I., Ivison R. J., Owen F. N., Blain A. W., Kneib J.-P., 2000, ApJ, 528, 612
Stanway E. R., Bunker A. J., McMahon R. G., Ellis R. S., Treu T., McCarthy P. J., 2004, ApJ, 607, 704
Steidel C. C., Shapley A. E., Pettini M., Adelberger K. L., Erb D. K., Reddy N. A., Hunt M. P., 2004, ApJ, 604, 534
Strolger L. et al., 2004, ApJ, 613, 200
Surace J. A. et al., 2005, http://swire.ipac.caltech.edu/swire/astronomers/publications
Swinbank A. M., Chapman S. C., Smail I., Lindner C., Borys C., Blain A. W., Ivison R. J., Lewis G. F., 2006, MNRAS, 371, 465
Swinbank A. et al., 2008, MNRAS, 391, 420
Szokoly G. et al., 2004, ApJS, 155, 271
Takata T., Sekiguchi K., Smail I., Chapman S. C., Geach J. E., Swinbank A. M., Blain A., Ivison R. J., 2006, ApJ, 651, 713
Taylor E. N. et al., 2009a, ApJ, 694, 1171
Taylor E. et al., 2009b, ApJS, 183, 295
Treister E. et al., 2009, ApJ, 693, 1713
Treu T., Auger M. W., Koopmans L. V. E., Gavazzi R., Marshall P. J., Bolton A. S., 2010, ApJ, 709, 1195
Vaccari M. e. A., 2010, A&A, 518, L20
van der Wel A., Franx M., van Dokkum P. G., Rix H., 2004, ApJ, 601, L5
Vanzella E. et al., 2008, A&A, 478, 83
Wang W., Cowie L. L., van Saders J., Barger A. J., Williams J. P., 2007, ApJ, 670, L89
Wardlow J. L. et al., 2010, MNRAS, 401, 2299
Weiß A. et al., 2009, ApJ, 707, 1201
Yang M., Phillips T., 2007, ApJ, 662, 284
Younger J. D. et al., 2007, ApJ, 671, 1531
Younger J. D. et al., 2009, ApJ, 704, 803
Yun M. S. et al., 2008, MNRAS, 389, 333
Zheng W. et al., 2004, ApJS, 155, 73

## APPENDIX A: DISCUSSION OF UNUSUAL SOURCES

Most LESS SMGs have properties similar to previous SMG populations. However, several robust counterparts have unusual properties,

X-ray emission or 8-μm excesses indicative of the presence of an AGN. We discuss these galaxies on a case-by-case basis below.

*LESS 2a and 2b*. LESS 2 has both a robust 24-μm (LESS 2a) and a robust radio counterpart (LESS 2b), separated by 2.7 arcsec, with $z = 1.80^{+0.35}_{-0.14}$ and $2.27^{+0.16}_{-0.55}$, respectively. It is possible that the two counterparts are at the same redshift ($z \sim 2$), separated by ∼20 kpc and may be in the process of merging.

*LESS 6.* LESS 6 is ∼1 arcsec from the robust 24-μm counterpart and ∼2.5 arcsec from the robust radio counterpart, and has a photometric redshift of $z = 0.40^{+0.09}_{-0.03}$; therefore, it is possible that the submillimetre source is a background galaxy which is being gravitationally lensed by LESS 6.

*LESS 9.* This SMG is X-ray luminous and has $z_{\rm phot} = 4.63^{+0.10}_{-1.10}$, making it the highest redshift X-ray source in our sample. Our best-fitting SED shows no 8-μm excess and thus no suggestion of an AGN from the near-IR and optical photometry.

*LESS 10a.* LESS 10a is one of the two counterparts to LESS 10 identified from extended or blended radio emission. It has some 8-μm excess over the best-fitting SED, suggesting the presence of an AGN, but no detectable X-ray emission.

*LESS 11.* Similarly to LESS 9, this galaxy shows no 8-μm excess but is X-ray bright.

*LESS 19.* Based upon the SED fitting, LESS 19 has excess 5.8- and 8-μm emission. However, the source is faint and the fit has $\chi^2 = 10.0$ so it is unclear whether the apparent excess is due to errors in the fitting or the presence of an AGN.

*LESS 20.* This SMG is unusually radio bright with $S_{1.4\,\rm GHz} = 4.25$ mJy. There is no evidence of X-ray emission or an 8-μm excess, suggesting that LESS 20 is a radio-bright AGN. If this is the case, then the AGN contribution to the radio flux means that $T_{\rm D}$ and $L_{\rm FIR}$ are likely to be significantly overestimated. Therefore, we exclude LESS 20 from our analyses of the SFRs and luminosity function of SMGs.

*LESS 40.* LESS 40 has X-ray emission and an 8-μm excess and is highly likely to contain an AGN.

*LESS 50b.* This galaxy is X-ray luminous but does not exhibit a compelling 8-μm excess.

*LESS 57.* LESS 57 has a strong 8-μm excess and is X-ray bright, compelling evidence for the presence of an AGN in this SMG.

*LESS 66.* LESS 66 lies near the diffraction spike of a bright star, so some of the photometry may be unreliable. However, it is an optically bright point source with an 8-μm excess and X-ray emission. There are broad emission lines in the spectra, suggesting that LESS 66 is a submillimetre-bright QSO.

*LESS 67.* This galaxy has coincident X-ray emission and may contain an AGN.

*LESS 74a and b.* The two counterparts to LESS 74 have $z = 1.84^{+0.32}_{-0.49}$ and $1.71^{+0.20}_{-0.17}$, are separated by 2.7 arcsec (∼20 kpc) and have some faint extended emission between them in the optical images. Therefore, it is likely that LESS 74a and LESS 74b are undergoing interaction at $z \sim 1.8$ which triggered the submillimetre emission.

*LESS 75.* Although LESS 75 is not X-ray detected, there is strong 8- and 5.8-μm excess above the best-fitting SED, indicative of a highly obscured AGN.

*LESS 84.* LESS 84 is X-ray detected and has a small 8-μm excess, suggesting it may contain an AGN.

*LESS 96:* LESS 96 is similar to LESS 66 – it is X-ray luminous and has a strong 8-μm excess above the best-fitting SED, and it is a bright optical point source. We interpret this as evidence that LESS 96 is a submillimetre-bright QSO.

*LESS 106.* This SMG is X-ray detected but no 8-μm excess is observed.

*LESS 108:* LESS 108 is identified as a bright local ($z = 0.086$) late-type spiral galaxy from its strong radio and 24-μm emission. The similarity of the radio, mid-IR and NIR, and optical morphologies suggests that this is not a case of gravitational lensing.

*LESS 111.* LESS 111 is X-ray detected and has a 8-μm excess, indicating it may contain an AGN. It lies $\lesssim$3 arcsec from an extended foreground galaxy and is likely to be gravitationally lensed.

*LESS 114.* This SMG is coincident with an X-ray source, but shows no evidence of an 8-μm excess above the best-fitting SED.

*LESS 122.* LESS 122 has excess flux at 8 μm compared to the best-fitting SED but is not X-ray detected.

## APPENDIX B: SED FITS

In Fig. B1, we show the measured photometry and best-fitting SED for each SMG counterpart. The calculated photometric redshifts and errors are shown, and the probability distribution functions presented for each galaxy. Most SMGs are well fitted by out template SEDs, although nine (12 per cent) have excess 8-μm flux above the best-fitting SED.

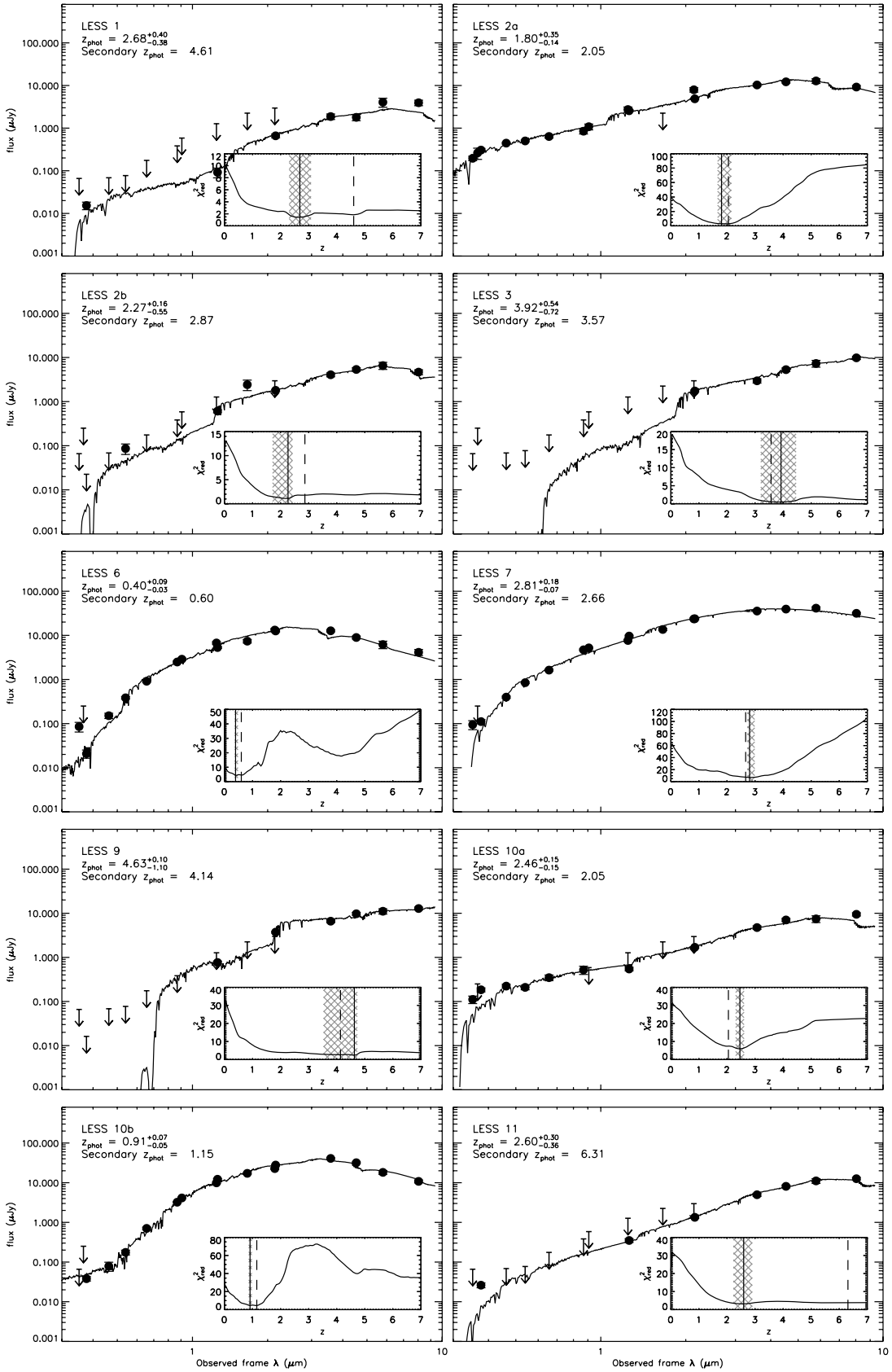


**Figure B1.** Photometry and best-fitting SEDs for robust SMG counterparts; the points and error bars show measured photometry and the arrows represent $3\sigma$ detection limits. Error bars on the primary photometric redshift are 99 per cent confidence limits. The inset panels show the minimum reduced $\chi^2$ at each redshift step with the photometric redshift primary and secondary solutions (where they exist) marked by the solid and dashed lines, respectively; the photometric redshift error is represented by the shaded region.

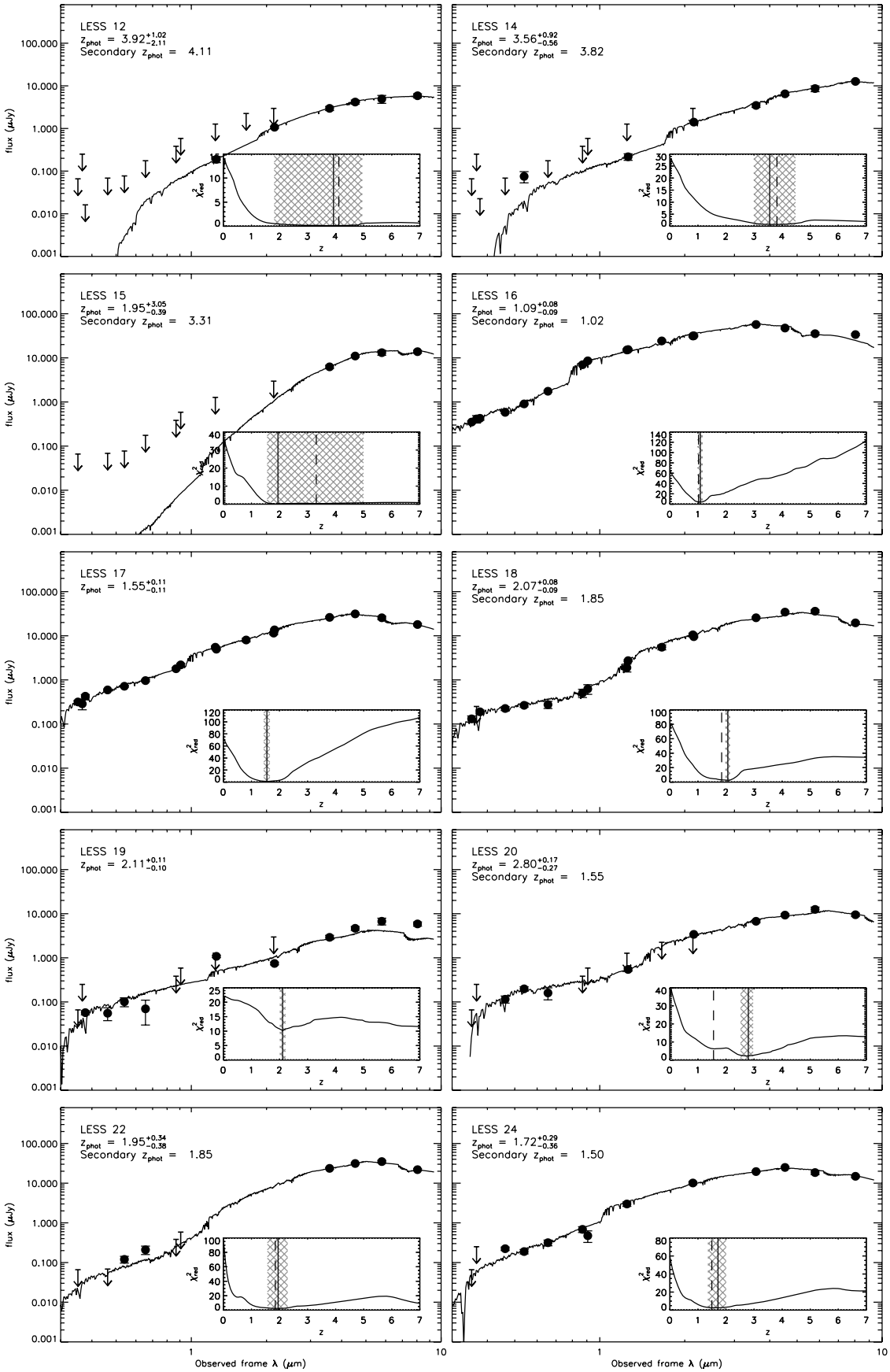


**Figure B1 –** *continued*

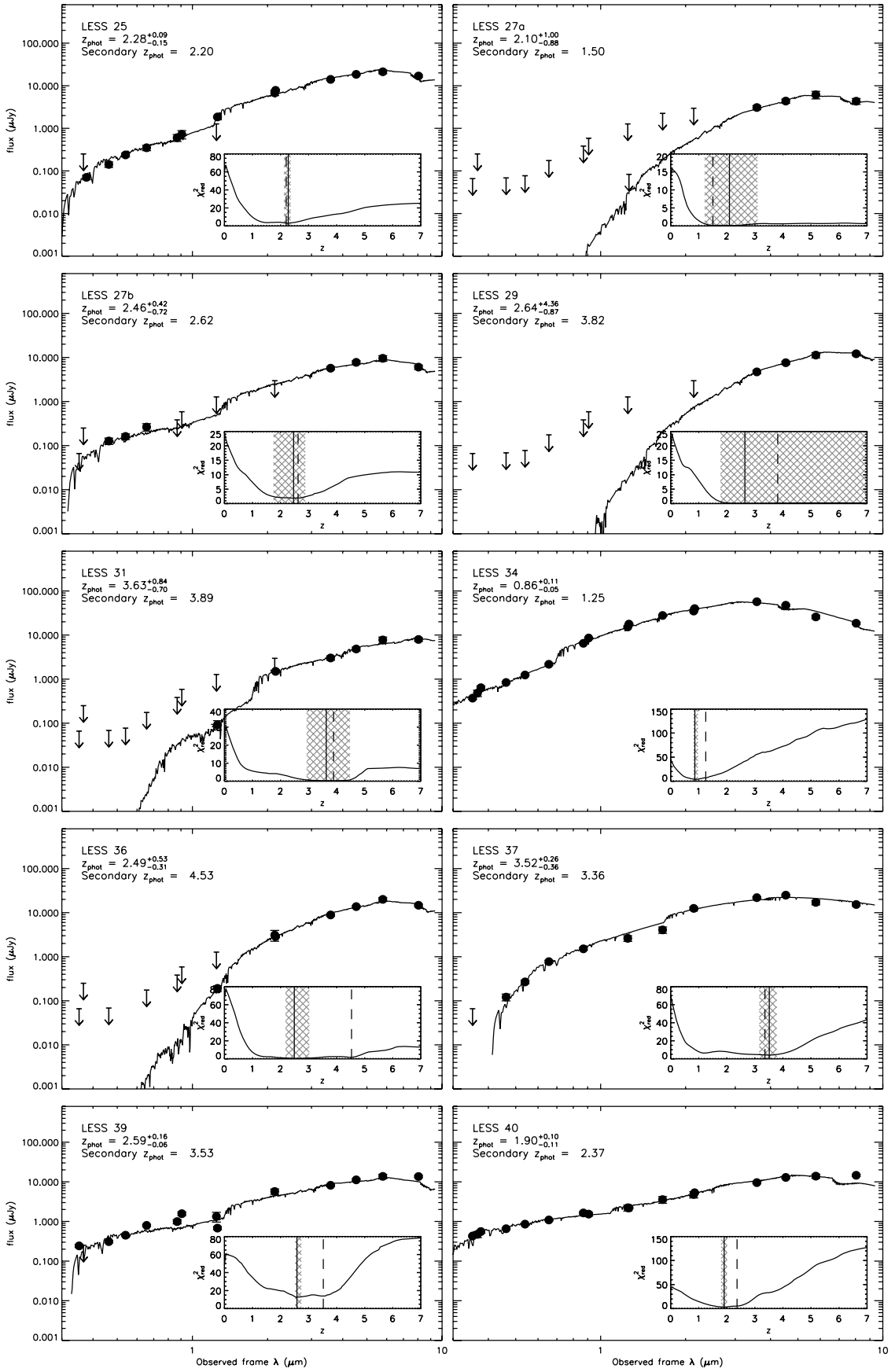


**Figure B1 –** *continued*

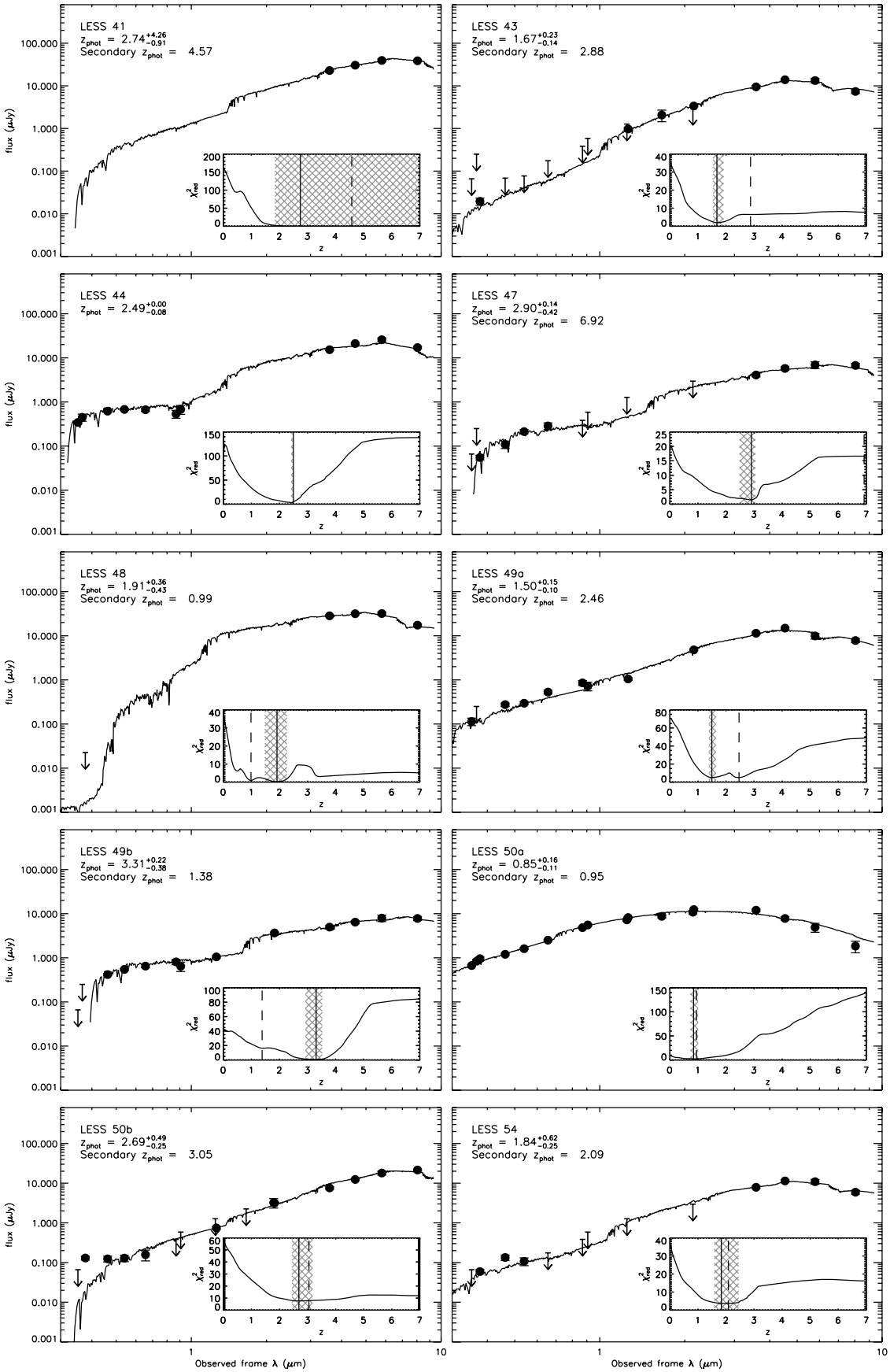


**Figure B1 –** *continued*

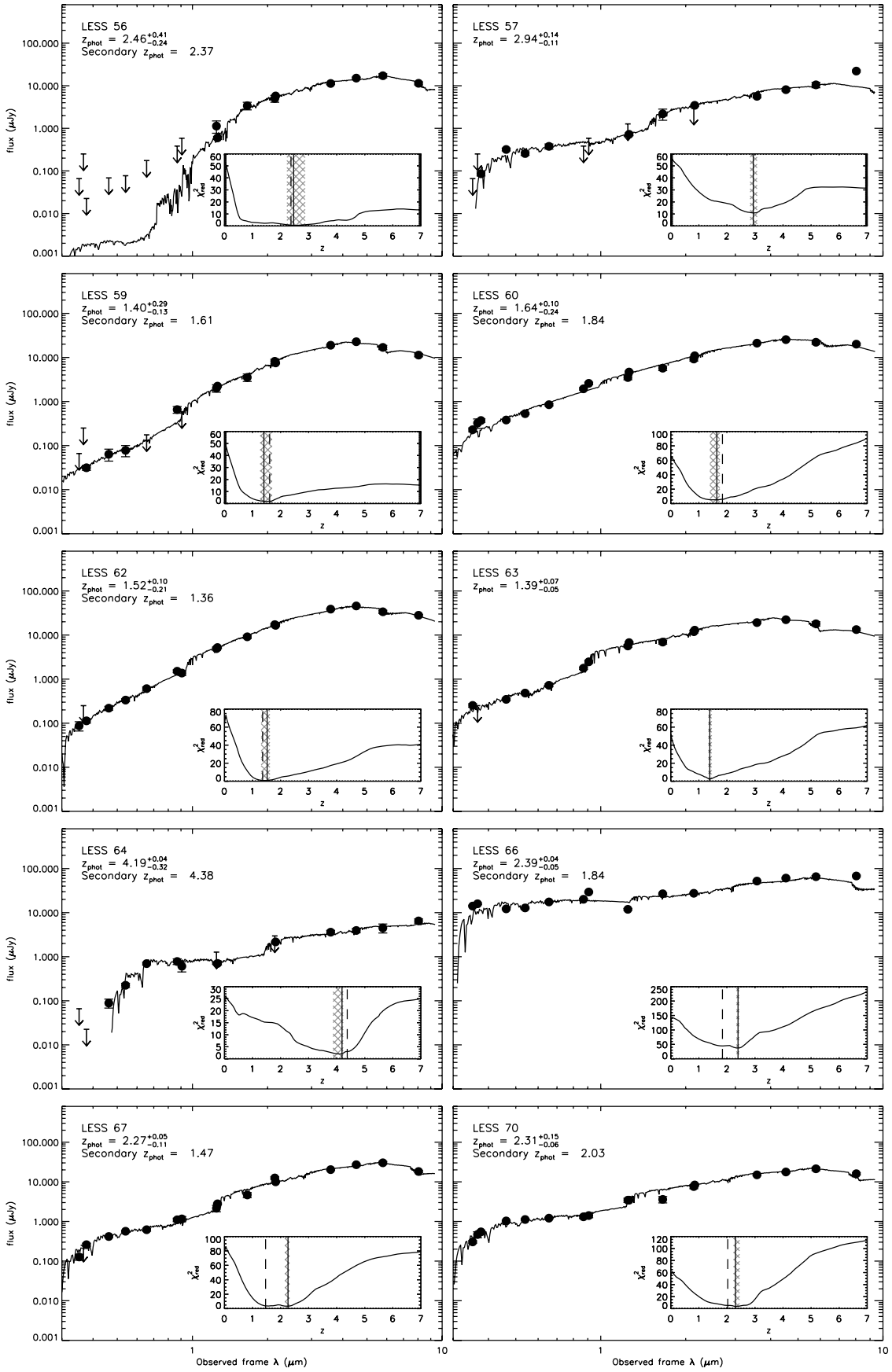


**Figure B1 –** *continued*

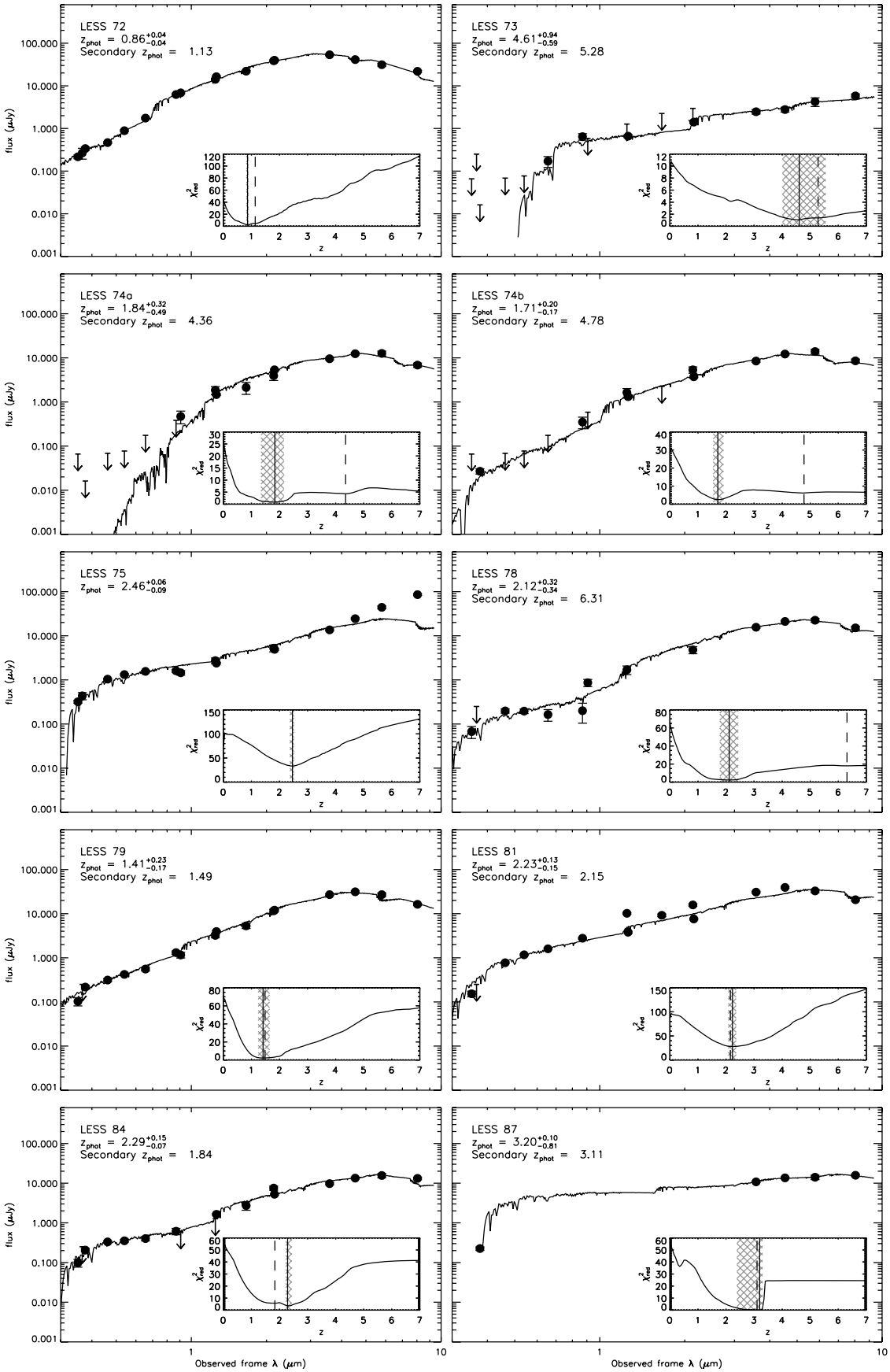


**Figure B1 –** *continued*

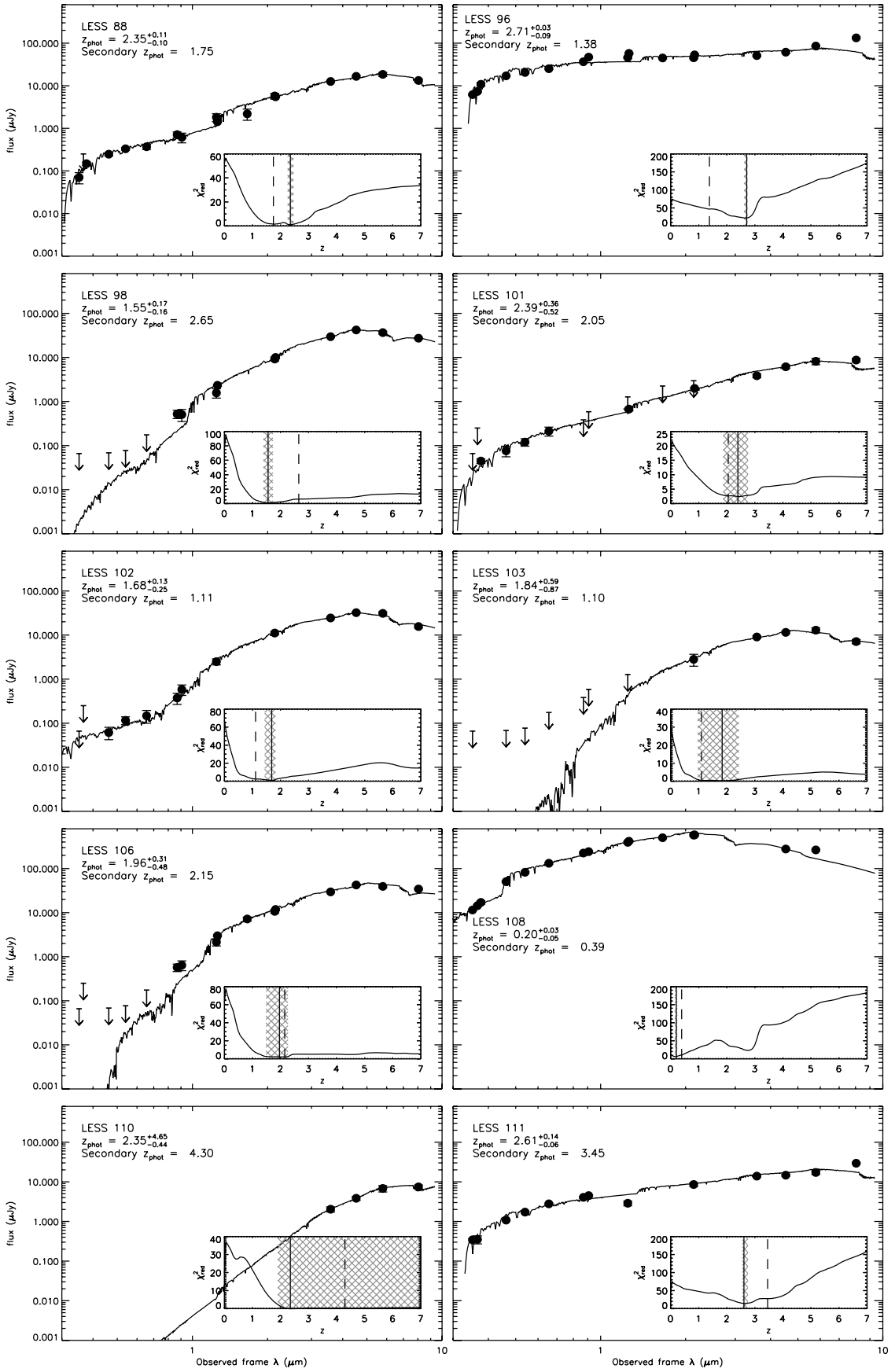


**Figure B1 –** *continued*

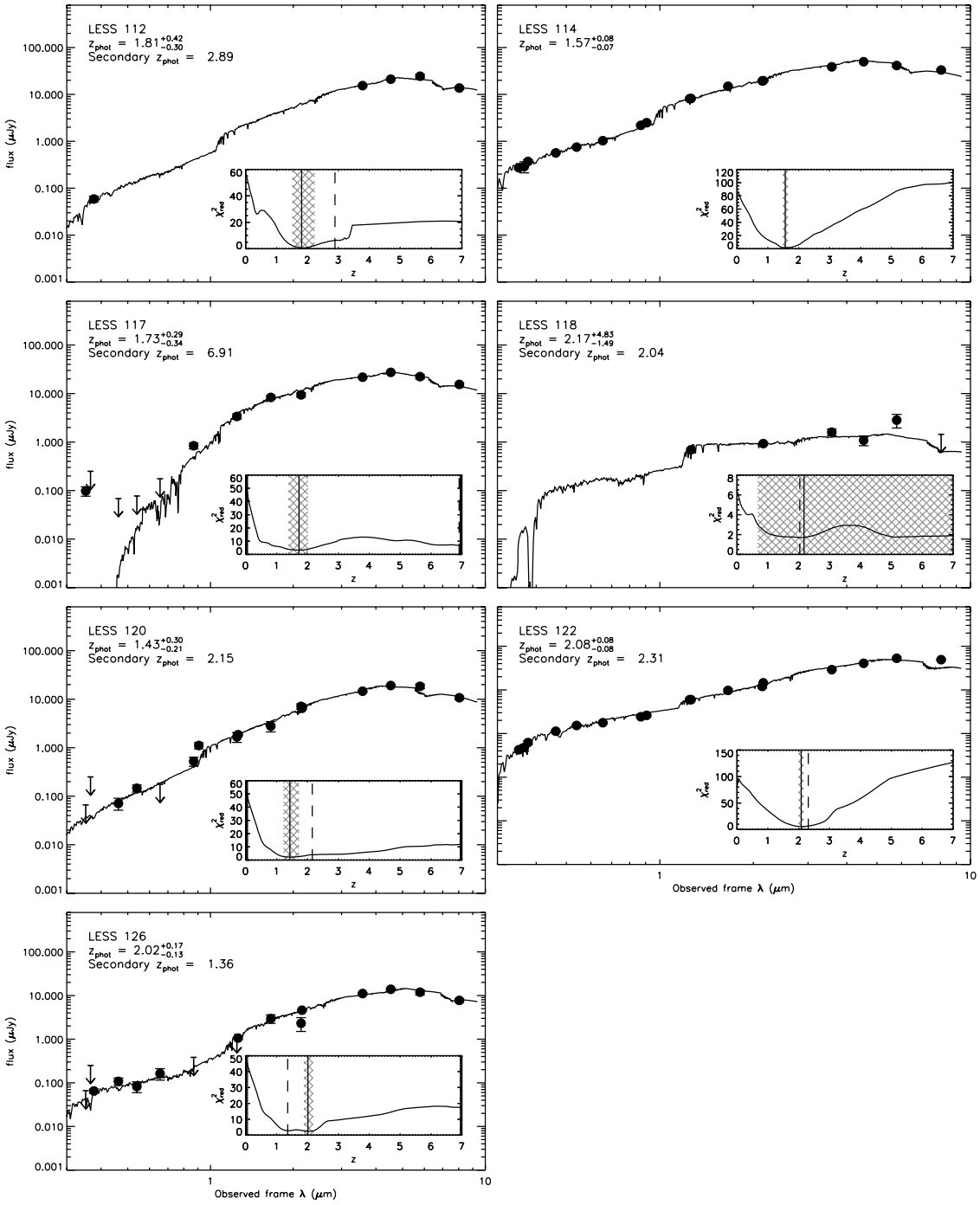


**Figure B1 –** *continued*

This paper has been typeset from a TEX/LATEX file prepared by the author.